Coupled Simulation of Turbomachinery Flutter and Forced Response Blade Vibrations using Nonlinear Frequency Domain Methods

Von der Fakultät für Luft- und Raumfahrttechnik und Geodäsie der Universität Stuttgart
zur Erlangung der Würde eines Doktors der Ingenieurwissenschaften (Dr.-Ing.)
genehmigte Abhandlung

vorgelegt von
Christian Berthold
geboren in
Gießen

Hauptberichter:	Prof. Dr. Malte Krack
Mitberichter:	Prof. Loïc Salles, PhD.

Tag der mündlichen Prüfung: 24. Mai 2024

Institut für Luftfahrtantriebe der Universität Stuttgart

2024

I dedicate this to my parents, my wife and my sister.
Moreover, I want to thank Christian Frey, Malte Krack and Johann Groß for the great support they provided during my work on this thesis.

Contents

Abstract **VIII**

Kurzfassung **IX**

Introduction **1**

1 Motivation **1**

2 State of Knowledge **5**
2.1 Fluid-Structure Interaction (FSI) 5
2.2 Basic Structural Modeling and Aspects of Turbomachinery Blade Rows . . 6
2.3 Flutter Induced Vibrations in Turbomachinery 11
2.4 Forced Response Vibrations in Turbomachinery 15
2.5 Limit State Types 15
2.6 Evaluation of Aerodynamic Forces by CFD 17
2.7 Time Integration Methods 21
2.8 Numerical Analysis of Blade Vibrations 23

3 Purpose of this Work **33**
3.1 Development of Coupled Nonlinear Flutter Analysis Methods for Turbomachinery Blades 35
3.2 Investigation of Nonlinear Blade Vibrations 35
3.3 Advantages and Limitations of the Proposed Methods 36

Methodology **37**

4 Nonlinear Frequency Domain Methods for Flutter and Forced Response **37**
4.1 Energy Methods 37
4.2 Coupled FD-FSI Solver 40
4.3 Application of the FD-FSI Solver to Flutter Induced LCOs 43
4.4 Extension of the FD-FSI Solver to Forced Response Problems 46
4.5 Data Exchange at the Fluid-Structure Interface and Fluid Mesh Deformation 49

Application **53**

5 Numerical LPT Rotor Testcase with Span-to-Chord Ratio of 4 53
5.1 Fluid Model . . . 55
5.2 Benchmark Configurations . . . 57
5.3 Stable Limit Cycle (configuration 1) . . . 59
5.4 Stability Limit (configuration 2) . . . 61
5.5 Discussion of the Computational Effort of FD-FSI Solver and Refined Energy Method . . . 64

6 Numerical LPT Rotor Testcase with Span-to-Chord Ratio of 6 67
6.1 Test Case and Modeling . . . 67
6.2 Computation of the LCO via FD-FSI Solver . . . 71
6.3 Comparison of the Results Obtained by Energy Methods and FD-FSI Solver 72
6.4 Discussion of the Computational Effort . . . 74
6.5 Harmonic Convergence Analysis . . . 74

7 Verification of Nonlinear Frequency Domain Methods with Time Domain Simulations 77
7.1 Structure Model . . . 77
7.2 Aerodynamic Model . . . 78
7.3 TD-FSI Solver . . . 80
7.4 Temporal Resolution . . . 81
7.5 Limitations of TD-FSI and FD-FSI Solvers . . . 81
7.6 LCO14 . . . 83
7.7 LCO8 . . . 86
7.8 LTO12-14-16 . . . 88
7.9 Computational Effort . . . 90

8 Numerical Forced Response Analysis of a LPT Rotor Testcase with Upstream Wake Excitation 91
8.1 Aeroelastic Problem Setting . . . 91
8.2 Comparison of Coupled Analysis Results Against the State of the Art . . . 93
8.3 Assessment of the Numerical Performance of the Developed Methods . . . 98

Evaluation 103

9 Discussion of the Results 103
9.1 The Refined Energy Method . . . 103
9.2 Frequency Domain - Fluid Structure Interaction Solver . . . 104
9.3 Analysis of the Impact of Nonlinear Friction on Flutter Induced LCOs of Turbomachinery Cascades . . . 106
9.4 Analysis of Nonlinear Structural and Aerodynamic Aspects on Forced Response Vibrations . . . 107
9.5 Limitations of the Proposed Methods . . . 107

10 Conclusions 109
10.1 Open Research Questions 109

List of frequently used symbols 111

Publications 113

Bibliography 115

Abstract

The central topic of this work is the simulation of nonlinear blade vibrations in turbomachinery. Two main causes of blade vibrations are flutter, denoting self-excited vibrations of the blades, and forced response due to e.g. aerodynamic rotor-stator interactions. During operation, the vibration levels of the blades must not exceed critical values in order to prevent high cycle fatigue or immediate failure of the engine. This motivates the development of numerical methods for the prediction of blade vibrations in order to evaluate the robustness of mechanical designs against flutter and forced response. In this work, the focus is laid on bladed turbine disks with interlocked shrouds, which represent a challenging task for numerical simulation. While interlocked shrouds introduce friction (and thus damping) into the structural system, possibly reducing the level of vibrations, they can alter the vibration shape and vibration frequency with increasing amplitude. This in turn makes the aerodynamic damping of the blade motion a nonlinear function of the vibration amplitude. Thus, the mechanical system is bidirectionally coupled, since the two physical domains (fluid and solid) interact with each other. Current numerical analysis tools like the energy method or the use of influence coefficients have deficits in resolving these nonlinear fluid-structure interactions. This motivates the development of improved numerical methods for the simulation of nonlinear blade vibrations. In this work, a refined energy method and a bidirectionally coupled fluid-structure solver are suggested for this purpose. For both approaches, the Harmonic Balance method is employed, which approximates a periodic motion of the blades very efficiently in the frequency domain. The novel methods are applied to numerical test cases of low pressure turbines to demonstrate the methods' capabilities and to investigate the potential influence of nonlinear contact forces on the blade vibrations. Here, the refined energy method allows to gain valuable insight on the impact of shroud contact interfaces on the aerodynamic damping. It is found, that the nonlinear structural contact forces can give rise to stable limit cycle oscillations as well as stability limits, which mark the amplitude level where blade vibrations become unstable if it is exceeded. Furthermore, the coupled solver reveals the complex interaction between a vibrating blade with shroud contact interfaces and a shock motion. For the analysis of forced response, the coupled solver is embedded into a path continuation procedure with a sequential and a parallel variant. The coupled method not only demonstrates the influence of nonlinear friction on the forced response but also reveals, that the superposition assumption regarding the aerodynamic wake excitation and the blade vibration induced aerodynamic forces can lead to inaccurate results.

Kurzfassung

Das zentrale Thema dieser Arbeit ist die Simulation von nichtlinearen Schaufelschwingungen in Turbomaschinen. Zwei wichtige Ursachen für Schaufelschwingungen sind Flattern, d.h. selbsterregte Schwingungen der Schaufeln, und erzwungene Schwingungen, z.B. durch aerodynamische Rotor-Stator-Interaktionen. Während des Betriebs dürfen die Schwingungsamplituden der Schaufeln keine kritischen Werte überschreiten, um High Cycle Fatigue oder einen sofortigen Schaden der Maschine zu verhindern. Dies motiviert die Entwicklung numerischer Methoden für die Vorhersage von Schaufelschwingungen, um die Robustheit Turbomaschinenkomponenten gegen Flattern und erzwungene SChwingungen zu bewerten. In dieser Arbeit liegt der Schwerpunkt auf Turbinenschaufeln mit Reibkontakten innerhalb von Deckbändern, die eine anspruchsvolle Aufgabe für die numerische Simulation darstellen. Während diese Reibung (und damit Dämpfung) in die Struktur einbringen und so möglicherweise die Schwingungsamplituden reduzieren, können sie mit zunehmender Amplitude die Schwingungsform und -frequenz verändern. Dies wiederum macht die aerodynamische Dämpfung der Schaufelschwingung zu einer nichtlinearen Funktion der Schwingungsamplitude. Das mechanische System ist also bidirektional gekoppelt, da die beiden physikalischen Domänen (Strömung und Struktur) miteinander interagieren. Aktuell verfügbare numerische Analysewerkzeuge wie die Energiemethode oder die Verwendung von aerodnyamischen Einflusskoeffizienten haben Defizite bei der Vorhersage dieser nichtlinearen Strömung-Struktur Wechselwirkungen. Dies motiviert die Entwicklung verbesserter numerischer Methoden für die Simulation nichtlinearer Schaufelschwingungen. In dieser Arbeit werden zu diesem Zweck eine verfeinerte Energiemethode und ein bidirektional gekoppelter Strömung-Struktur-Löser entwickelt. Für beide Ansätze wird die Harmonic Balance Methode verwendet, die eine periodische Bewegung der Schaufeln im Frequenzbereich sehr effizient approximiert. Die neuen Methoden werden auf numerische Testfälle von Niederdruckturbinen angewandt, um die Fähigkeiten der Methoden zu demonstrieren und den möglichen Einfluss nichtlinearer Kontaktkräfte auf die Schaufelschwingungen zu untersuchen. Hier ermöglicht die verfeinerte Energiemethode einen wertvollen Einblick in die Auswirkungen der Kontaktreibung im Deckband auf die aerodynamische Dämpfung. Es zeigt sich, dass die nichtlinearen strukturellen Kontaktkräfte zu stabilen Grenzzyklusschwingungen sowie zu Stabilitätsgrenzen führen können, welche das Amplitudenniveau angeben, bei dessen Überschreitung die Schaufelschwingungen instabil werden. Darüber hinaus zeigt der gekoppelte Löser die komplexe Interaktion zwischen einer schwingendend Schaufel mit Kontaktreibung und einer Stoßbewegung in der Strömung. Für die Analyse von erzwungenen Schwingungen wird der gekoppelte Löser in eine numerische Pfadverfolgung mit einer sequentiellen und einer parallelen Variante eingebettet. Die gekoppelte Methode zeigt nicht nur den Einfluss der nichtlinearen Reibung auf die erzwungene Schwingungsantwort, sondern auch, dass die Superpositionsannahme bezüglich der aerodynamischen Nachlaufanregung und der durch die Schaufelschwingung induzierten aerodynamischen Kräfte zu ungenauen Ergebnissen führen kann.

1 Motivation

In turbomachinery, the relative rotation of components and dynamical instabilities inevitably induce structural vibrations, which can lead to high cycle fatigue (HCF) or immediate fracture and thus must be reduced to an acceptable level. In the following, a brief introduction to turbomachinery blade vibrations is given which also serves as motivation for this work. Some content of this chapter is taken from [F, C, D].

A critical component subject to vibrations are the blade rows in the compressor or turbine of an engine. An example of a shrouded Low Pressure Turbine (LPT) blade row is shown in **Figure 1.1**. Blades in axial turbomachinery must withstand high mechanical stresses during operation. Static stresses are caused by rotation (centrifugal forces), the stationary flow (static flow forces) and thermal loads. Mechanical vibrations caused by dynamic loads of different origins, lead to vibrational stresses. Depending on the level level of static stress, sustained vibration stresses can lead to HCF. In addition, the vibrations can also cause wear in joints and noise. Vibrations are therefore a central problem in the design of aircraft engines and stationary gas and steam engines. Two of the most important vibration mechanisms of airfoils result from the aeroelastic interactions with the surrounding unsteady flow: (a) speed-synchronous forced vibration and (b) flutter [62]. An example of flutter induced vibrations leading to engine damage is depicted in **Figure 1.2**, where the blade cracked at the blade root and eventually broke off completely.

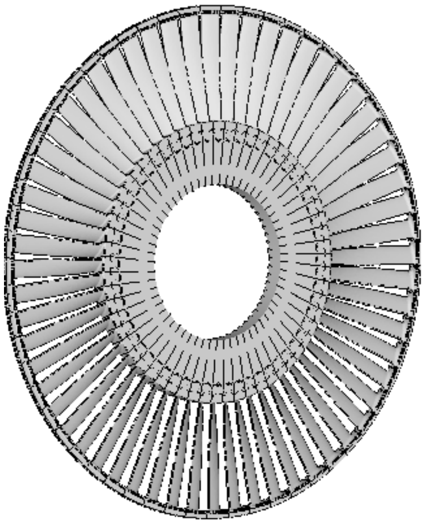

Figure 1.1: Example of a shrouded LPT blade row.

Other vibration mechanisms of aeroelastic nature arise, for example due to acoustic resonances and vortex shedding, which occur in particular beyond the nominal operating range.

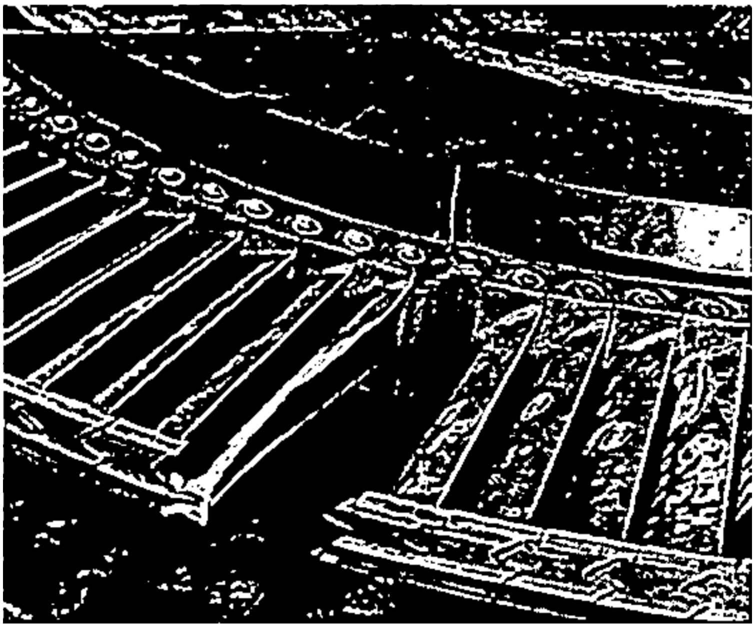

Figure 1.2: A fractured shrouded turbine blade row. [62]

In case (a), the dynamic loads result from the rotation of the blades due to the inhomogeneous pressure field in the circumferential direction. Pressure inhomogeneities are caused by aerodynamic interactions between the stator and rotor blade rows as well as non-homogeneous inflow or outflow conditions. An example of the former are the wakes of the upstream blade row. This leads to a dynamic load with frequencies that are integer multiples of the rotational frequency. In the case of resonance, i.e. when an excitation frequency coincides with a natural frequency of the structure, the forced vibrations are only limited by the existing damping and can become particularly large.

Flutter refers to the unstable aeroelastic interaction of a vibrating structure with the surrounding flow. In turbomachinery, flutter is caused by the cascade effect, i.e. the aerodynamic interference between the blades within a blade row. If this interaction is unstable the blades receive energy from the unsteady flow due to their oscillation, which is a self-excitation mechanism. In contrast to forced oscillations, the oscillation frequency in the case of flutter is generally not an integer multiple of the speed [62].

A thorough analysis of blade vibrations during the design process of an engine is crucial, as it has to ensure a safe operation over its whole lifetime. What makes this task challenging is the existence of several nonlinearities in both domains (fluid and structure). On the fluid side nonlinear flow features like moving shocks in transonic flows or detached flow can influence the aerodynamic forces on the moving blade while on the structural side nonlinear contact forces from joints or dissipative devices lead to further complexity. The interplay of such nonlinearities has not yet been investigated and is therefore not yet fully understood. Thus, no suitable and efficient methodology for the coupled simulation is known which, however, is precisely a prerequisite for the investigation of nonlinear interactions.

Optimizing the performance of aircraft engines is a current challenge. Especially the environmental impact due to exhaust gases is to be reduced, which requires further improvement of turbomachinery components. However, the goals of increased efficiency and reduced weight of the engine is competing with the robustness of the structure against vibrations. In the resulting challenge for optimized designs, better methods for the prediction of the resulting vibrations is crucial. The development of new numerical methods which have the capability of simulating nonlinear blade vibrations of the coupled fluid-structure system, as done in this work, hopefully contributes to this challenge.

2 State of Knowledge

This chapter presents the relevant state of knowledge regarding flutter and forced response vibrations of turbomachinery blades and their numerical analysis. Some parts of this chapter are published in [D, C, F, G].

2.1 Fluid-Structure Interaction (FSI)

Blade vibrations interact with the surrounding fluid which makes their analysis challenging. This interaction constitutes a coupled problem as illustrated in **Figure 2.1**. The flow chart shows the coupling of fluid and structure dynamics. A blade's motion, governed by structure dynamics, influences the boundary of the fluid domain and thus impacts the fluid flow. In turn, the fluid generates unsteady aerodynamic forces on the blade surface and thus potentially alters the blade motion. This type of coupling is denoted as *bidirectional* or *fully coupled* since the two physical domains (fluid and solid) interact with each other in both directions. Consequently, analyzing turbomachinery blade vibrations in a precise manner requires to consider the coupled mechanical problem. In many circumstances however, assumptions are valid which make a bidirectional analysis unnecessary and allow for simplified analysis methods in order to approximate the behavior of the blade row and its vibrations. In this case, typically one branch between the fluid and the structure domain in **Figure 2.1** is neglected (e.g. the aerodynamic forces are not transferred back to the blade surface), which is denoted as *unidirectional*.

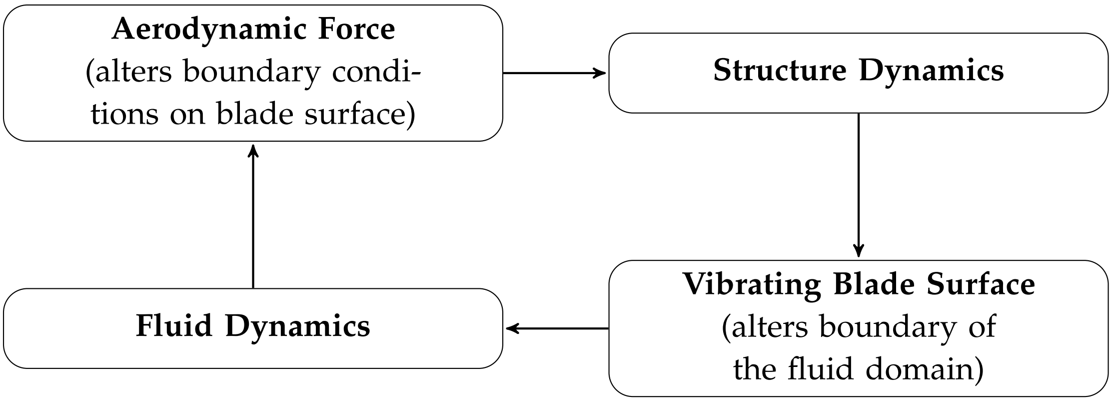

Figure 2.1: Coupling schematic of the fluid-structure interaction (FSI) problem.

2.2 Basic Structural Modeling and Aspects of Turbomachinery Blade Rows

In real world machines, mistuning is always present, at least due to manufacturing tolerances (unintentional), or is even brought in intentionally. It describes blade to blade variations in the material, geometry or both and influences the deflection shape of each blade as well as the vibration frequency [18, 9]. Intentional mistuning is commonly used as a measure to mitigate aerodynamic instability [36]. A popular special case is AB-mistuning, in which two types of blades (type A and type B) are assembled in an alternating way around the circumference, which differ for example, in their airfoil thickness. Unintentional mistuning can increase the maximum vibration amplitude (of individual blades) during forced response and reduce the tendency to flutter [44]. A very drastic example is a missing blade, as depicted in **Figure 1.2**.

The effect of smaller mistuning in the case of strong coupling between the sectors, as in the case of blade to blade coupling via a shroud, is known to be negligible [67]. Thus, the current design strategy is to use high-quality models to calculate the symmetrical case and to consider the influence of mistuning by means of magnification factors, which are obtained from experience and/or highly simplified full models. A tuned blade row with identical sectors is thus denoted as cyclic symmetric. One sector can contain a single or multiple blades with the corresponding disk segments, however in the following one sector denotes a single blade and disk segment since only cyclic symmetric blade rows are considered in this work.

For many relevant modeling strategies, the dynamic force balance for the structure is obtained from a Finite Element (FE) discretization, where material damping can be assumed as small and thus in most cases is neglected. In a preprocessing step a static equilibrium under centrifugal loading due to the rotation speed (for rotors) should be computed (nonlinear static calculation). Since deformations cannot be assumed to be small during this step, nonlinear geometric effects are taken into account. The static equilibrium serves as a new reference configuration for the following dynamic force balance:

$$\boldsymbol{M}_{\mathrm{FE}}\ddot{\boldsymbol{q}}_{\mathrm{FE}} + \boldsymbol{K}_{\mathrm{FE}}\boldsymbol{q}_{\mathrm{FE}} + \boldsymbol{f}^{\mathrm{c}}_{\mathrm{FE}}(\boldsymbol{q}_{\mathrm{FE}}, \dot{\boldsymbol{q}}_{\mathrm{FE}}) = \boldsymbol{f}^{\mathrm{a}}_{\mathrm{FE}}(\boldsymbol{q}_{\mathrm{FE}}, \dot{\boldsymbol{q}}_{\mathrm{FE}}). \tag{2.1}$$

The sparse, symmetric and positive definite matrices $\boldsymbol{M}_{\mathrm{FE}}$ and $\boldsymbol{K}_{\mathrm{FE}}$ are the mass and the stiffness matrix respectively and $\boldsymbol{q}_{\mathrm{FE}}$ denotes the FE nodal displacement coordinates (counted from the static equilibrium). The elastic forces are linearized which implies a linear geometric behavior and thus the model is only suitable for small deformations. $\boldsymbol{f}^{\mathrm{c}}_{\mathrm{FE}}$ denotes the contact forces, for which a suitable model must be chosen and $\boldsymbol{f}^{\mathrm{a}}_{\mathrm{FE}}$ denotes the fluid pressure forces acting on the blade surface, where the shear forces due to the viscosity of the fluid are neglected since their contributed work is small compared to the work done by the surface pressure in a variety of FSI applications, including flutter [72]. Through $\boldsymbol{f}^{\mathrm{a}}_{\mathrm{FE}}$, the structural dynamics are coupled to the fluid dynamics. It should be noticed, that, depending on the underlying modeling, $\boldsymbol{f}^{\mathrm{a}}_{\mathrm{FE}}$ and $\boldsymbol{f}^{\mathrm{c}}_{\mathrm{FE}}$ may have a hysteretic behavior.

2.2.1 Periodic Vibrations and Traveling Wave Motion

For a full wheel blade row an eigenvalue analysis of Eq. (2.1) can be performed, which reveals the mode shapes $\boldsymbol{\psi}$ and associated eigenfrequencies $\boldsymbol{\omega}$ of the free vibrations in vacuum:

$$(\boldsymbol{K}_{\mathrm{FE}} + \boldsymbol{K}^{\mathrm{c}} - \omega^2 \boldsymbol{M}_{\mathrm{FE}})\boldsymbol{\psi} = \boldsymbol{0}. \tag{2.2}$$

Here, the contact forces (e.g. in shroud contact interfaces) are linearized: $\boldsymbol{f}^{\mathrm{c}} \approx \boldsymbol{K}^{\mathrm{c}} \boldsymbol{q}_{\mathrm{FE}}$ (more details on contact modeling are given later).

When a blade row is cyclic symmetric, also its natural mode shapes $\boldsymbol{\psi}$ are of cyclic symmetry, as depicted in **Figure 2.2**, and can be associated to nodal diameters (NDs). In **Figure 2.2**, the displacements of all blade tips correspond to 5 sine waves distributed around the circumference, which is then denoted as ND $= 5$ mode shape. For turbomachinery applications, it is customary to consider only the ND ranges $[-N_{\mathrm{Blades}}/2 - 1, N_{\mathrm{blades}}/2]$ for an even amount blades and $[-(N_{\mathrm{Blades}} - 1)/2, (N_{\mathrm{blades}} - 1)/2]$ for an uneven amount, especially, if the bladed disk is reduced to a single representative sector for subsequent analysis. Modes with NDs beyond these ranges can be considered as higher modes of vibration of the considered NDs.

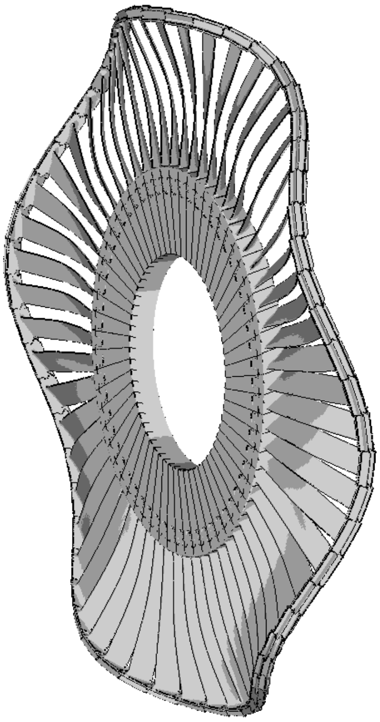

Figure 2.2: Example of a blade row's mode shape with ND 5.

For a cyclic blade row, mode shapes come in pairs with the same eigenfrequency, except for ND 0 (and in case of an even amount of blades also ND $N_{\text{Blades}}/2$) modes, where only a single mode shape per eigenfrequency exists. Such a pair of modes can vibrate with a constant phase relationship, making the wave formed by the blade tips (cf. **Figure 2.2**) travel around the circumference, which is then denoted as a traveling wave. In this case, the periodic motion of two adjacent blades (1 and 2) has a constant time lag $u_1(t) = u_2(t + \Delta t)$. A traveling wave can spin around clockwise or anti-clockwise, which is expressed by a plus or minus sign before the ND number (e.g ND +5/-5). An exception are ND 0 (and in case of an even amount of blades also ND $N_{\text{Blades}}/2$) waves, which are standing waves. For a harmonic vibration, the time lag between two adjacent blades can also be considered as a phase lag, which is denoted as Inter-Blade Phase Angle (IBPA). The relation between the IBPA and ND is given by

$$\text{IBPA} = \frac{2\pi}{N_{\text{Blades}}}\text{ND}. \tag{2.3}$$

Since flutter typically occurs for traveling (standing) wave modes, it is customary to study periodic blade vibrations in the form of traveling (standing) waves. In this case, structural oscillations and the fluctuations of the flow field from one sector and the adjacent sector have the above mentioned time/phase lag. This can be utilized for the analysis of flutter vibrations in order to reduce the problem to one sector (i.e. typically one flow passage and one blade with the corresponding disk segment), which is a significant simplification and reduction of computational resources. In case of a cyclic symmetric excitation of a blade row (forced response), the same simplification can be applied. Consequently only a single sector/blade needs to be calculated with appropriate periodic boundary conditions (BCs) at the cyclic boundaries for each ND/IBPA of interest [17, 56]. For more details on traveling wave coordinates and circumferential wave numbers, the reader is referred to [36, A].

2.2.2 Structural Model Order Reduction

Directly solving Eq. (2.1) (e.g. by means of temporal discretization schemes) is computationally expensive. Thus, different model order reduction techniques have been proposed in order to reduce the amount of unknowns and the computational costs. Many reduction methods use a reduced basis with appropriate basis vectors for the approximation of the structural motion. In this case, the displacements of the original FE model can be recovered from the generalized coordinates $\boldsymbol{u}^{\text{s}}$ according to

$$\boldsymbol{q}_{\text{FE}} = \boldsymbol{T}\boldsymbol{u}^{\text{s}}, \tag{2.4}$$

where the number of unknowns in $\boldsymbol{u}^{\text{s}}$ is typically much smaller than in $\boldsymbol{q}_{\text{FE}}$.

Modal truncation, where a few selected normal modes $\boldsymbol{\psi}_i$ of the eigenvalue problem Eq. (2.2) are used for the construction of the reduced basis

$$\boldsymbol{T}_{\text{MOD}} = [\boldsymbol{\psi}_0, \boldsymbol{\psi}_1, \dots], \tag{2.5}$$

is one of the simplest ways of obtaining a Reduced Order Model (ROM). Inserting the transformation rule $\boldsymbol{q}_{\mathrm{FE}} = \boldsymbol{T}_{\mathrm{MOD}}\boldsymbol{u}^{\mathrm{s}}$ into Eq. (2.1) and multiplying with $\boldsymbol{T}_{\mathrm{MOD}}^{\mathrm{H}}$ from the left yields

$$\boldsymbol{M}\ddot{\boldsymbol{u}}^{\mathrm{s}} + \boldsymbol{K}\boldsymbol{u}^{\mathrm{s}} + \boldsymbol{f}^{\mathrm{c}} = \boldsymbol{f}^{\mathrm{a}} \tag{2.6}$$

with $\boldsymbol{M} = \boldsymbol{T}_{\mathrm{MOD}}^{\mathrm{H}}\boldsymbol{M}_{\mathrm{FE}}\boldsymbol{T}_{\mathrm{MOD}}$ ($\boldsymbol{K}$ is analogous) and $\boldsymbol{f}^{\mathrm{c}} = \boldsymbol{T}_{\mathrm{MOD}}^{\mathrm{H}}\boldsymbol{f}_{\mathrm{FE}}^{\mathrm{c}}$ ($\boldsymbol{f}^{\mathrm{a}}$ is analogous). Since the FE matrices are symmetric and positive definite, the mass and stiffness matrices of the modally reduced ROM are diagonal. If nonlinear contact forces have been linearized as in Eq. (2.2) and they are already accounted for in the stiffness matrix $\boldsymbol{K}$, the formulation of the nonlinear contact forces $\boldsymbol{f}^{\mathrm{c}}$ must be adapted. Often, the linearization of contact forces means to assume fully sticking contacts.

While modal truncation provides a simple way of constructing a ROM, it is not particularly suitable for accurate modeling of contact interfaces with dry friction, especially when a change of mode shape and frequency are expected, since this would require a very large amount of normal modes $\boldsymbol{\psi}_i$, which does not reduce the computational cost as desired.

A more efficient approximation of a blade row's structural dynamics with contact friction interfaces can be achieved with the Component Mode Synthesis (CMS), where the structural motion is approximated by a set of component modes. A popular CMS technique is the Craig-Bampton method [12], which is also used in this work extensively. Accordingly, a few coordinates of the FE model $\boldsymbol{q}_{\mathrm{FE}}^{\mathrm{retained}}$ are retained for the surface where friction is to be modeled and the remaining ones $\boldsymbol{q}_{\mathrm{FE}}^{\mathrm{internal}}$ are reduced. Therefore it is customary to reorganize the FE coordinates as

$$\boldsymbol{q}_{\mathrm{FE}} = \begin{bmatrix} \boldsymbol{q}_{\mathrm{FE}}^{\mathrm{retained}} \\ \boldsymbol{q}_{\mathrm{FE}}^{\mathrm{internal}} \end{bmatrix}, \tag{2.7}$$

before a new basis $\boldsymbol{T}_{\mathrm{CB}}$, containing the component modes as column vectors, is constructed:

$$\boldsymbol{T}_{\mathrm{CB}} = \begin{bmatrix} \boldsymbol{I} & \boldsymbol{0} \\ \bar{\boldsymbol{\psi}} & \boldsymbol{\Phi} \end{bmatrix}. \tag{2.8}$$

The set of component modes is formed by static constraint modes and fixed-interface normal modes. The static constraint modes are associated with the displacements of each contact node pair. $\bar{\boldsymbol{\psi}}$ represents the static displacement of the remaining nodal degrees of freedom in response to a unit displacement of each relative coordinate. The fixed-interface modes are normal modes, which are obtained from the FE model by fixing all coordinates associated with the retained nodes (sticking contact conditions); the deflection shapes associated with the lowest-frequency normal modes are collected as columns in the matrix $\boldsymbol{\Phi}$. Finally, the transformation of the FE model to the ROM system is analogous to the modal reduction but with $\boldsymbol{T}_{\mathrm{CB}}$ instead of $\boldsymbol{T}_{\mathrm{MOD}}$.

Another method for model order reduction is proposed in [50] where the system is reduced by approximating the Forced Response Function (FRF) matrix with respect to the degrees of freedom where contact forces are modeled. This method is however only applicable to a frequency domain analysis while modal truncation and CMS techniques are not restricted to a certain temporal discretization method.

2.2.3 Impact of Contact Friction and its Modeling

In **Figure 2.3** a shroud with a contact interface is depicted which is the source of structural nonlinearity of primary interest in this work. Between the contacting surfaces, nonlinear effects like friction can occur, which is the major contribution to structural dissipation [36]. The level of structural dissipation can be quantified with the damping ratio

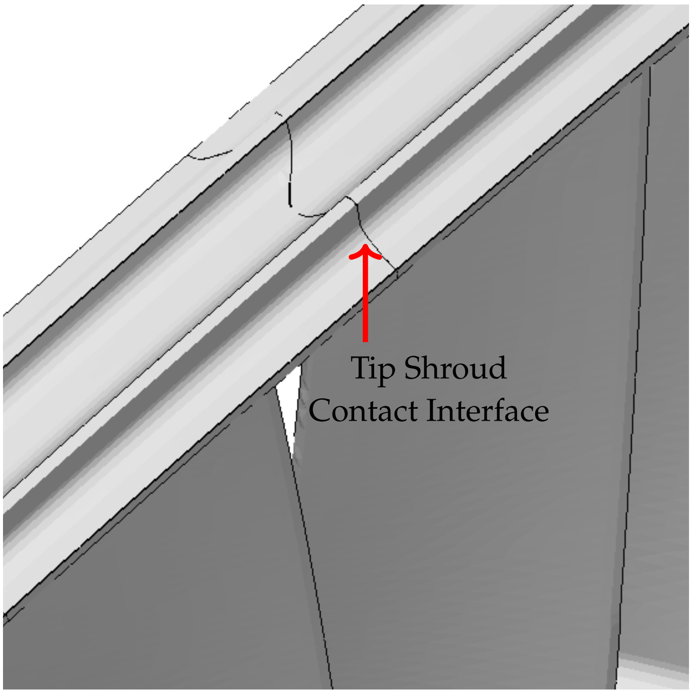

Figure 2.3: Shroud of a turbine blade row with interfaces.

$$D_s = \frac{W_s}{4\pi E_{\mathrm{kin,max}}} \tag{2.9}$$

where W_s is the dissipation work performed during one period of oscillation and $E_{\mathrm{kin,max}}$ denotes the maximum kinetic energy of the vibrating mode shape.

If the vibrating structure behaves linearly (as in case of linear material damping), then the damping ratio is constant with respect to the vibration amplitude. When dry friction is present however, D_s is a nonlinear function of the vibration amplitude due to the contact nonlinearity. Additionally, the mode shape $\boldsymbol{\psi}$ and vibration frequency ω of a free vibration analysis are not constant anymore but as well are a function of the amplitude. Especially friction in tip shroud interfaces can have a significant influence on a blade's mode shape and vibration frequency.

Thus, the modeling of contact forces is crucial in order simulate the nonlinear behavior of blade vibrations, if contact interfaces are present. The contact problem can be split into a static and a dynamic part [36]. In the static part, the normal load distribution (i.e. the contact pressure between two contacting surfaces) and deformation of the structure under static forces (e.g. centrifugal) is determined. This step can be included in the preprocessing step described in Section 2.2, by considering contact forces in the nonlinear static calculation. In the subsequent dynamic analysis, the dynamic contact forces must be modeled. For convenience, a coordinate transform to the relative displacements at each contact node pair can be carried out, assuming that the deformations and thus the sliding between the contact surfaces is small. This way, the contact kinematics are not described by the absolute position of each contact node but by the relative positions of the contact node pairs, which can simplify the formulation of contact models. There are numerous methods for frictional and normal contact forces available. In [36] an overview of some methods is given and due to the complexity of contact mechanics, it is still a lively field of research.

2.3 Flutter Induced Vibrations in Turbomachinery

In the case of flutter, the blade vibrations are self-excited. In other words, the aerodynamic stability depends on the sign of the aerodynamic work that the surrounding flow performs on the blades per oscillation cycle. The aerodynamic work is influenced by the vibrating mode shape, the oscillation frequency and the flow conditions [31]. The reduced frequency

$$k = \frac{c\omega}{2V}, \tag{2.10}$$

which is the ratio between the angular frequency of the oscillation ω, chord length c and the velocity of the outflow V, is an important influencing variable in addition to the vibration shape [49], especially in the context of low-pressure turbines (LPTs). The lower k, the higher the susceptibility to flutter which is of relevance for fan cascades and LPTs which both have rather long and slender blades with low eigenfrequencies and thus low reduced frequencies. In a turbomachinery compressor several regions in a compressor stability map can be identified, where flutter occurs, e.g. stall flutter close to the stall line or choke flutter close to the choke line at moderate mass flow.

Tuned blade rows in turbomachinery have a rotationally periodic structure and thus the vibrations typically take the form of traveling (or standing) waves, as explained in Section 2.2.1. The natural frequency and the exact form of vibration depend on the ND. This applies in particular if there is a significant mechanical coupling of the blades, e.g. if the disc is comparatively flexible or if there is a coupling via other structural elements such as a shroud. The qualitative aerodynamic influence significantly depends on both, the ND as well as the direction of propagation of the traveling waves [49]. The quantitative influence increases with decreasing mass ratio, which is the ratio between the mass of

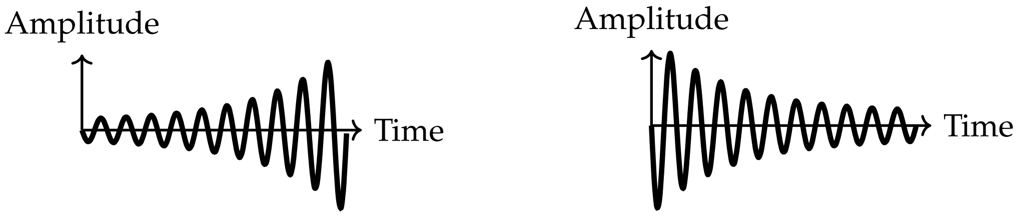

(a) Growth (b) Decay

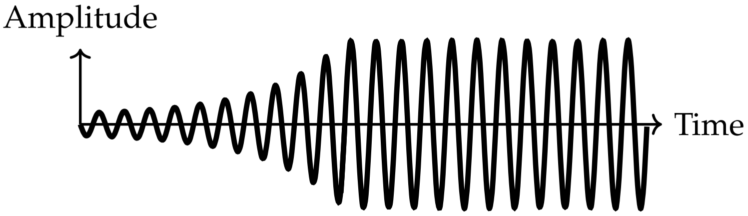

(c) Forming of a Limit Cycle Oscillation (LCO)

Figure 2.4: a) and b): Exponential growing and decaying amplitude, c): LCO

the flowing blade and the flowing gas. Mass ratios for turbomachinery blades are $\gg 1$, often > 100, which means that the vibrating mode is largely determined by the structure itself. The aerodynamic influence is responsible for the aerodynamic damping (negative in the flutter case) as well as the shift of the natural frequencies and can also cause a distortion of the vibrating modes. A strong influence of the flow is to be expected in areas of high aerodynamic loads and high sensitivity, especially in the presence of resonances or aeroelastic instability. Thus, both the aerodynamic and the mechanical coupling within the blade row have an effect on the mode shape and reduced frequency, and thus on the aeroelastic stability.

In the case of flutter, energy is transferred from the fluid into the structural vibration and the blade row is self-excited. Without any structural dissipation and under the assumption of linearized aerodynamic forces, the vibrational amplitude would grow exponentially as illustrated in **Figure 2.4(a)**. In a real engine, where nonlinear effects will eventually occur, this can lead to immediate failure or high cycle fatigue (in case of saturated but too large vibration amplitudes). If energy is transferred from the structure to the fluid, the vibrations are aerodynamically damped and the vibrational amplitude decays, cf. **Figure 2.4(b)**.

The aerodynamic flutter intensity can be quantified with the logarithmic decrement $\delta = \log(\frac{\hat{q}_1}{\hat{q}_2})$, which is the logarithm of the factor by which the amplitude $\hat{q}$ decreases during one period $T = \frac{2\pi}{\omega}$ if structural dissipation is absent. A positive value of δ describes a decaying oscillation while a negative value describes a growing oscillation.

Since in this work structural and aerodynamic damping/excitation of a certain mode of vibration are often compared, it is convenient to also express aerodynamic damping in terms of the damping ratio instead of using the logarithmic decrement:

$$D_{\mathrm{a}} = \frac{W_{\mathrm{a}}}{4\pi E_{\mathrm{kin,max}}}. \tag{2.11}$$

W_{a} and W_{s} are, in this work, defined to be *positive* when work is going *out* of the structure. Thus $D_{\mathrm{a}} > 0$ describes aerodynamically damped vibrations but it can also attain negative values in case of aerodynamic excitation. The relationship between the damping ratio and the logarithmic decrement is

$$D = \frac{\delta}{\sqrt{(2\pi)^2 + \delta^2}} \tag{2.12}$$

which can be approximated by $D \approx \frac{\delta}{2\pi}$ for small $\delta \ll 1$. Since D_{a} is a function of the aerodynamic influence, it follows that D_{a} can be also a nonlinear function of the amplitude as shown in [71], where the influence of different contact conditions in the shroud on the aerodynamic damping is investigated.

In order to get a better picture of a blade row's flutter characteristics, a flutter curve can be helpful. For a flutter curve, δ (or D_{a}) is typically plotted as a function of the IBPA or ND for a single mode family. An example of a simple flutter curve is depicted in **Figure 2.5**, where the flutter curve has the form of a simple sine wave, which is the case when only the aerodynamic coupling between direct neighbouring blades is considered. It should be noticed, that in many cases the flutter curve does not have the form of a simple sine wave due to the frequency dependency of the mode shape with respect to the ND (for structurally coupled blades), acoustic resonances or other physical effects.

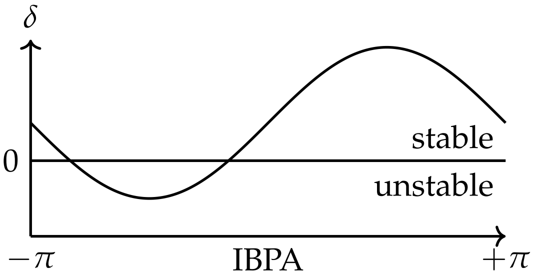

Figure 2.5: A simple flutter curve (δ as a function of IBPA).

2.3.1 Flutter-Free and Flutter-Tolerant Design

Flutter avoidance, where the flutter curve is required to reside completely in the stable region, has become a dominant design constraint with regard to both compressor [40] and turbine blades [66]. This design goal often competes with the goals for maximum efficiency and low weight and thus a trade-off is inevitable. For modern aircraft engines however, a high efficiency and reduced weight are important factors for reducing the fuel consumption and emissions. It is currently explored to overcome the strict requirement of flutter avoidance by flutter tolerance, where a dynamic instability is permitted as long

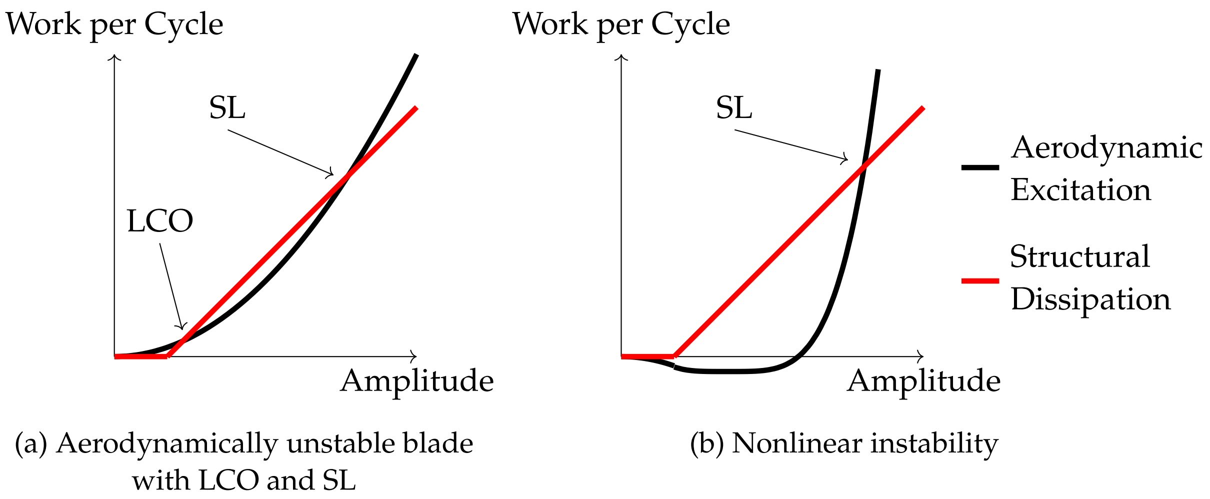

(a) Aerodynamically unstable blade with LCO and SL

(b) Nonlinear instability

Figure 2.6: Idealized examples of aerodynamic work and structural dissipation vs. vibration amplitude.

as the flutter-induced vibrations remain bounded at an acceptably low level. This change in design paradigm has the potential to further improve aerodynamic performance, and thus to reduce emissions and save resources.

Flutter-induced vibration amplitudes can be limited by dissipation in contact interfaces like tip shroud interfaces, blade root joints or under platform dampers. In the case of tip shroud interfaces for example, a high amount of dissipation can occur above a certain amplitude level, when the tangential contact forces exceed the normal pressure times the friction coefficient (limit friction force). Then the contact interfaces start to slide with a relative motion (also known as macro slip). Micro slip, where the contact stiffness is to a large degree retained (also during dissipation), occurs e.g. in blade root joints or under platform dampers. Its effect on the vibration shape and frequency in case of turbomachinery flutter is in most cases negligible and thus in the following the focus lies on shroud contact interfaces where macro slip is expected.

An idealized example of dry friction dissipation as a function of the vibration amplitude is shown in **Figure 2.6(a)** (red line). For small amplitudes the contact interface remains in sticking conditions (no dissipation) and starts to increase once the limit friction force is exceeded. In the case of an aerodynamically unstable blade row (black line), vibrations can grow until they evolve in e.g. a Limit Cycle Oscillation (LCO) where the aerodynamic excitation work is balanced by the dissipative work, see the intersection marked as 'LCO' in **Figure 2.6(a)**. An example of a transient vibration evolving towards a stable LCO is illustrated in **Figure 2.4(c)**. An LCO is a periodic limit state with a single fundamental oscillation frequency.

In **Figure 2.6(a)** a further intersection is labeled Stability Limit (SL), which denotes an unstable LCO due to balance of energy considerations. In this case the aerodynamic excitation grows faster than the structural dissipation: for amplitudes above the SL, more aerodynamic work is going into the structural vibration than the structure is able to dissipate and the amplitude increases possibly above critical stress levels. Amplitudes below the SL will most likely decay in this example towards the LCO. It should be noticed here that a stable LCO (due to energy balance considerations) can still be asymptotically unstable, this however will be discussed later.

Another phenomenon which has not been studied until now is nonlinear instability (NLI). Here, a vibrating mode is aerodynamically stable for small amplitudes but becomes unstable for larger vibrational amplitudes due to nonlinear effects. This is illustrated in **Figure 2.6(b)**, where the aerodynamic excitation is negative (acts as damping) up to an amplitude level, where the excitation switches sign and intersects the structural dissipation work and thus a stability limit arises.

For the evaluation of flutter-tolerant components it is crucial to have numerical methods available which can estimate the resulting vibrational amplitude of the above discussed limit states and reveal stability limits. Furthermore the analysis of nonlinear vibrations where nonlinear instability is expected is also of interest. Such analysis is challenging because friction contact interfaces in the shroud can influence the mode shape and vibration frequency, as already outlined in this chapter. Consequently, unidirectional analysis methods, which evaluate the aerodynamic forces based on a preliminary structural analysis as used in the past, may fail in predicting the resulting nonlinear vibrations.

2.4 Forced Response Vibrations in Turbomachinery

In case of forced response, the aerodynamic loads result from the rotation of the blades relative to the inhomogeneous pressure field in the circumferential direction. Pressure inhomogeneities are caused by aerodynamic interactions between the stator and rotor blade rows as well as non-homogeneous inflow or outflow conditions. An example of the former are the wakes of the upstream blade row. Possible resonances are analyzed using the Campbell diagram, see **Figure 2.7**. For this purpose, the relevant excitation order(s) and the natural frequency(-ies) are plotted as a function of the rotation speed and possible crossing points are identified. As a rule, resonances with the lowest-frequency eigenmodes within the operating range are avoided. However, due to the wide operating ranges and the diverse excitation mechanisms, resonances with higher-frequency modes cannot be avoided. For the remaining resonances, fatigue must be analyzed on the basis of calculated vibration stresses.

2.5 Limit State Types

The presence of negative aerodynamic damping or external excitation (forced response) and structural dissipation such as dry friction can lead to different limit states. The resulting limit states of the dynamical system can be of different type. A trivial limit state

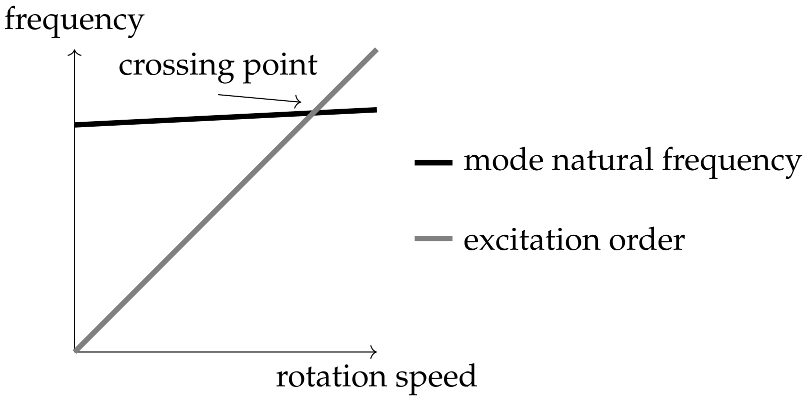

Figure 2.7: Simplified schematic of a Campbell diagram.

is a fixed point. For turbomachinery blade vibrations, one fixed point is the solution with zero deflection (considering the hot configuration as a reference, where centrifugal forces and static aerodynamic loads are accounted for). When unbounded growth occurs, this is denoted as divergence. Next, limit cycle oscillations (LCOs) are another possible limit state as already mentioned and depicted in **Figure 2.4(c)**. In the case of LCOs, a measure of motion $u(t)$ is periodic in time with a period length $T > 0$:

$$\boldsymbol{u}(t) = \boldsymbol{u}(t+T). \tag{2.13}$$

In a phase diagram, where e.g. position over velocity of a blade tip motion is plotted, the trajectory of an LCO has the form of a closed curve (see, for example, **Figure 7.5(a)**). Due to the periodicity, the motion $u(t)$ of an LCO can be expressed as a Fourier series

$$\boldsymbol{u}(t) = \Re\left\{\sum_{j=-\infty}^{\infty} \hat{\boldsymbol{u}}_j e^{\mathrm{i}j\omega t}\right\} \tag{2.14}$$

with $\omega = \frac{2\pi}{T}$ as the fundamental frequency. Additionally, an LCO has the property, that at least one trajectory of the dynamic system is going into the closed curve. If all trajectories joining the closed curve do it forward in time, the LCO is called a stable LCO. An LCO which is not stable is considered to be unstable in this work, however it should be mentioned that there are also other possibilities besides these two.

Oscillations with multiple incommensurable fundamental frequencies are denoted as limit torus oscillations (LTOs) or as quasi-periodic. In the case of two fundamental frequencies (a 2-torus), the trajectory in phase space lies on a torus. For two base frequencies ω_1 and ω_2, the motion can also be be expressed as a Fourier series:

$$\boldsymbol{u}(t) = \Re\left\{\sum_{(j,k)\in\mathbb{Z}^2} \hat{\boldsymbol{u}}_{j,k} e^{\mathrm{i}(j\omega_1 + k\omega_2)t}\right\}. \tag{2.15}$$

Furthermore strange attractors, e.g. chaotic motion, exist which are however out of scope of this work.

2.6 Evaluation of Aerodynamic Forces by CFD

For unidirectional or bidirectional numerical analysis of turbomachinery blade vibrations the evaluation of the aerodynamic force $\boldsymbol{f}^{\mathrm{a}}$ is necessary and is typically done by Computational Fluid Dynamics (CFD). The industrial standard for turbomachinery CFD is based on the Navier-Stokes equations for compressible fluids:

$$\frac{\partial \varrho}{\partial t} + \nabla \cdot (\varrho \boldsymbol{u}) = 0 \tag{2.16}$$

$$\frac{\partial \varrho \boldsymbol{u}}{\partial t} + \nabla \cdot (\varrho \boldsymbol{u} \otimes \boldsymbol{u}) = -\nabla p + \nabla \cdot \boldsymbol{\tau} \tag{2.17}$$

$$\frac{\partial \varrho E}{\partial t} + \nabla \cdot (\varrho \boldsymbol{u} H) = \nabla \cdot (\boldsymbol{\tau} \cdot \boldsymbol{u} - \boldsymbol{q}(T)) \tag{2.18}$$

$$\boldsymbol{u}|_{\text{blade surface}} = \dot{\boldsymbol{x}}|_{\text{blade surface}} \tag{2.19}$$

where $\varrho, \boldsymbol{u}$, E and H are the density, velocity vector, total energy and total enthalpy, respectively. $\boldsymbol{\tau}$ denotes the Cauchy stress tensor. The vector $\boldsymbol{q}(T)$ denotes the heat flux and the pressure p, temperature T, total enthalpy H and total energy E are related by laws of thermodynamics and an appropriate gas law, for example, ideal gas. A direct simulation of the Navier-Stokes equations requires a high amount of computational resources since very small turbulent flow scales would need to be resolved. Thus in most cases Reynolds averaging is applied yielding the Unsteady Reynolds Averaged Navier-Stokes (URANS) equations which removes the necessity of resolving turbulent length scales. This however introduces additional equations and terms in the fluid equations which must be closed with an empirical turbulence model. On solid surfaces, the no-slip boundary condition is applied to the fluid velocity. Thus, on a deforming blade surface, the fluid couples to the structural motion $\boldsymbol{x}$ which is expressed by Eq. (2.19).

2.6.1 Consideration of the Blade Motion

For the calculation of the fluid motion in the context of dynamic blade vibrations, the motion of the blade surface must be considered as a boundary condition for the fluid equations, as already mentioned in Section 2.6. These boundary conditions can be implemented in different ways. One possibility is to use the immersed boundary (IB) method, which can be sub-classified into diffuse interface IB (e.g. by using artificial body forces) or sharp interface IB methods (e.g. the cut-cell method) [60]. A disadvantage of the IB methods is, that the mesh resolution close to the blade surface is not trivial to be optimized for the boundary layer since it changes its position over time while the mesh stays fixed. Thus, for turbomachinery flows with high Reynolds numbers, the usage of a moving mesh is preferable since the refined mesh close to the blade surface is always aligned with the boundary layer. For a moving mesh $\chi(\boldsymbol{u}^{\mathrm{s}})$, the flux formulation of the spatial discretization must be modified to account for the motion of the cell faces. This requires the Arbitrary Lagrangian-Eulerian (ALE) formulation of the fluid equations [61] in conjunction with the Geometric Conservation Law (GCL) [72] for a correct treatment of the numerical flux. The resulting semi-discrete form of the fluid equations can simply be formulated as

$$\dot{\boldsymbol{u}}^{\mathrm{a}} + \boldsymbol{r}(\boldsymbol{u}^{\mathrm{a}}, \chi(\boldsymbol{u}^{\mathrm{s}}), \dot{\chi}(\dot{\boldsymbol{u}}^{\mathrm{s}})) = \boldsymbol{0} \tag{2.20}$$

where $\boldsymbol{r}$ contains the spatial discretization. The vector $\boldsymbol{u}^{\mathrm{a}}$ not only contains the unknown conservative flow variables but also the volume of the mesh cells since these also depend on time.

2.6.2 Non-Reflecting Boundary Conditions

For numerical flow analysis, if the system is not closed, inflow and outflow boundary conditions are necessary. Indeed, the best approach for a realistic turbomachinery model is to include the neighbouring blade rows in the simulation. In the case of turbomachinery CFD analysis, neighboring stages of a blade row of interest are often neglected and replaced by artificial inflow (in upstream direction) and outflow (in downstream direction) boundaries, since the consideration of additional neighboring rows is computationally very expensive. Although it was shown that the consideration of adjacent blade rows alter the flutter behavior of a cascade [29], a single row model with (artificial) inflow and outflow boundaries can still be considered as representative.

For artificial inflow and outflow boundaries, Non-Reflecting Boundary Conditions (NRBCs) are employed, which try to mimic the behavior of an infinite duct attached to the inlet (exit) of the blade row in order to prevent unphysical reflections at the inflow (outflow) boundaries. Different boundary condition methods exist which vary with respect to the degree of reflection, computational costs and robustness/stability. For the very simple and straight forward one-dimensional Riemann boundary conditions [38], viscous effects are neglected and the Euler equations are linearized where only the direction normal to the boundary is considered for the spatial derivation:

$$\frac{\partial \boldsymbol{u}^{\mathrm{a}}}{\partial t} + \left.\frac{\partial \boldsymbol{f}}{\partial \boldsymbol{u}^{\mathrm{a}}}\right|_{\boldsymbol{u}_0^{\mathrm{a}}} \frac{\partial \boldsymbol{u}^{\mathrm{a}}}{\partial x} = 0 \tag{2.21}$$

where $\left.\frac{\partial \boldsymbol{f}}{\partial \boldsymbol{u}^{\mathrm{a}}}\right|_{\boldsymbol{u}_0^{\mathrm{a}}}$ denotes the flux Jacobian evaluated around the mean flow. Using an eigenvalue analysis, the flow variables can be related to characteristic variables $\boldsymbol{c}^{\mathrm{a}} = \boldsymbol{L}\boldsymbol{u}^{\mathrm{a}}$, where $\boldsymbol{L}$ contains the left eigenvectors from the eigenvalue analysis. The characteristic variables allow to distinguish incoming and outgoing waves of the flow which can then be set to zero for outoing waves and to prescribed boundary target values for incoming waves. One-dimensional boundary conditions however exhibit spurious, numerical reflections at the boundary [54] and thus can deteriorate the flow solution leading to an over- or under-prediction of the flutter intensity. Especially for turbomachinery simulations, two-dimensional spectral NRBCs have been shown to yield increased accuracy [54], where wavelike perturbations with a periodic frequency ω of the form

$$\boldsymbol{u}^{\mathrm{a}} = \Re\left\{\hat{\boldsymbol{u}}^{\mathrm{a}} e^{\mathrm{i}(kx+m\varphi-\omega t)}\right\} \tag{2.22}$$

are considered with k and m denoting the wave numbers along the cylindrical coordinates x and φ, respectively. Appropriately, the Euler equations in two dimensions are considered and linearized (the circumferential coordinate is additionally considered). Since k will turn into the sought eigenvalues of the subsequent eigenvalue analysis, ω and m need to be specified in advance which is problematic for FSI simulations in the time domain, since especially the flutter frequency is part of the solution. The spectral NRBCs are especially suited for frequency domain methods (e.g. harmonic balance) since these are already formulated in the frequency domain. For time domain simulations, a reformulation is necessary. Promising time local higher-order NRBCs [26] do not require a fundamental frequency and deliver a better reflection behavior compared to one-dimensional BCs but currently are less robust and take more time to converge compared to two-dimensional spectral NRBCs.

An unresolved problem, even for time local higher-order NRBCs in the time domain, is the determination of the mean flow used for the linearization of the Euler equations, if the perturbation frequency of the unsteady flow is unknown. Temporal averaging of the flow is necessary in order to meet the user prescribed values at the boundary. This requires the correct perturbation frequency for an efficient implementation of time domain NRBCs. If this frequency is unknown, either a very long history storage of the flow is necessary for temporal averaging (and even then an error is present), or the perturbation frequency must be determined during the simulation. The last option, however, adds another stability problem into the whole numerical model and is, to the authors knowledge, not yet implemented in any CFD code.

Simulation of unsteady flows, where the perturbation frequency is not known a priori, can be found in e.g. [19]. In this and similar simulations in literature, mostly conventional one-dimensional NRBCs are employed, however in combination with greatly enlarged computational domains, sponge layers and nozzles at the exit. While this is a solution to ease numerical reflections at the boundaries and circumvent above mentioned problems, the computational costs significantly increase, especially since the domain must span the full annulus. Additionally, some reflections still occur at a nozzle placed close to the exit of the domain.

2.6.3 Aerodynamic Influence Coefficients

The aerodynamic forces induced by blade vibrations can be modeled in terms of influence coefficients in the frequency domain [66, 51] similar as in Eq. (2.31). These are formulated with respect to a selected set of structural modes $\boldsymbol{\psi}_i$. To predict these coefficients, a harmonic deformation in each mode is imposed and the resulting aerodynamic force, more specifically its fundamental Fourier coefficient, is determined using computational fluid dynamics, e.g. by solving the unsteady URANS equations. The force induced by unit deformation in mode j, acting on mode i is the influence coefficient a_{ij}. This way, a modal AIC coefficient matrix $\boldsymbol{G} = [a_{ij}]$ is set up and the Fourier coefficients of aerodynamic forces induced by blade vibration are approximated according to

$$\hat{\boldsymbol{f}}^{\mathrm{a}} \approx \boldsymbol{G}(\omega)\hat{\boldsymbol{u}}^{\mathrm{s}}, \tag{2.23}$$

i.e. it is assumed, that the harmonic aerodynamic forces acting on a blade can be determined by a linear superposition from the aerodynamic influence of all blades. $\boldsymbol{G}$ is a complex-valued matrix; the real parts of the diagonal entries are associated with the aerodynamic stiffness and the imaginary parts with the aerodynamic damping. It generally depends on the frequency ω of the imposed vibration. If the actual vibration frequency is accurately known, the frequency dependence can be neglected [44]. For cases where the relevant frequency range is large, a piecewise linear interpolation was proposed in [14]. Just as with the conventional energy method, an advantage of the method of influence coefficients is the decoupling of computational fluid dynamics and nonlinear structural dynamics: Once the AIC matrix is set up, one has a closed-form expression for the aerodynamic forces. This can subsequently be used to compute the LCO by considering the balance with the nonlinear structural forces. As the computational effort for setting up the AIC matrix grows linearly with the number of modes, the appropriate choice of a modal basis for describing structural vibration is a crucial aspect.

2.6.4 Fluid-Structure Surface Data Interpolation

The numerical analysis of aeroelastic blade vibration requires the transfer of mechanical quantities (force/displacement) between the fluid and structure domains. At the fluid-structure interface, the meshes of both domains are in most cases non-matching due to the different discretization methods and meshing algorithms. Hence, the fluid pressure/forces and structural displacements and velocities must be transferred between the two solvers by interpolation. For unidirectional coupling, unsteady displacement data could, for example, be interpolated onto the fluid mesh in order to calculate the unsteady flow and the resulting aerodynamic forces on the blade surface. In case of a bidirectional FSI solver scheme, the surface pressure/forces must be interpolated in the other direction.

Common interpolation techniques are nearest neighbor interpolation, projection methods and interpolation by splines [4]. Whichever interpolation method is chosen, the outcome can be formulated as a linear operation

$$\boldsymbol{q}_{\text{target}} = \boldsymbol{L}\boldsymbol{q}_{\text{source}}, \tag{2.24}$$

where $\boldsymbol{q}_{\text{target}}$ denotes the interpolated values on the target mesh and $\boldsymbol{q}_{\text{source}}$ the values of the source mesh. One interpolation matrix $\boldsymbol{L}_{\text{Structure}\to\text{Fluid}}$ is required for the interpolate of the displacements (and velocities) from the structure to the fluid mesh surface. When interpolation of surface pressure/forces from the fluid mesh to the structure mesh is required (e.g. in case of a bidirectional FSI simulation or a forced response analysis), an interpolation matrix $\boldsymbol{L}_{\text{Fluid}\rightarrow\text{Structure}}$ is necessary, which interpolates the surface forces in the other direction. In principal, for both matrices, any interpolation technique can be chosen. If interpolation techniques for both directions, which exactly recover a constant (homogeneous) quantity on the target mesh, are applied, then this is denoted as a consistent interpolation. A consistent interpolation is however not guaranteed to be conservative. A conservative interpolation means, that the mechanical work transferred across the interface is conserved, which for some applications is favorable. For a conservative interpolation, one of the two interpolation matrices is derived from the other one, see e.g. [3].

2.7 Time Integration Methods

The structure and fluid dynamics Eqs. (2.6) and (2.20) can be solved with numerical time integration, for example, with the Newmark scheme [45], Runge-Kutta schemes [5] or Backward Difference Formula (BDF) schemes. While time integration schemes can simulate transient phenomena and limit states such as LCOs, LTOs and chaos, they require a high amount of computational resources, since many time steps must be computed until convergence (provided there is a stable limit set) and often full blade row models for the analysis of flutter are necessary. Additionally, time integration schemes can require a very small time step size, if the numerical stiffness of the equation to be solved is high. A numerical stiff equation means that numerical methods are likely to become numerically unstable when applied it. Especially in structural dynamics, the numerical stiffness of Eq. (2.6) can become very high when nonlinear contact forces are resolved realistically and more involved schemes need to be deployed, see e.g. [64].

To overcome the high computational effort of numerical time integration, nonlinear frequency domain methods such as the Harmonic Balance (HB) method have been developed which are now popular in both structural dynamics and computational fluid dynamics. Compared to numerical time integration, the computational effort is typically reduced by two to four orders of magnitude [29]. The reasons for the computational advantages of HB are: (a) HB can efficiently deal with stiff differential equations. (b) HB avoids the costly simulation of the usually long transient. (c) A few harmonics often suffice to resolve the periodic oscillation. (d) Assuming symmetric behavior within the blade row, the computational domains can be reduced to a reference sector (only one blade or one passage) with appropriate cyclic symmetry boundary conditions. First attempts to co-simulate cascade flutter in the time or frequency domain are limited to linear [15, 63, 6, 22] or single-degree-of-freedom nonlinear [A, B] structural models. The HB method is used extensively in this work for both physical domains (fluid + structure).

For frequency domain methods, a solution is approximated by a truncated Fourier series,

$$\boldsymbol{u}(t) \approx \Re\left\{\sum_{k=0}^{H} \mathrm{e}^{ik\omega t}\hat{\boldsymbol{u}}_k\right\}, \tag{2.25}$$

where t denotes time, $\mathrm{i} = \sqrt{-1}$ is the imaginary unit, H is the harmonic truncation order, ω is the fundamental oscillation frequency and $\hat{\boldsymbol{u}}_k^{\mathrm{s}}$ are the Fourier coefficients. Following the HB concept, Eq. (2.25) is inserted into a nonlinear equation and the residual is subsequently made orthogonal to the Fourier basis by a Galerkin projection. Thus, in the case of HB, the residual as well as the unknowns reside in the frequency domain. Applying the HB technique to Eq. (2.6) [35] yields the algebraic system of equations

$$\boldsymbol{r}^{\mathrm{s}}(\hat{\boldsymbol{u}}^{\mathrm{s}}, \omega, \hat{\boldsymbol{f}}^{\mathrm{a}}) := \boldsymbol{S}(\omega)\hat{\boldsymbol{u}}^{\mathrm{s}} + \hat{\boldsymbol{f}}^{\mathrm{c}}(\hat{\boldsymbol{u}}^{\mathrm{s}}) - \hat{\boldsymbol{f}}^{\mathrm{a}} = \boldsymbol{0}, \tag{2.26}$$

where $\boldsymbol{r}^{\mathrm{s}}$ denotes the structural residual. The Fourier coefficients are here stacked as $\hat{\boldsymbol{u}}^{\mathrm{s}} = [\hat{\boldsymbol{u}}_0^{\mathrm{s}}; \hat{\boldsymbol{u}}_1^{\mathrm{s}}; \ldots; \hat{\boldsymbol{u}}_H^{\mathrm{s}}]$, where ; denotes vertical concatenation. $\boldsymbol{S}(\omega)$ is the block diagonal dynamic stiffness matrix, which describes the linear-elastic and linear inertia forces and thus depends on $\boldsymbol{M}$ and $\boldsymbol{K}$. $\hat{\boldsymbol{f}}^{\mathrm{c}}$ and $\hat{\boldsymbol{f}}^{\mathrm{a}}$ are the vectors of Fourier coefficients of the contact and aerodynamic forces, and are stacked analogously to $\hat{\boldsymbol{u}}^{\mathrm{s}}$. Nonlinear aerodynamic and contact forces introduce coupling among the harmonics. The nonlinear contact forces $\hat{\boldsymbol{f}}^{\mathrm{c}}$ can be computed with the alternating frequency-time (AFT) scheme, which can mathematically be expressed as

$$\hat{\boldsymbol{f}}^{\mathrm{c}}(\hat{\boldsymbol{u}}^{\mathrm{s}}) = \boldsymbol{\mathcal{F}}\boldsymbol{f}^{\mathrm{c}}(\boldsymbol{\mathcal{F}}^{-1}\hat{\boldsymbol{u}}^{\mathrm{s}}) \tag{2.27}$$

where $\boldsymbol{\mathcal{F}}$ denotes the discrete Fourier transform (DFT) and $\boldsymbol{\mathcal{F}}^{-1}$ its inverse (iDFT). By applying the iDFT to the Fourier coefficients $(\boldsymbol{\mathcal{F}}^{-1}\hat{\boldsymbol{u}}^{\mathrm{s}})$, $\boldsymbol{u}^{\mathrm{s}}$ is computed at discrete time samples, which allows the nonlinear function to be evaluated $\boldsymbol{f}^{\mathrm{c}}$ in the time domain. Finally, the nonlinear force evaluated at the discrete time samples is transformed back into the frequency domain by applying the DFT. For the evaluation of $\hat{\boldsymbol{f}}^{\mathrm{a}}$ a CFD solver (or some other approximation) is necessary for the calculation of the Fourier coefficients.

Similar to the structural side, applying the HB method to the fluid equations (Eq. (2.20)) yields

$$\boldsymbol{r}^{a}(\hat{\boldsymbol{u}}^{\mathrm{a}}, \hat{\boldsymbol{u}}^{\mathrm{s}})_k := \mathrm{i}k\omega\hat{\boldsymbol{u}}_{\mathrm{k}}^{\mathrm{a}} + \boldsymbol{\mathcal{F}}\boldsymbol{r}\left(\boldsymbol{\mathcal{F}}^{-1}\hat{\boldsymbol{u}}^{\mathrm{a}}, \boldsymbol{\mathcal{F}}^{-1}\hat{\chi}(\hat{\boldsymbol{u}}^{\mathrm{s}}), \frac{\partial}{\partial t}\boldsymbol{\mathcal{F}}^{-1}\hat{\chi}(\hat{\boldsymbol{u}}^{\mathrm{s}})\right)|_{\mathrm{k}} = \boldsymbol{0} \tag{2.28}$$

for each fluid harmonic $k \in \{0, 1, 2, \ldots, H^{\mathrm{a}}\}$ where again $\hat{\boldsymbol{u}}^{\mathrm{a}} = [\hat{\boldsymbol{u}}_0^{\mathrm{a}}; \hat{\boldsymbol{u}}_1^{\mathrm{a}}; \ldots; \hat{\boldsymbol{u}}_{\mathrm{H^a}}^{\mathrm{a}}]$.

An extension to the HB method is the multidimensional HB method, where multiple fundamental frequencies can be considered [33, 28]. Essentially, the ansatz presented in Eq. (2.25) is formulated with a finite amount of fundamental frequencies ω_j. A non-trivial task however is the selection of the harmonics of the multidimensional Fourier method which highly depends on the considered problem.

2.8 Numerical Analysis of Blade Vibrations

Numerous numerical methods of different fidelity levels are available for the FSI analysis of turbomachinery blades. In the previous sections some aspects of turbomachinery flutter and forced response vibrations are presented together with basic numerical modeling of the fluid and the structure. In the following, important methods for the simulation of flutter and forced response vibrations are presented.

2.8.1 Energy Method

The energy method developed by Carta [8], in the remainder of this work also denoted "conventional energy method", has been used for a long time as a standard numerical analysis method for turbomachinery flutter. For the energy method the following prerequisites are assumed [57]:

- nonlinear structural effects (dry friction) leading to a change of mode shape or frequency are negligible
- the mass ratio ($\frac{\varrho_{\mathrm{air}}}{\varrho_{\mathrm{blade}}}$) is very low
- aerodynamic forces compared to the structural stiffness are small
- the frequency separation of modes with the same ND is sufficiently large
- the (modal) aerodynamic forces behave linearly.

The energy method evaluates the aerodynamic work due to a prescribed harmonic motion of a blade mode. For a mode $\boldsymbol{\psi}^{\mathrm{stick}}$ of interest, the work exerted on the structure/blade by aerodynamic forces per period W^{a} is determined for a prescribed modal amplitude $\hat{u}$. In this step, a harmonic displacement $\boldsymbol{q}_{\mathrm{Fluid}} = \Re \left\{ \boldsymbol{L}\, \boldsymbol{\psi}^{\mathrm{stick}} \hat{u} e^{\mathrm{i}\omega^{\mathrm{stick}} t} \right\}$ (where $\boldsymbol{L}$ denotes the interpolation matrix of the displacements) and velocity $\dot{\boldsymbol{q}}_{\mathrm{Fluid}}$ are imposed as boundary condition for the fluid. Additionally, the fluid domain is typically reduced to a single sector with appropriate phase-lag BCs. Since the structure is treated as linear, also the contact forces need to be linearized, which in most cases means to assume sticking contact conditions which is denoted by the superscript "stick". After solving the fluid equations (with frequency or time domain methods) the (modal) aerodynamic work can be evaluated for one period T according to

$$
\begin{aligned}
W_{\mathrm{a}}(\hat{u}) &= \int_0^T \left(\dot{\boldsymbol{q}}_{\mathrm{Fluid}}\right)^{\mathrm{T}} \boldsymbol{f}^{\mathrm{a}}_{\mathrm{Fluid}} \mathrm{d}t \\
&= \int_0^T \Re\left\{\mathrm{i}\omega^{\mathrm{stick}} \boldsymbol{L}\, \boldsymbol{\psi}^{\mathrm{stick}} \hat{u} \mathrm{e}^{\mathrm{i}\omega^{\mathrm{stick}} t}\right\}^{\mathrm{T}} \Re\left\{\hat{\boldsymbol{f}}^{\mathrm{a}}_{1,\mathrm{Fluid}}\, \mathrm{e}^{\mathrm{i}\omega^{\mathrm{stick}} t}\right\} \mathrm{d}t \\
&= \int_0^{2\pi} \Re\left\{\mathrm{i}\boldsymbol{L}\boldsymbol{\psi}^{\mathrm{stick}} \hat{u} \mathrm{e}^{\mathrm{i}\tau}\right\}^{\mathrm{T}} \Re\left\{\hat{\boldsymbol{f}}^{\mathrm{a}}_{1,\mathrm{Fluid}}\, \mathrm{e}^{\mathrm{i}\tau}\right\} \mathrm{d}\tau \\
&= \int_0^{2\pi} \left(\mathrm{i}\boldsymbol{L}\boldsymbol{\psi}^{\mathrm{stick}} \hat{u} \frac{\mathrm{e}^{\mathrm{i}\tau}}{2} + \overline{\mathrm{i}\boldsymbol{L}\boldsymbol{\psi}^{\mathrm{stick}} \hat{u}} \frac{\mathrm{e}^{-\mathrm{i}\tau}}{2}\right)^{\mathrm{T}} \left(\hat{\boldsymbol{f}}^{\mathrm{a}}_{1,\mathrm{Fluid}}\, \frac{\mathrm{e}^{\mathrm{i}\tau}}{2} + \overline{\hat{\boldsymbol{f}}^{\mathrm{a}}_{1,\mathrm{Fluid}}}\, \frac{\mathrm{e}^{-\mathrm{i}\tau}}{2}\right) \mathrm{d}\tau \\
&= 2\pi \left(-\mathrm{i}\left(\boldsymbol{L}\boldsymbol{\psi}^{\mathrm{stick}}\right)^{\mathrm{H}} \hat{\boldsymbol{f}}^{\mathrm{a}}_{1,\mathrm{Fluid}}/4 + \mathrm{i}\left(\boldsymbol{L}\boldsymbol{\psi}^{\mathrm{stick}}\right)^{\mathrm{T}} \overline{\hat{\boldsymbol{f}}^{\mathrm{a}}_{1,\mathrm{Fluid}}}/4\right) \hat{u} \\
&= \Re\left\{-\mathrm{i}\pi\left(\boldsymbol{L}\boldsymbol{\psi}^{\mathrm{stick}}\right)^{\mathrm{H}} \hat{\boldsymbol{f}}^{\mathrm{a}}_{1,\mathrm{Fluid}}\right\} \hat{u} \qquad (2.29)
\end{aligned}
$$

where $\hat{\boldsymbol{f}}^{\mathrm{a}}_{1,\mathrm{Fluid}}$ denotes the harmonic aerodynamic force vector containing the nodal surface forces which is obtained according to

$$
\hat{\boldsymbol{f}}^{\mathrm{a}}_{1,\mathrm{Fluid}} = \frac{2}{T} \int_0^T \mathrm{e}^{-\mathrm{i}\omega^{\mathrm{stick}} t} \boldsymbol{f}^{\mathrm{a}}_{\mathrm{Fluid}}(t) \mathrm{d}t. \qquad (2.30)
$$

In the above Eq. (2.30), the factor 2 is necessary if a half spectrum is used for the reconstruction. It should be noticed, that the instantaneous nodal forces $\boldsymbol{f}^{\mathrm{a}}_{\mathrm{Fluid}}(t)$ should be evaluated under consideration of the deformed surface in.

Finally, W_{a} is used to determine either the damping ratio D_{a} or the logarithmic decrement $\delta \approx -\frac{W_{\mathrm{a}}}{2E_{\mathrm{kin,max}}}$. It is assumed, that the aerodynamic damping D_{a} or δ is invariant with respect to the vibration amplitude, which implies the assumption of a linear aerodynamic force

$$
\hat{f}^{\mathrm{a}} = \left(\boldsymbol{L}\boldsymbol{\psi}^{\mathrm{stick}}\right)^{\mathrm{H}} \hat{\boldsymbol{f}}^{\mathrm{a}}_{1,\mathrm{Fluid}} \approx a\hat{u}, \qquad (2.31)
$$

where a denotes the influence coefficient. In case of a flutter-free design it is sufficient to require that $D_{\mathrm{a}}, \delta > 0$ or in case of the presence of structural damping $D_{\mathrm{a}} + D_{\mathrm{s}} > 0$. If nonlinear structural damping data $W_{\mathrm{s}}(\hat{u})$ is present, an LCO amplitude $\hat{u}_{\mathrm{LCO}}$ can be determined by requiring $W_{\mathrm{s}}(\hat{u}_{\mathrm{LCO}}) + W_{\mathrm{a}} = 0$.

2.8.2 Aeroelastic Eigenvalue Problem

An example of the application of the AICs is the analysis of the flutter stability via an aeroelastic eigenvalue problem. To start with, a ROM of the structure (e.g. obtained by modal truncation) as in Eq. (2.6) is considered. A harmonic motion $\boldsymbol{u}^{\mathrm{s}}(t) = \Re\left\{\hat{\boldsymbol{u}}^{\mathrm{s}}\mathrm{e}^{\mathrm{i}\lambda t}\right\}$ for the bladewise modes and the aerodynamic forces $\boldsymbol{f}^{\mathrm{a}}(t) = \Re\left\{\hat{\boldsymbol{f}}^{\mathrm{a}}\mathrm{e}^{\mathrm{i}\lambda t}\right\}$ is assumed with

$\lambda = \mathrm{i}\zeta + \omega$. Here, each coordinate in $\hat{\boldsymbol{u}}^{\mathrm{s}}$ corresponds to a single blade's mode shape and thus, for one mode family, the number of generalized coordinates N equals the number of blades. Inserting these assumptions into Eq. (2.6), and neglecting or linearizing $\boldsymbol{f}^{\mathrm{c}}$ yields

$$\left(\boldsymbol{K} - \lambda^2 \boldsymbol{M}\right) \hat{\boldsymbol{u}}^{\mathrm{s}} = \hat{\boldsymbol{f}}^{\mathrm{a}}. \tag{2.32}$$

Approximating the aerodynamic forces by AICs, Eq. (2.23) is inserted into Eq. (2.32), yielding the eigenvalue problem

$$\left(\boldsymbol{K} - \lambda^2 \boldsymbol{M} - \boldsymbol{G}(\omega)\right) \hat{\boldsymbol{u}}^{\mathrm{s}} = 0, \tag{2.33}$$

where coupling among the blades stems from the fully populated AIC matrix $\boldsymbol{G}$ (and possibly also from structural coupling between the blades accounted for in $\boldsymbol{K}$). When the vibration frequency is expected to be in the vicinity of the natural blade frequency, the frequency dependency of $\boldsymbol{G}(\omega)$ can be neglected and a generalized eigenvalue problem is obtained. Finally, D_{a} or δ can be determined from the decay rate ζ of the resulting modes ($\hat{\boldsymbol{u}}_i^{\mathrm{s}}$, λ_i) according to

$$D_{\mathrm{a}} = \frac{\zeta}{\sqrt{\omega^2 + \zeta^2}} \left(\approx \frac{\zeta}{\omega}\right) \tag{2.34}$$

provided that $D_{\mathrm{a}} < 1$. The AIC method can be applied to multiple mode shapes per blade and the dependency of $\boldsymbol{G}$ on ω can be accounted for in different ways, see e.g. [27, 57]. This, in contrast to the energy method, removes the requirements of sufficiently large frequency separation between modes, low density ratios and small aerodynamic forces compared to the structural stiffness, which allows to investigate special phenomena like coupled mode flutter [57]. However, nonlinear aerodynamic forces are still neglected.

2.8.3 Structural Analysis of Nonlinear Blade Vibrations with Numerical Path Continuation

Involved structural simulation methods exist for the investigation of nonlinear blade vibrations with frictional contact interfaces or other nonlinearities. In many cases the application of different ROM techniques (e.g. Craig-Bampton or Rubin method) in conjunction with FD methods (e.g. harmonic balance) leads to an algebraic system equal or similar to

$$\boldsymbol{r}^{\mathrm{s}}(\hat{\boldsymbol{u}}^{\mathrm{s}}, \omega) := \boldsymbol{S}(\omega)\hat{\boldsymbol{u}}^{\mathrm{s}} + \hat{\boldsymbol{f}}^{\mathrm{c}}(\hat{\boldsymbol{u}}^{\mathrm{s}}) = \boldsymbol{0}. \tag{2.35}$$

Eq. (2.35) could be solved with an iterative solver (e.g. the Newton-Raphson method). This solver type requires that the initial point lies in the basin of attraction of the sought solution. Thus, a sufficiently good guess for the initialization is required which can be a non-trivial task. For the analysis of blade vibrations, a single solution of Eq. (2.35) is sometimes not helpful, instead a whole solution curve, where a parameter of the mechanical system is varied is of interest. Such a parameter can be for example the (excitation) frequency ω in case of a forced response analysis or the aerodynamic excitation level in case of flutter. Numerical path continuation allows to compute such a solution path, which is explained in the following.

The complex valued system is transformed to real arithmetics by splitting the complex and real parts of $\boldsymbol{r}^{\mathrm{s}}$ and the unknowns according to

$$\tilde{\boldsymbol{R}}^{\mathrm{s}} = \begin{bmatrix} \Re\{\boldsymbol{r}^{\mathrm{s}}(\boldsymbol{X}^{\mathrm{s}})\} \\ \Im\{\boldsymbol{r}^{\mathrm{s}}(\boldsymbol{X}^{\mathrm{s}})\} \end{bmatrix} = \boldsymbol{0}, \tag{2.36}$$

where $\boldsymbol{X}^{\mathrm{s}} = [\Re\{\hat{\boldsymbol{u}}^{\mathrm{s}}\},\, \Im\{\hat{\boldsymbol{u}}^{\mathrm{s}}\},\, \omega]^{\mathrm{T}}$, if the frequency is considered as an unknown. Here, the imaginary part of the zeroth harmonic ($k = 0$) is discarded since the mean of the (real) time periodic signal can be represented by purely real coefficients, which is not reflected in the notation for simplicity. The aim is to compute a discretized solution path consisting of a finite number of solution points $\boldsymbol{X}^{\mathrm{s}}_{(n)}$ satisfying Eq. (2.36). An example of two points is depicted in **Figure 2.8**, however typically many solution points (sometimes in the order of a few hundred) are required to sufficiently resolve a solution path. Additionally, a constraint $r^{\mathrm{con}}(\boldsymbol{X}^{\mathrm{s}})$ is necessary in order to control the distance between two successive solution points and to ensure local uniqueness. Therefore, an extended residual

$$\boldsymbol{R}^{\mathrm{s}} = \begin{bmatrix} \tilde{\boldsymbol{R}}^{\mathrm{s}}(\boldsymbol{X}^{\mathrm{s}}) \\ r^{\mathrm{con}}(\boldsymbol{X}^{\mathrm{s}}) \end{bmatrix} = \boldsymbol{0} \tag{2.37}$$

is formulated. An example is the arc-length constraint [58]

$$r^{\mathrm{con}}\left(\boldsymbol{X}^{\mathrm{s}}_{(n+1)}\right) = ||(\boldsymbol{X}^{\mathrm{s}}_{(n+1)} - \boldsymbol{X}^{\mathrm{s}}_{(n)})||^2 - \Delta s^2 = 0, \tag{2.38}$$

where the step length Δs controls the distance between two successive solution points and thus has an effect on the resolution of the curve. Here, $||\cdot||$ denotes an appropriate norm.

The solution points are computed sequentially. Based on the last solution $\boldsymbol{X}^{\mathrm{s}}_{(n)}$, an estimate is made for the next point along the path by using a predictor (e.g. a tangent or secant predictor). An example is depicted in **Figure 2.8**, where a tangent predictor step is made,

$$\boldsymbol{X}^{\mathrm{s}}_{(n+1,i=0)} = \boldsymbol{X}^{\mathrm{s}}_{(n)} + \boldsymbol{t}\Delta s\,, \tag{2.39}$$

with $\boldsymbol{t}$ denoting the unit tangent of the solution curve at $\boldsymbol{X}^{\mathrm{s}}_{(n)}$, and Δs the step length. This estimate is then iteratively improved in a corrector step until the norm of the residual $||\boldsymbol{R}^{\mathrm{s}}(\boldsymbol{X})||$ falls below a numerical tolerance threshold. For the corrector step Eq. (2.37) is solved iteratively for $\boldsymbol{X}^{\mathrm{s}}_{(n+1)}$ with a Newton-Raphson scheme:

$$\boldsymbol{X}^{\mathrm{s}}_{(n+1,i+1)} = \boldsymbol{X}^{\mathrm{s}}_{(n+1,i)} - \left.\left(\frac{\partial \boldsymbol{R}^{\mathrm{s}}}{\partial \boldsymbol{X}^{\mathrm{s}}}\right)^{-1}\right|_{\boldsymbol{X}^{\mathrm{s}}_{(n+1,i)}} \boldsymbol{R}^{\mathrm{s}}\left(\boldsymbol{X}^{\mathrm{s}}_{(n+1,i)}\right) \tag{2.40}$$

where i denotes the Newton-Raphson iterations and the initial solution $\boldsymbol{X}^{\mathrm{s}}_{(n+1,i=0)}$ is provided by the predictor step. Subsequently, the next solution point is predicted. A good starting point for a solution path can reside in the linear regime, where it is easy to obtain

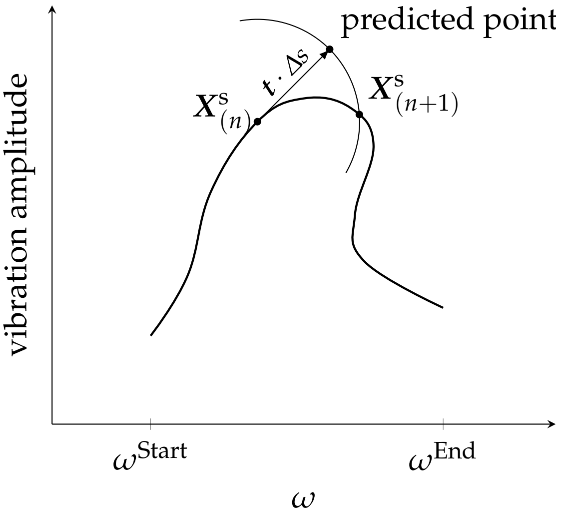

Figure 2.8: Numerical path continuation using a tangent predictor in combination with an arc-length constraint

a good initialization. A solution path is then computed while a suitable parameter which is tracked in order to consider a range of interest for the solution path. In the example shown in **Figure 2.8**, the frequency ω is used for tracking.

The use of involved modeling of the structure in combination with numerical path continuation provides a powerful basis for the analysis of blade vibrations. For example, in [51] a methodology is presented which combines the HB method with an approximate FRF matrix (see Section 2.2.2), which allows to compute a flutter induced LCO under consideration of linearized aerodynamic forces. In this approach the effect of the aerodynamic forces are extracted from a few aerodynamic influence coefficients of the linearized structural system. The suggested method utilizes numerical path continuation in order to retrieve an LCO solution for a specific level of aerodynamic excitation.

2.8.4 Nonlinear Modal Analysis

A method utilizing path continuation is the Nonlinear Modal Analysis (NMA) [32], which is presented in the following, since it serves as a basis for a refined energy method later in this work. The NMA can determine the mode shape $\boldsymbol{\psi}$ and frequency ω of the vibrations as functions of the blade vibration amplitude considering the influence of nonlinear contact forces. It is applied to the nonlinear frequency domain formulation of the reduced structural model Eq. (2.26) without aerodynamic forces (in vacuum), yielding the algebraic equation system,

$$\boldsymbol{S}_k(\omega^{\mathrm{nl}})\hat{\boldsymbol{u}}^{\mathrm{s}}_k + \hat{\boldsymbol{f}}^{\mathrm{c}}_k(\hat{\boldsymbol{u}}^{\mathrm{s}}) = 2D_{\mathrm{s}}\omega^{\mathrm{nl}}(\mathrm{i}k\omega^{\mathrm{nl}})\boldsymbol{M}^{\mathrm{cb}}_k\hat{\boldsymbol{u}}^{\mathrm{s}}_k, \quad k = 0, 1, \ldots, H^{\mathrm{s}}. \tag{2.41}$$

Here, $\boldsymbol{S}$ is the dynamic stiffness matrix, which is derived from the mass, stiffness and (possibly) other linear terms of the dynamic force balance. The term on the right hand side represents the mass-proportional excitation term in accordance with the definition in [32] and D_{s} is treated as a free parameter. Here, the effect of the flow is still neglected (as in the conventional energy method), but the nonlinear contact forces at the contact interfaces are considered. The NMA starts with a small amplitude preferably in the linear regime in which only sticking (but no frictional, $D_{\mathrm{s}} = 0$) contact conditions are present. By numerical path continuation, the amplitude-dependent mode shape $\boldsymbol{\psi}^{\mathrm{nl}}(\hat{u})$ and natural frequency $\omega^{\mathrm{nl}}(\hat{u})$ as functions of the modal amplitude $\hat{u}$ are obtained. The mode shape is mass normalized with respect to the first harmonic $k = 1$, i. e. $\left(\boldsymbol{\psi}_1^{\mathrm{nl}}\right)^{\mathrm{H}} \boldsymbol{M}_1^{\mathrm{cb}} \boldsymbol{\psi}_1^{\mathrm{nl}} = 1$ and the solution for a certain modal amplitude is recovered according to $\hat{\boldsymbol{u}}^{\mathrm{s}} = \boldsymbol{\psi}^{\mathrm{nl}}(\hat{u})\hat{u}$. If the same normalization for mode shapes is applied to the linear modes, the NMA is consistent with the linear system. In case a CMS method was used, the Fourier coefficients of the nodal displacement coordinates are recovered according to $\hat{\boldsymbol{q}}_{\mathrm{FE,k}} = \boldsymbol{T}_{\mathrm{cb,k}} \boldsymbol{\psi}_k^{\mathrm{nl}}(\hat{u})\, \hat{u}$. Finally, the work dissipated by dry friction can subsequently be evaluated from the recovered contact forces over one period or directly from D_{s}.

2.8.5 Modal Time Integration with AICs

Various approaches have been developed in order to predict saturated flutter vibrations (LCOs or LTOs) with time accurate or asymptotic methods. Especially the description of the structure in modal space is popular due to the relatively low computational burden and ease of implementation. Conceptually, the modal dynamic force balance Eq. (2.6) is integrated in time until a periodic (or quasi-periodic) steady state is reached, while the aerodynamic forces are approximated via linear functions of the (modal) displacements and velocities. For the nonlinear structural forces $\boldsymbol{f}^{\mathrm{c}}$, different friction models can be used in order to describe microslip or macroslip.

The description of the linear aerodynamic forces is derived from AICs, which implies the assumptions of linear aerodynamics and a harmonic blade motion. Since the AICs are in general complex coefficients, real valued matrices must be extracted for the description of the aerodynamic forces in the time domain. In case of blade wise modes these matrices can be extracted according to

$$\boldsymbol{K}^{\mathrm{a}} = \Re\left(\boldsymbol{G}(\omega_0)\right), \quad \boldsymbol{D}^{\mathrm{a}} = \Im\left(\frac{\boldsymbol{G}(\omega_0)}{\omega_0}\right) \tag{2.42}$$

for a fixed frequency ω_0 [43]. The aerodynamic stiffness and damping matrices K^{a} and D^{a} can be inserted into Eq. (2.6):

$$\boldsymbol{M}\ddot{\boldsymbol{u}}^{\mathrm{s}} - \boldsymbol{D}^{\mathrm{a}}\dot{\boldsymbol{u}}^{\mathrm{s}} + \left(\boldsymbol{K} - \boldsymbol{K}^{\mathrm{a}}\right)\boldsymbol{u}^{\mathrm{s}} + \boldsymbol{f}^{\mathrm{c}} = 0. \tag{2.43}$$

In case of traveling wave modes (and thus a traveling wave basis for the ROM), the construction of real valued aerodynamic stiffness and damping matrices is not so straightforward. In [24], it is shown how aerodynamic damping and stiffness values determined from a flutter computation with a prescribed traveling wave motion can be converted to real valued aerodynamic damping and stiffness matrices for time integration. This way the aerodynamic forces for forward and backward traveling waves can be recovered in the time domain for harmonic blade vibrations, where the combination of two standing waves are necessary to replicate one traveling wave.

This approach is valid as long as there is no impact of the nonlinear contact forces on the mode shape(s), which makes this approach unfeasible for shrouded blades with contact interfaces. This could be resolved by approximating the structural motion by a very high number of modes, which however undoes the benefits of modal reduction.

If friction and aerodynamic forces are small compared to elastic and inertial forces of the blades, the vibration amplitude modulates on a slow time scale and asymptotic techniques can be applied to Eq. (2.43) to further reduce computational costs [43]. In [23] such an approach is extended for the simulation of multi-wave flutter (LTOs).

2.8.6 Coupled Time Integration Methods

In a bidirectionally coupled FSI simulation, Eq. (2.6) and Eq. (2.20) are solved at every time step under consideration of domain coupling. In general, coupled solvers can be classified into partitioned and monolithic approaches. A monolithic FSI solver is a single implicit solver which is able to setup the full Jacobi matrix of the coupled problem, i.e. the Jacobi matrix contains derivatives which associate structural and fluid degrees of freedom. In a partitioned approach, two (or more) domain specific solvers are used and only the block diagonal of the full system's Jacobi matrix is determined [72]. Thus, in case of a partitioned solver, a coupling algorithm is required in order to exchange data between the solvers and iteratively compute a converged solution.

For strongly coupled problems (where the structure is very flexible the mass ratio is high), a monolithic solver has the potential to be more efficient since no additional coupling algorithm is necessary. The disadvantage of monolithic solvers is, however, that a new solver must be developed from scratch - a re-use of existing (specialized) solvers can be difficult. In contrast, for a partitioned scheme, existing specialized solvers can be re-used with a manageable amount of effort.

A partitioned coupling scheme follows either a sequential or a parallel approach. In the sequential approach the two solvers are executed in a sequence as illustrated in **Figure 2.9** until the physical quantities at the time step $i+1$ are converged. In a parallel scheme, both solvers are executed simultaneously and the data is exchanged between the executions.

The convergence of a partitioned solver can be accelerated and/or stabilized by using different coupling algorithms. The most straight forward algorithms are fixed-point iterations, where the outcome of one solver $\boldsymbol{u}_i^{\mathrm{s}}$ or $\boldsymbol{u}_i^{\mathrm{a}}$ is fed into the other one. In case of numerical stability issues a relaxation parameter can be used, but in order to speed up convergence, more advance coupling algorithms can be employed, e.g. the Aitken method [37] or Quasi-Newton methods [13]. In a parallel coupling scheme, the two solvers are executed simultaneously, which has the benefit of a faster simulation time per iteration but usually requires more FSI iterations per physical time step. Thus, for a parallel scheme, Quasi-Newton methods which speed up the convergence, are necessary in order for the parallel approach to be competitive compared to sequential iterations [2]. The necessity of more advanced coupling schemes is determined by the type of FSI problem. For strongly coupled problems, e.g. a very flexible structure with a high mass ratio, fixed point iterations might converge very slowly or not at all and more sophisticated algorithms are required. For weakly coupled systems, e.g. a turbomachinery blade made of steel with a low mass ratio, only a very few fixed-point iterations are required for sufficient convergence.

In the following, a sequential approach with fixed point iterations is briefly described since it is widely used and also serves as a verification tool for the numerical methods developed in this work. A single coupling iteration consists of 4 stages (denoted 1 to 4 in **Figure 2.9**), as described in the following.

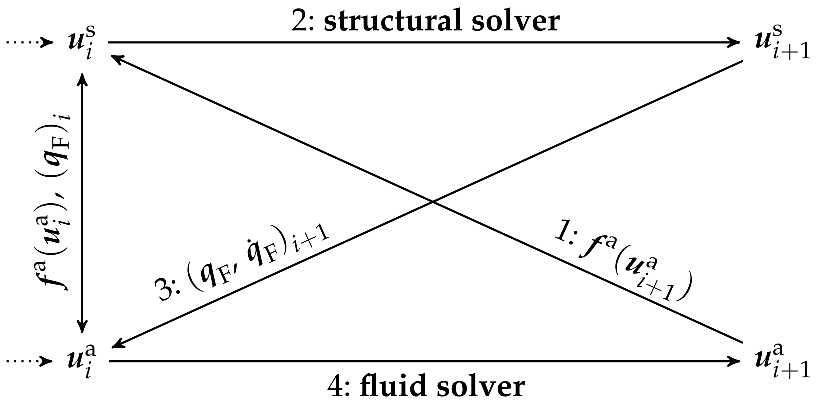

Figure 2.9: Sequential Coupling Scheme

In stage 1, the aerodynamic force $f^a(u_{i+1}^a)$ at the next time level t_{i+1} is calculated and interpolated onto the structure surface mesh. In the first coupling iteration, where no fluid solution exists yet, $f^a(u_{i+1}^a)$ can e.g. be linearly extrapolated from the last two time levels. In stage 2, the structural solver computes an updated estimate of the structural state variables u_{i+1}^s at t_{i+1}. In stage 3, the surface deformation of the fluid mesh q_F (and the velocity) at $t = t_{i+1}$ is determined by interpolation from the structure model and the fluid mesh is deformed accordingly. In stage 4, the flow solver computes an updated estimate of the conservative fluid variables u_{i+1}^a. Finally, the next coupling iteration starts with stage 1 or, if convergence is achieved, the next time level ($i \leftarrow i + 1$) is advanced.

Coupled time domain simulation methods are in principle able to resolve all nonlinear effects modeled in the respective domain and allow the coupled system to converge to any stable attractor (LCO, LTO or chaotic), however the computational costs are very high [E]. Another disadvantage of time marching methodologies is the treatment of fluid boundary conditions at the inlet and outlet of the computational fluid domain. Accurate

2-dimensional spectral Non-Reflecting Boundary Conditions (NRBCs) [55] require a fundamental frequency as input parameter which must be known a priori, see Section 2.6.2. In the case of flutter-induced LCOs however, this frequency is determined as part of the solution. This also prohibits the use of phase-lag methods for periodic boundaries because these also require a frequency as input parameter and thus a full blade row must be simulated in general as in [53]. State-of-the-art higher-order NRBCs [26] do not require a fundamental frequency and could in principle also be used for the simulation of LTOs but currently are less robust and take more time to converge compared to 2-dimensional spectral NRBCs. They as well require a full blade row simulation.

2.8.7 Forced Response Analysis

For a forced response analysis, the prevailing practice is to approximate the aerodynamic forces as a superposition of imposed forces (which would occur for rigid, rotating blades, e.g. due to wakes) and vibration-induced forces [7]. The latter are linearized and expressed by means of modal AICs. In the frequency domain, this yields

$$\hat{\boldsymbol{f}}^{\mathrm{a}}(\hat{\boldsymbol{u}}^{\mathrm{s}}) \approx \hat{\boldsymbol{f}}^{\mathrm{a}}_{\mathrm{wake}} + \boldsymbol{G}_a \hat{\boldsymbol{u}}^{\mathrm{s}}. \tag{2.44}$$

Usually only one AIC is determined with respect to a single mode, see e.g. [39, 47] , in a few exceptions a matrix is determined with respect to a small number of modes. In any case, the contact boundary conditions are linearized for the computation of the modes (usually assuming sticking contact). The described procedure neglects the amplitude dependence of the modal deflection shape (due to nonlinear contact interactions).

The principle of superimposed (and linearized) aerodynamic forces can simply be applied to a aeroelastic problems by adding the imposed forces to the equations. For example, a wake contribution could be added to the aerodynamic force $\hat{\boldsymbol{f}}^{\mathrm{a}}$ in Eqs. (2.35) and a subsequent analysis of the forced response by numerical path continuation yields the vibration levels as a function of the excitation frequency in the vicinity of the resonance peak.

The above described procedure also neglects the amplitude-dependence of the aerodynamic forces. In the present study it will be shown to have a considerable effect in the present study. Finally, it is a common practice to neglect the frequency dependence of the aerodynamic influence, which may have an effect of similar magnitude as the mode shape variation [C, D].

For coupled methods, a wake from an upstream blade row can be modeled as a boundary condition at the inlet of the fluid domain or, alternatively, the upstream blade row can be resolved by extending the computational domain, which however further increases the computation costs.

3 Purpose of this Work

Flutter-free designs of turbomachinery cascades limit the technological advancement and thus, flutter-tolerant designs of nonlinearly damped blades are currently explored in order to increase efficiency and reduce the weight of aircraft engines. Analogously, forced response vibrations remain a challenging task and a more accurate prediction compared to the current practice has the potential to further improve the mechanical design of components. Most methods like the energy method, influence coefficient methods or many nonlinear structural approaches are unidirectionally coupled, i.e. the aerodynamic forces are computed once and are linearized in the subsequent analysis. A change of mode shape and frequency is often only approximated or not modeled at all, except in case of fully coupled FSI simulations in the time domain, which are computationally expensive, suffer from some difficulties (e.g. NRBCs) and thus are very rarely seen. For the numerical evaluation of flutter-tolerant designs and forced response analysis however, bidirectional approaches would be beneficial for better predictions of current and future designs. In the following, shortcomings of current state-of-the-art methods regarding this topic are identified:

- For the conventional energy method, where frequency and shape of the vibration are assumed as constant, the amplitude can be determined from the requirement that supplied and dissipated work per cycle cancel each other ($W_\mathrm{s} + W_\mathrm{a} = 0$). This strategy was followed e.g. in [43, 59], and it is most certainly the prevailing industry practice today. It is justified if the aerodynamic and nonlinear contact forces have negligible effect on the deflection shape and frequency of the LCO. However, the nonlinear contact boundary conditions can easily account for more than 10% frequency shift and significantly alter the deflection shape [25], as compared to the linearized case. Given that the reduced frequency and the deflection shape are the driving determinants for flutter, this strategy has a strictly limited range of validity. Indeed, the sign of the aerodynamic work can be affected by the boundary conditions at the contact interfaces. For instance, Leyes et al. [41] associate a blade failure in an aircraft engine to a flutter instability caused by the altered boundary conditions at the tip shrouds due to fretting wear. Similarly, Wu et al. [71] demonstrate a test case that was stable for sticking and unstable for frictionless sliding tip shroud interfaces.
- The method of influence coefficients is, in principle, able to model the impact of vari-

able mode shape and frequency on the aerodynamic forces. However, if a reduced structural ROM contains too many generalized coordinates, then the calculation of the fully populated AIC matrix becomes very costly or even impracticable. Furthermore the aerodynamic forces are assumed to behave linear and in the context of forced response the superposition of imposed and vibration induced aerodynamic forces is assumed which limits the validity.

- Common methodologies for a more sophisticated structural analysis include the impact of nonlinear forces (e.g. dry friction in contact interfaces) on the mode shape and frequency, however the aerodynamic forces acting on the blade have been modeled in a very simplified way in the past. Especially, the influence of the mode shape and frequency on the aerodynamic forces was neglected or approximated with a limited number of aerodynamic influence coefficients.
- To account for nonlinear phenomena and their interactions of vibrating blades in turbomachinery, coupled solvers with time accurate integration schemes could be used. Here the disadvantage lies in the very high computational costs (primarily due to the very high number of degrees of freedom of the fluid model). Furthermore sophisticated and robust boundary conditions for the inlet and outlet of the computational fluid domain are necessary in order to minimize numerical reflections. This comes however with difficulties for time accurate simulations, one of them being the a priori unknown vibration frequency in case of flutter. Another problem of time integration schemes lies in the potentially high numerical stiffness of detailed structure models with a relatively high number of degrees of freedom. This can lead to a very small allowable time step size and thus, together with the computational fluid dynamics, to very high computational costs. Advanced time marching schemes in combination with appropriate contact modeling can cure this issue, but the problems mentioned above regarding the fluid boundary conditions would still need to be addressed.

These issues limit the application of existing methods for the analysis of flutter induced LCOs and forced response of turbomachinery blades. Moreover nonlinear effects and their interactions between the structure and the fluid are an active field of research and an improved physical understanding of coupled mechanical systems would be a valuable contribution to the future design process of turbomachinery components.

In order to provide a solution to the above issues, this work suggests an extension of the energy method for flutter vibrations and an efficient coupled frequency-domain solver is developed. The coupled solver is applied to flutter induced LCOs and, in a slightly modified variant, embedded in forced response analysis. Since the focus lies on periodic vibrations the harmonic balance method lends itself as a core method.

The central topics of this work are:

- *How can harmonic balance based methods be extended in order to improve the prediction quality and computational efficiency for flutter induced LCOs and forced response vibra-*

tions? Here, *prediction quality* refers to the consideration of the amplitude dependent mode shape and vibration frequency induced by nonlinear contact mechanics. As in case of coupled time integration methods, the interaction between the mode shape/frequency and the aerodynamic forces should be modeled, but with drastically reduced computational costs.

- *Evaluate the potential impact of the above mentioned nonlinear effects on the flutter characteristics and forced response.*

3.1 Development of Coupled Nonlinear Flutter Analysis Methods for Turbomachinery Blades

3.1.1 Extension of the Linear Energy Method

In Section 4.1, the linear energy method is extended by using the nonlinear modal analysis concept. The resulting unidirectional coupled method should be able to analyze the blade vibrations for a range of amplitudes. Nonlinear structural effects as well as the unsteady nonlinear fluid equations (in particular local nonlinear and unsteady flow features) are considered in this approach. Also a bidirectional coupled variant of the extended energy method is introduced which serves as an additional verification tool.

3.1.2 Coupled Frequency Domain Solver for the Analysis of LCOs and Forced Response

A bidirectional coupled frequency domain solver is developed and presented in Section 4.2, which accurately computes the flutter induced periodic motions of the fluid and the structure. All nonlinear effects which can be modeled by the underlying structure and fluid solvers and their interactions are considered. The computational efficiency should be reduced by at least an order of magnitude compared to time domain simulation methods. Analogous to the coupled flutter analysis, also a bidirectional analysis method is developed for the simulation of forced response blade vibrations.

3.2 Investigation of Nonlinear Blade Vibrations

The novel methods are applied to shrouded low pressure turbine test cases with contact surfaces in the shroud. The aim is to investigate the physical interactions between the solid and the fluid. The results from the numerical test cases should indicate which physical aspects of the coupled system are of significance for flutter induced LCOs.

More specifically, the impact of the change of mode shape and frequency on the aerodynamic forces is investigated. Furthermore, the interaction between higher harmonics of the structure and the fluid are analyzed, providing further insights into physical aspects of the coupled system. Finally, also numerical aspects will be investigated, e.g. harmonic convergence.

For forced response analysis the influence of the change of mode shape due to nonlinear contact on the resonance peak is demonstrated. Furthermore a test case is investigated, where the superposition assumption for the aerodynamic forces is validated for the case of a considerable shock motion on the blade surface.

3.3 Advantages and Limitations of the Proposed Methods

Time integration schemes have several limitations which makes their application to self-excited LCOs of turbomachinery blades difficult. On the other hand the presented frequency methods have other limitations. The advantages and disadvantages of both approaches are evaluated and discussed.

4 Nonlinear Frequency Domain Methods for Flutter and Forced Response

The content of this chapter is primarily taken from [C, D]. As outlined in Chapter 3, there is a lack of efficient numerical methods suitable for the calculation of flutter induced LCOs.

There is thus a need for simulation methods that predict the nonlinear Fluid-Structure Interaction. One of the purposes of this work is to develop efficient frequency-domain methods for computing flutter-induced LCOs of bladed disks, which are capable of accounting for both structural and aerodynamic nonlinear effects. First, the conventional energy method is refined to take into account structural nonlinearities and their effect on the aerodynamic damping (Section 4.1). Then, the fully-coupled solver is presented in Section 4.2.

4.1 Energy Methods

The basic idea behind energy methods is, for a given frequency ω, deflection shape $\boldsymbol{\psi}$ and amplitude, to evaluate the work per cycle W going into or out of the vibrating structure. When the analysis is based on small amplitudes, the stability around the static equilibrium is evaluated, which is the most common application of the energy method. This approach is now extended to be valid for a (finite) range of amplitudes under consideration of nonlinear effects. More specifically, the (aerodynamic or structural) work per cycle will be evaluated for a range of amplitudes and subsequently may be compared to each other. An exemplary result of such an analysis is illustrated in **Figure 4.1(b)**. The right plot depicts the structural dissipation W^{s} and the aerodynamic work $-W^{\mathrm{a}}$ as function of the amplitude $\hat{u}$. At the intersection points, where $W^{\mathrm{a}} + W^{\mathrm{s}} = 0$, the corresponding amplitudes mark either stable or unstable limit cycles. By analyzing the dependence of W^{a} and W^{s} on the amplitude $\hat{u}$, one can also infer the stability of a given limit cycle: A positive slope at the zero crossing of $W^{\mathrm{a}} + W^{\mathrm{s}}$ means that for increased amplitude, the dissipated work exceeds the supplied one. Thus, the system returns to the limit cycle in the presence of a small perturbation; the limit cycle is stable. If, in contrast, the slope is negative, an arbitrarily small perturbation would drive the amplitude away from this point; the limit cycle is unstable. Here, only the stability from an energy point of view is considered, which may not be equivalent to asymptotic stability.

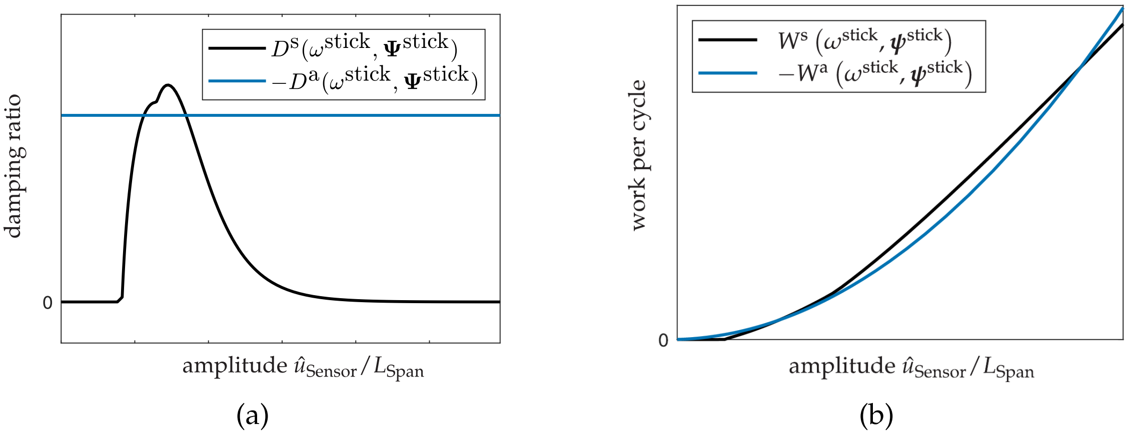

Figure 4.1: Example of a stable LCO and a stability limit: (a) Damping ratio vs. amplitude; (b) Work vs. amplitude [D].

In the example shown in **Figure 4.1**, two limit cycles can be identified. This is a typical situation under aerodynamic self-excitation and dry frictional dissipation. Assuming that the aerodynamic forces depend linearly on the structural displacements, and the mode shape and frequency are fixed, the aerodynamic damping ratio

$$D = \frac{W}{4\pi E_{\mathrm{kin,max}}} \tag{4.1}$$

is constant and W^{a} grows quadratically with the amplitude (since the maximum kinetic energy $E_{\mathrm{kin,max}}$ is a function of the amplitude squared). For small vibration amplitudes, the contact is sticking, and consequently W^{s} is zero. For sufficiently large amplitudes, sliding friction occurs. For constant normal load, the area enclosed in the force-displacement hysteresis cycle, which corresponds to W^{s}, grows linearly beyond this point. The left intersection corresponds to a stable, the right to an unstable limit cycle. As there is no further limit cycle at higher amplitudes (for the given model), the unstable limit cycle can also be viewed as a *stability limit*. In **Figure 4.1(a)** the same situation is shown but in terms of the damping ratio plotted against the logarithm of the amplitude, makes it a bit easier to identify the intersections.
The available energy methods differ by the simplifying assumptions made for the determination of ω and $\boldsymbol{\psi}$.

4.1.1 Refined Energy Method

In the following, a refinement of the conventional energy method is proposed, which takes into account the nonlinear amplitude-dependence of mode shape, $\boldsymbol{\psi}^{\mathrm{nl}}(\hat{u})$, and natural frequency, $\omega^{\mathrm{nl}}(\hat{u})$. To determine these, in a first step a nonlinear modal analysis (NMA) is carried out as described in Section 2.8.3. Therefore, the NMA equation of the structural model in vacuum

$$\boldsymbol{S}_k(\omega^{\mathrm{nl}})\hat{\boldsymbol{u}}^{\mathrm{s}}_k + \hat{\boldsymbol{f}}^{\mathrm{c}}_k(\hat{\boldsymbol{u}}^{\mathrm{s}}) = 2D^{\mathrm{s}}\omega^{\mathrm{nl}}(\mathrm{i}k\omega^{\mathrm{nl}})\boldsymbol{M}^{\mathrm{cb}}_k\hat{\boldsymbol{u}}^{\mathrm{s}}_k \;\; k = 0, 1, \ldots, H \tag{4.2}$$

is solved with numerical path continuation for a technically relevant interval of the modal amplitude $\hat{u}$. Since the aerodynamic forces are not considered at this point, it is a one-way coupled approach. As a result of the NMA, one obtains the natural frequency $\omega^{\mathrm{nl}}(\hat{u})$, modal damping ratio $D^{\mathrm{s}}(\hat{u})$ and Fourier coefficients of the modal deflection shape $\boldsymbol{\psi}_k^{\mathrm{nl}}$, where harmonic (nodal) displacements are retrieved according to $\hat{\boldsymbol{u}}_k^{\mathrm{s}} = \boldsymbol{\psi}_k^{\mathrm{nl}}(\hat{u})\hat{u}$. Herein, the mode shape of the fundamental harmonic is normalized with respect to the mass matrix such that $\boldsymbol{\psi}_1^{\mathrm{nl}\,\mathrm{H}}\boldsymbol{M}\boldsymbol{\psi}_1^{\mathrm{nl}} = 1$.

In a second step, the aerodynamic work per period for the amplitude-dependent mode shape $\boldsymbol{\psi}^{\mathrm{nl}}(\hat{u})$ and natural frequency $\omega^{\mathrm{nl}}(\hat{u})$ is evaluated. To account for the change of the mode shape, the aerodynamic force $\hat{\boldsymbol{f}}^{\mathrm{a}}$ is approximated using the aerodynamic influence coefficient matrix $\boldsymbol{G}$ with respect to the component modes,

$$\hat{\boldsymbol{f}}^{\mathrm{a}}(\hat{u}) = \boldsymbol{G}\left(\omega^{\mathrm{nl}}(\hat{u})\right)\hat{\boldsymbol{u}}^{\mathrm{s}} = \boldsymbol{G}\left(\omega^{\mathrm{nl}}(\hat{u})\right)\boldsymbol{\psi}^{\mathrm{nl}}(\hat{u})\,\hat{u}\,. \tag{4.3}$$

$\boldsymbol{G}$ is set up column-wise, $\boldsymbol{G} = [\boldsymbol{G}_1 \dots \boldsymbol{G}_N]$, where $\boldsymbol{G}_i = \boldsymbol{T}^{\mathrm{cb}\,\mathrm{H}}\hat{\boldsymbol{f}}_1^{\mathrm{a,fem}}\left(\boldsymbol{T}^{\mathrm{cb}}\boldsymbol{e}_i\right)$ for $i = 1, \dots, N$. Thus, the fundamental Fourier coefficient of the aerodynamic forces must be determined, obtained under a harmonic structural displacement in the form of every component mode (index i). In other words, $\boldsymbol{G}(\omega)$ is computed in a preprocessing step with respect to all component modes of the structural reduced order model. To account for the change of the natural frequency, $\boldsymbol{G}$ is linearly interpolated as

$$\boldsymbol{G}(\omega) = \boldsymbol{G}(\omega^{\mathrm{stick}}) + \left(\boldsymbol{G}\left(\omega^{\mathrm{slip}}\right) - \boldsymbol{G}\left(\omega^{\mathrm{stick}}\right)\right)\frac{\omega^{\mathrm{stick}} - \omega}{\omega^{\mathrm{stick}} - \omega^{\mathrm{slip}}}. \tag{4.4}$$

Herein, ω^{slip} and ω^{stick} are the natural frequencies under the frictionless sliding and sticking linear limit cases, and $\boldsymbol{G}^{\mathrm{slip}}$, $\boldsymbol{G}^{\mathrm{stick}}$ are obtained by imposing the structural displacement with the corresponding frequency. In case no linear limit cases exist for a specific model, sensible frequencies should be chosen for the evaluation. It should be noticed, that the linearization of $\hat{\boldsymbol{f}}^{\mathrm{a}}$ via $G(\omega)$ is not limited to a single harmonic k - even the interaction among several harmonics can be reflected. In this case, $G(\omega)$ is not only block-diagonal but fully populated. The computational costs however will also increase since for each additional harmonic also additional fluid simulations are necessary.

Analogously to Eq. (2.29), the aerodynamic work per cycle is then given by

$$W_{\mathrm{a}}(\hat{u}) = \Re\left\{-\mathrm{i}\pi\left(\boldsymbol{\psi}^{\mathrm{nl}}(\hat{u})\right)^{\mathrm{H}}\boldsymbol{G}\left(\omega^{\mathrm{nl}}(\hat{u})\right)\boldsymbol{\psi}^{\mathrm{nl}}(\hat{u})\right\}\hat{u}^2 \tag{4.5}$$

from which the aerodynamic damping ratio D^{a} can be retrieved. Finally, $-D^{\mathrm{a}}(\hat{u})$ and $D^{\mathrm{s}}(\hat{u})$ can be plotted as functions of $\hat{u}$ similar as in **Figure 4.1(a)** and LCOs or stability limits are identified as intersection points between the two curves.

As an alternative to the influence coefficient matrix in Eq. (4.3), the aerodynamic forces can be computed by imposing the deflection shape $\boldsymbol{\psi}^{\mathrm{nl}}(\hat{u})$ and frequency $\omega^{\mathrm{nl}}(\hat{u})$ directly, for specific values of the amplitude $\hat{u}$. In other words, for some selected sampling points of $\hat{u}$, a fluid simulation is conducted for the evaluation of $\hat{\boldsymbol{f}}^{\mathrm{a}}(\hat{u})$.

In preliminary investigations, it was found that the results of both alternatives are in very good agreement in the relevant amplitude and frequency range. On the one hand, the analysis of $\boldsymbol{G}(\omega)$ can provide deeper insight into the aerodynamic interaction of certain modes of vibration while on the other hand, the direct evaluation of $\hat{\boldsymbol{f}}_1^{\mathrm{a}}$ using $\boldsymbol{\psi}^{\mathrm{nl}}(\hat{u})$ and $\omega^{\mathrm{nl}}(\hat{u})$ can indeed be more computationally feasible and is not a priori limited to linear amplitude- and frequency-dependence of the aerodynamic forces.

4.1.2 Refined Energy Method in Air

The refined energy method in air is a generalized form of the refined energy method above. Here, the aerodynamic forces are modeled in terms of influence coefficients according to Eq. (4.3) and considered during the NMA:

$$\boldsymbol{S}_k(\omega^{\mathrm{nl}})\hat{\boldsymbol{u}}_k^{\mathrm{s}} + \hat{\boldsymbol{f}}_k^{\mathrm{c}}(\hat{\boldsymbol{u}}^{\mathrm{s}}) - \boldsymbol{G}\left(\omega^{\mathrm{nl}}\left(\hat{u}\right)\right)\hat{\boldsymbol{u}}^{\mathrm{s}}\Big|_k = 2D^{\mathrm{s}}\omega^{\mathrm{nl}}(\mathrm{i}\,k\omega^{\mathrm{nl}})\boldsymbol{M}_k^{\mathrm{cb}}\hat{\boldsymbol{u}}_k^{\mathrm{s}}\ :\ k = 0,1,\ldots,H \quad (4.6)$$

Since the aerodynamic forces are expressed in closed form as function of frequency and structural deformation, the only unknowns in Eq. (4.6) are $\hat{\boldsymbol{u}}^{\mathrm{s}}$, ω and D^{s}, and the approach can be considered a two-way coupled method (however, linear aerodynamic forces are still assumed).

4.2 Coupled FD-FSI Solver

The purpose of the newly developed solver is to be able to calculate single periodic solutions of the coupled fluid-structure system with a very high accuracy. Contrary to time accurate FSI methods (as described in Section 2.8.6), the newly developed Frequency Domain Fluid-Structure Interaction (FD-FSI) solver seeks a solution to the Harmonic Balance equations Eq. (2.28) and Eq. (2.26). The set of unknowns consists of $(\hat{\boldsymbol{u}}^{\mathrm{a}}, \hat{\boldsymbol{u}}^{\mathrm{s}}, \omega)$ and must satisfy both equations simultaneously (plus the boundary conditions in either domain). The governing equations of the coupled problem are compactly denoted as

$$\begin{aligned} \boldsymbol{R}^{\mathrm{s}}\left(\boldsymbol{X}^{\mathrm{s}}, \hat{\boldsymbol{f}}^{\mathrm{a}}\left(\hat{\boldsymbol{u}}^{\mathrm{a}}\right)\right) &= \mathbf{0}, & (4.7)\\ \boldsymbol{R}^{\mathrm{a}}\left(\boldsymbol{X}^{\mathrm{a}}, \omega, \hat{\boldsymbol{\chi}}\left(\hat{\boldsymbol{u}}^{\mathrm{s}}\right)\right) &= \mathbf{0}. & (4.8) \end{aligned}$$

As in Section 2.8.3, the problem has been cast into real arithmetic; i.e., $\boldsymbol{R}^{\mathrm{s}}$ and $\boldsymbol{R}^{\mathrm{a}}$ are real-valued. Accordingly, the vectors of unknowns $\boldsymbol{X}^{\mathrm{s}} = [\Re\{\hat{\boldsymbol{u}}^{\mathrm{s}}\}, \Im\{\hat{\boldsymbol{u}}^{\mathrm{s}}\}, \omega]^{\mathrm{T}}$ and $\boldsymbol{X}^{\mathrm{a}} = [\Re\{\hat{\boldsymbol{u}}^{\mathrm{a}}\}, \Im\{\hat{\boldsymbol{u}}^{\mathrm{a}}\}]^{\mathrm{T}}$ correspond to the real coefficients. Again, the imaginary part of the zeroth harmonic is implicitly discarded which is not reflected in the notation for brevity. The residual vector function $\boldsymbol{R}^{\mathrm{a}}$ corresponds to the Harmonic Balance equations for the fluid Eq. (2.28) and the residual vector function $\boldsymbol{R}^{\mathrm{s}}$ is defined in the same way as in Eq. (2.37):

$$\boldsymbol{R}^{\mathrm{s}}\left(\boldsymbol{X}^{\mathrm{s}}, \hat{\boldsymbol{f}}^{\mathrm{a}}\left(\hat{\boldsymbol{u}}^{\mathrm{a}}\right)\right)=\begin{bmatrix}\Re\left\{\boldsymbol{r}^{\mathrm{s}}\left(\boldsymbol{X}^{\mathrm{s}}, \hat{\boldsymbol{f}}^{\mathrm{a}}\left(\hat{\boldsymbol{u}}^{\mathrm{a}}\right)\right)\right\} \\ \Im\left\{\boldsymbol{r}^{\mathrm{s}}\left(\boldsymbol{X}^{\mathrm{s}}, \hat{\boldsymbol{f}}^{\mathrm{a}}\left(\hat{\boldsymbol{u}}^{\mathrm{a}}\right)\right)\right\} \\ r^{\mathrm{con}}\left(\boldsymbol{X}^{\mathrm{s}}\right)\end{bmatrix}=\mathbf{0}, \tag{4.9}$$

where $\boldsymbol{r}^{\mathrm{s}}$ corresponds to the Harmonic Balance equations for the structure and r^{con} is an additional constraint residual which is defined later depending on the problem the FD-FSI solver is applied to. In principle, r^{con} could be a function of both, the fluid and structure variables, $r^{\mathrm{con}}\left(\boldsymbol{X}^{\mathrm{s}}, \boldsymbol{X}^{\mathrm{a}}\right)$, but for the applications in this work, the dependency on structural variables only, $r^{\mathrm{con}}\left(\boldsymbol{X}^{\mathrm{s}}\right)$, is sufficient.

A monolithic solver suitable for the simulation of turbomachinery blade vibrations including contact friction would require a very high implementation effort and thus a partitioned approach is followed. An important benefit of this strategy is that it is not intrusive, in the sense that existing codes for either domain can be used, and individual single-domain solvers can be employed that are optimized for the individual subproblems. In the following, the serial coupling loop is explained in order to give an overview of the FD-FSI solver and in the remainder of the section, details of the different steps are highlighted.

The algorithm of the partitioned FD-FSI solver is illustrated in **Figure 4.2**. Here, the structural and the fluid sub-problems are solved in a (serial) iteration loop. An initial guess $\boldsymbol{X}^{\mathrm{s}}_{(0)}$ is required, as defined later. The outer iteration loop starts by updating the flow mesh deformation $\hat{\chi}_{(m)}$ in accordance with the periodic structural displacement. Next, the harmonic balance residual of the fluid domain is minimized by iteratively improving the flow variables $\boldsymbol{X}^{\mathrm{a}}$. In this step, the frequency ω and the Fourier coefficients of the structural deformation $\hat{\boldsymbol{u}}^{\mathrm{s}}$ are held constant. Once the residual norm falls below a specified tolerance, the aerodynamic force is determined. Subsequently, the harmonic balance residual of the structure solver is minimized by iteratively improving both the frequency ω and the structural variables $\hat{\boldsymbol{u}}^{\mathrm{s}}$. In this step, the aerodynamic force $\hat{\boldsymbol{f}}^{\mathrm{a}}$ is considered as input. As the residuals in both domains are always reduced below the specified tolerance, the current estimate is considered as solution of the coupled problem if it does not change between two iterations (according to a given tolerance ε). If the structure and fluid solvers are denoted as two operators $\boldsymbol{X}^{\mathrm{s}}_{(m+1)}=\mathcal{S}\left(\hat{\boldsymbol{f}}^{\mathrm{a}}\left(\hat{\boldsymbol{u}}^{\mathrm{a}}\right)_{(m)}\right)$ and $\hat{\boldsymbol{f}}^{\mathrm{a}}\left(\hat{\boldsymbol{u}}^{\mathrm{a}}\right)_{(m)}=\mathcal{F}\left(\boldsymbol{X}^{s}_{(m)}\right)$, then one iteration of the coupling loop corresponds to the chained application of these two operators

$$\boldsymbol{X}^{\mathrm{s}}_{(m+1)}=\mathcal{S}\circ\mathcal{F}\left(\boldsymbol{X}^{\mathrm{s}}_{(m)}\right), \tag{4.10}$$

which corresponds to a fixed-point algorithm.

The structural solver uses a Newton-Raphson scheme as implemented in the open source

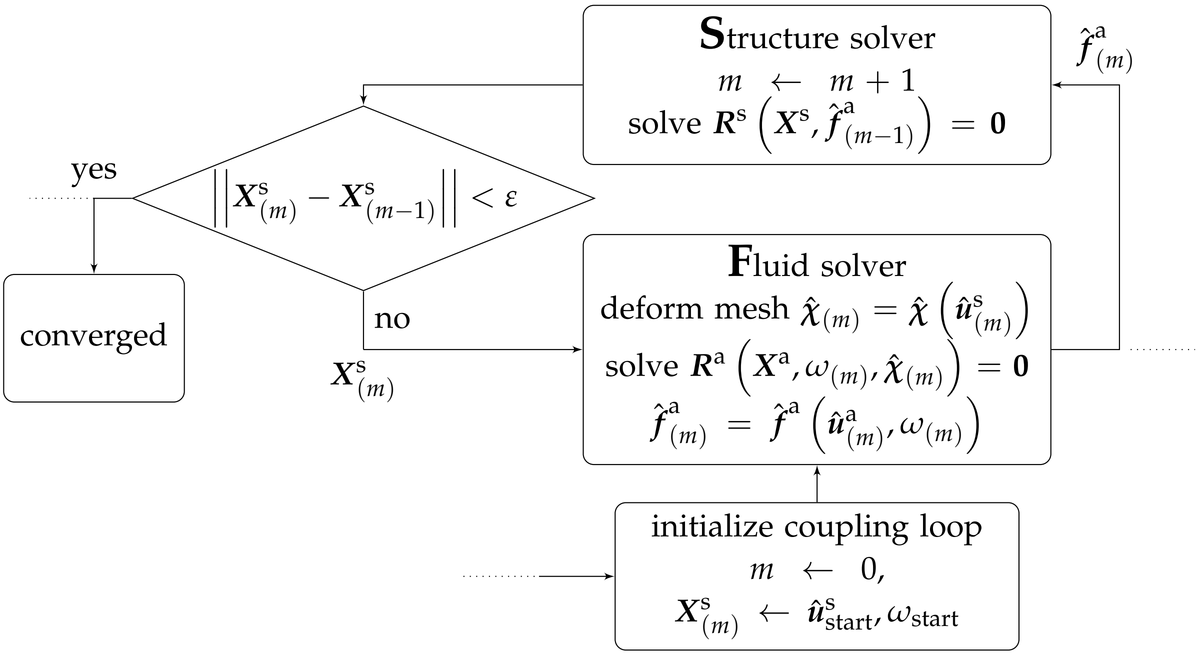

Figure 4.2: Algorithm scheme of the FD-FSI solver.

Harmonic Balance tool NLvib [35]. It iterates on the solution $\boldsymbol{X}^{\mathrm{s}}$ according to

$$\boldsymbol{X}^{\mathrm{s}}_{(m+1,i+1)} = \boldsymbol{X}^{\mathrm{s}}_{(m+1,i)} - \left(\frac{\partial \boldsymbol{R}^{\mathrm{s}}}{\partial \boldsymbol{X}^{\mathrm{s}}}\right)^{-1}\Bigg|_{\boldsymbol{X}^{\mathrm{s}}_{(m+1,i)}} \boldsymbol{R}^{\mathrm{s}}\left(\boldsymbol{X}^{\mathrm{s}}_{(m+1,i)}\right) \tag{4.11}$$

with i denoting the Newton-Raphson iterations.

The fluid model is implemented in the tool TRACE [21, 1], where the Harmonic Balance equations are solved with a pseudo time stepping scheme, since in general the fluid model contains a very large number of unknowns. For the pseudo time stepping scheme, an artificial time τ is introduced and an additional derivative term is added to Eq. (4.8) yielding

$$\frac{\partial \boldsymbol{X}^{\mathrm{a}}}{\partial \tau} + \boldsymbol{R}^{\mathrm{a}}(\boldsymbol{X}^{\mathrm{a}}, \omega, \hat{\boldsymbol{u}}^{\mathrm{s}}) = \boldsymbol{0}. \tag{4.12}$$

Eq. (4.12) is solved with an implicit time integration scheme until steady state in terms of τ is reached which implies that the pseudo time derivative term equals zero and hence Eq. (4.8) is solved. More details on this solver can be found in [21, 1].

In contrast to energy methods, it is straight-forward to account for all nonlinear effects that can be modeled with the underlying fluid and structure solvers. Hence, the fully-coupled solver is more versatile and has the potential for a much higher prediction accuracy. It should be emphasized that the vibrational frequency is not a priori known and considered as part of the solution.

An advantage of the FD-FSI solver with respect to the computational efficiency is that the data exchanged between the respective single-domain solvers does not require significant amount of memory. Only Fourier coefficients of generalized coordinates and forces plus the oscillation frequency are exchanged, so only $(2H+1)N+1$ with $H = \min(H^{\mathrm{s}}, H^{\mathrm{a}})$

real numbers must be exchanged, where N denotes the number of generalized coordinates of the structural model. The resulting computational effort for the data exchange between the solvers is negligible compared to the total computational burden. This contrasts the common multi-physics simulation tools, which exchange displacements and forces at all surface nodes and possibly many time levels. In the following subsections, a few crucial aspects for the computational efficiency and robustness of the FD-FSI solver are addressed.

4.2.1 Stability of the Obtained Solutions

For the partitioned FD-FSI solver, a Newton method for the structure solver is combined with a pseudo time stepping scheme for the fluid solver. The Newton solver allows the FD-FSI solver to converge not only to stable LCOs but also to asymptotically unstable solutions as will be shown later. This is in contrast to a monolithic FSI solver approach, where pseudo time stepping would most likely be employed to both domains. In this case, unstable LCOs could not be obtained, which is a limitation of the pseudo time approach.

4.3 Application of the FD-FSI Solver to Flutter Induced LCOs

4.3.1 Treatment of Unknown Frequency and Exclusion of Trivial Solution

As the system is autonomous in case of a flutter induced LCO, a given periodic solution can be time-shifted arbitrarily and will still remain a solution. In other words, the phase of the solution is arbitrary in the autonomous case. To achieve local uniqueness, it is common practice to impose a phase constraint. Taking into account that the oscillation frequency is an additional unknown in the autonomous case, this phase constraint is also necessary to make the number of equations equal to the number of unknowns. Typically, the real or imaginary part of the fundamental Fourier coefficient of a specific coordinate is commonly set to zero. While this constrains the phase, it does not exclude the trivial solution (static equilibrium, $\hat{\boldsymbol{u}}^{\mathrm{s}} = \boldsymbol{0}$). Without appropriate countermeasures, therefore, the structural solver might run into the static equilibrium. To overcome this, a different phase constraint is proposed: The real part of the fundamental Fourier coefficient of a selected generalized coordinate $\boldsymbol{e}_i^{\mathrm{T}} \boldsymbol{X}^{\mathrm{s}}$ is set to a suitable *nonzero* value v (**Figure 4.3**), where $\boldsymbol{e}_i$ denotes the i-th unit vector. It should be noticed that the index i refers to (but is not equal to) the index j of $\hat{u}_j^{\mathrm{s}}$ in **Figure 4.3** since the latter corresponds to the system formulated in complex Fourier coefficients. The proposed constraint is imposed by setting the constraint

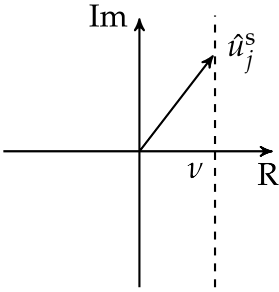

Figure 4.3: Non-trivial phase constraint to avoid trivial solution [D].

residual r^{con} included in Eq. (4.9) to

$$r^{\mathrm{con}}\left(\boldsymbol{X}^{\mathrm{s}}\right) = \boldsymbol{e}_i^{\mathrm{T}} \boldsymbol{X}^{\mathrm{s}} - \nu. \tag{4.13}$$

Since the FD-FSI solver can still adjust the imaginary part, this does not constrain the physical solution (except if the prescribed real part exceeds the magnitude, which can be easily checked upon solving). The generalized coordinate associated with the dominant fixed-interface mode is selected for the constraint. This is expected to provide great numerical performance, as this coordinate characterizes the motion of the structure very well and is not likely to suddenly flip or significantly change its phase relative to the rest of the coordinates during the solution process. It is important to emphasize that the described procedure has no impact on the physical solution but is actually necessary to obtain a well posed problem.

The frequency is determined only during the structural solution process in order to achieve compatibility of the solution between the fluid and structure problem. This requires that valid solutions of the fluid sub-problem can be retrieved for each iteration, where during its execution the frequency is held constant. This implies, that for a (hypothetical) trivial solution $\hat{\boldsymbol{u}}^{\mathrm{s}} = \boldsymbol{0}$, the fluid solution must be steady. Consequently, fluid instabilities leading to unsteadiness where the frequency is governed mainly by the fluid, also known as Non-Synchronous Vibrations (NSV), cannot be simulated by the proposed FD-FSI solver, and hence, the proposed treatment of the unknown frequency is only suited for purely flutter induced vibrations. An exception could be the situation of locked-in NSV, where the frequency of the fluid perturbations lock in to the structural eigenfrequency of the blades. The more complicated situation of NSV (as it can occur in case of vortex shedding or acoustic resonance), however, is beyond the scope of this work.

4.3.2 Initialization

A good initialization of the FD-FSI solver for flutter induced LCOs is favorable. Therefore, the results from the refined energy method can be used

$$\hat{\boldsymbol{u}}^{\mathrm{s}}_{(0)} = \boldsymbol{\psi}^{\mathrm{nl}}(\hat{u}^{\mathrm{lco}})\, \hat{u}^{\mathrm{lco}}, \qquad \omega_{(0)} = \omega^{\mathrm{nl}}(\hat{u}^{\mathrm{lco}})\,, \tag{4.14}$$

where $\hat{u}^{\mathrm{lco}}$ is the modal amplitude of the limit cycle predicted by the refined energy method. The phase of $\hat{\boldsymbol{u}}^{\mathrm{s}}_{(0)}$ is modified in order to meet the phase constraint illustrated in **Figure 4.3**. An alternative to a result from the refined energy method is a simple guess. When a limit cycle is expected, a result from an appropriate interval of an NMA analysis usually suffices for the coupled solver to converge to the LCO (if it exists). This way, no knowledge of the aerodynamic work and thus no prior CFD simulations are necessary.

4.3.3 Linear Surrogate Model of the Flow Force

The fixed-point iteration algorithm outlined in **Figure 4.2** will converge only very slowly due to a very slow step wise update of the aerodynamic force, which motivates further optimization. Within the structural subproblem, it is proposed to model the aerodynamic force $\hat{\boldsymbol{f}}^{\mathrm{a}}$ as linear with respect to the vibration amplitude, but always strictly consistent with the force $\hat{\boldsymbol{f}}^{\mathrm{a}}_{(m)}$ output by the previous run of the fluid solver. This ensures that the converged solution is independent of the assumed linearization. However, the linearization greatly speeds up the overall convergence of the coupled solver as the assumed linearity is at least locally a reasonable approximation. This proposition turns the coupling algorithm of the FD-FSI solver into a quasi Newton-like scheme [42], where instead of the approximate linearization of the complete fixed-point equation, the approximate linearization of one solver is inserted into the other one. Two variants of the described linearization are considered in the following.

4.3.3.1 Frequency-Dependent Influence Coefficient Matrix

If the fully-populated influence coefficient matrix is available the aerodynamic force $\hat{\boldsymbol{f}}^{\mathrm{a}}$ in Eq. (2.26) can be split as

$$\hat{\boldsymbol{f}}^{\mathrm{a}}_1(\hat{\boldsymbol{u}}^{\mathrm{s}},\omega) = \hat{\boldsymbol{f}}^{\mathrm{a}}_{1,(m)} + \boldsymbol{G}\left(\omega\right)\hat{\boldsymbol{u}}^{\mathrm{s}}_1 - \boldsymbol{G}\left(\omega_{(m-1)}\right)\hat{\boldsymbol{u}}^{\mathrm{s}}_{1,(m-1)} \quad \hat{\boldsymbol{f}}^{\mathrm{a}}_k = \hat{\boldsymbol{f}}^{\mathrm{a}}_{k,(m)}\ \forall k \neq 1\,. \tag{4.15}$$

Note that $\hat{\boldsymbol{f}}^{\mathrm{a}}_{(m)}$ is obtained by imposing $\hat{\boldsymbol{u}}^{\mathrm{s}}_{(m-1)}$ and $\omega_{(m-1)}$ in the previous run of the fluid solver (**Figure 4.2**). $\boldsymbol{G}(\omega)\hat{\boldsymbol{u}}^{\mathrm{s}}$ can be viewed as the part of the aerodynamic forces explainable by the influence coefficient matrix. Here, it is assumed that $\boldsymbol{G}$ was evaluated only for the first harmonic, but this approach could be extended to other multiple harmonics.

4.3.3.2 Frequency-Independent Influence Coefficient Matrix

A simplified variant of the previous approach is to neglect the frequency dependence of $\boldsymbol{G}$. This seems justified if the change in frequency due to nonlinear effects is small. The simplification halves the computational effort in the pre-processing, since $\boldsymbol{G}$ does not have to be computed at two frequencies in order to obtain an interpolation with respect to ω.

4.3.3.3 Dominating-Mode Linearization

The disadvantage of the above methods is that the computation of a fully-populated influence coefficient matrix is relatively expensive. Another possibility is to linearize the aerodynamic force, in an ad-hoc way, as

$$\hat{\boldsymbol{f}}^{\mathrm{a}} = \hat{\boldsymbol{f}}^{\mathrm{a}}_{(m)} \frac{\boldsymbol{e}_i^{\mathrm{T}} \boldsymbol{u}_1^{\mathrm{s}}}{\boldsymbol{e}_i^{\mathrm{T}} \boldsymbol{u}_{1,(m-1)}^{\mathrm{s}}}. \tag{4.16}$$

Recall that $\boldsymbol{e}_i$ is the unit vector whose i-th element is 1 and the rest are zeros. $\boldsymbol{e}_i^T \hat{\boldsymbol{u}}_1^{\mathrm{s}}$ thus extracts the i-th element of $\hat{\boldsymbol{u}}_1^{\mathrm{s}}$, which is, again, the fundamental Fourier coefficient of the dominant fixed-interface mode. This method will perform well if the change of the mode shape and thus the change of $\hat{\boldsymbol{f}}^{\mathrm{a}}$ between two iterations of the coupled solver is moderate.

4.4 Extension of the FD-FSI Solver to Forced Response Problems

The response amplitude due to e.g. an incoming wake is computed as a function of the excitation frequency. However, close to the resonance peak, overhanging branches of the response amplitude curve with respect to frequency are expected due to nonlinear contact forces in the structure. This necessitates the use of numerical path continuation, as explained in Section 2.8.3. As before, the rotor speed / excitation frequency parameter, ω, is treated as an unknown, this time however, the coupled FSI system is not autonomous (as in contrast to flutter). ω rather serves as a free parameter in order to compute the response amplitude curve as a function of ω by means of numerical path continuation, cf. **Figure 2.8**. In addition, path continuation facilitates numerical efficiency and robustness in ranges with strong gradient changes of the solution path, which are typical near resonances. It is useful to recall that the exact location of the resonance peak is a priori unknown and may significantly deviate from the natural frequency of the linearized system in the nonlinear case.

Two variants have been developed to obtain the branch of the coupled solution, the coupled continuation of the solution path, and the coupled re-iteration of selected solution points. To understand the rationale behind the method development, it is crucial to emphasize that the computational effort for the fluid sub-problem is orders of magnitude higher than that associated with the structural sub-problem.

4.4.1 Coupled Continuation of the Solution Path

For the coupled continuation of the solution path, the coupled FD-FSI solver as presented in Section 4.2 is essentially embedded into the path continuation procedure explained in Section 2.8.3. This algorithm is illustrated in **Figure 4.4**. If the switches in the flow chart

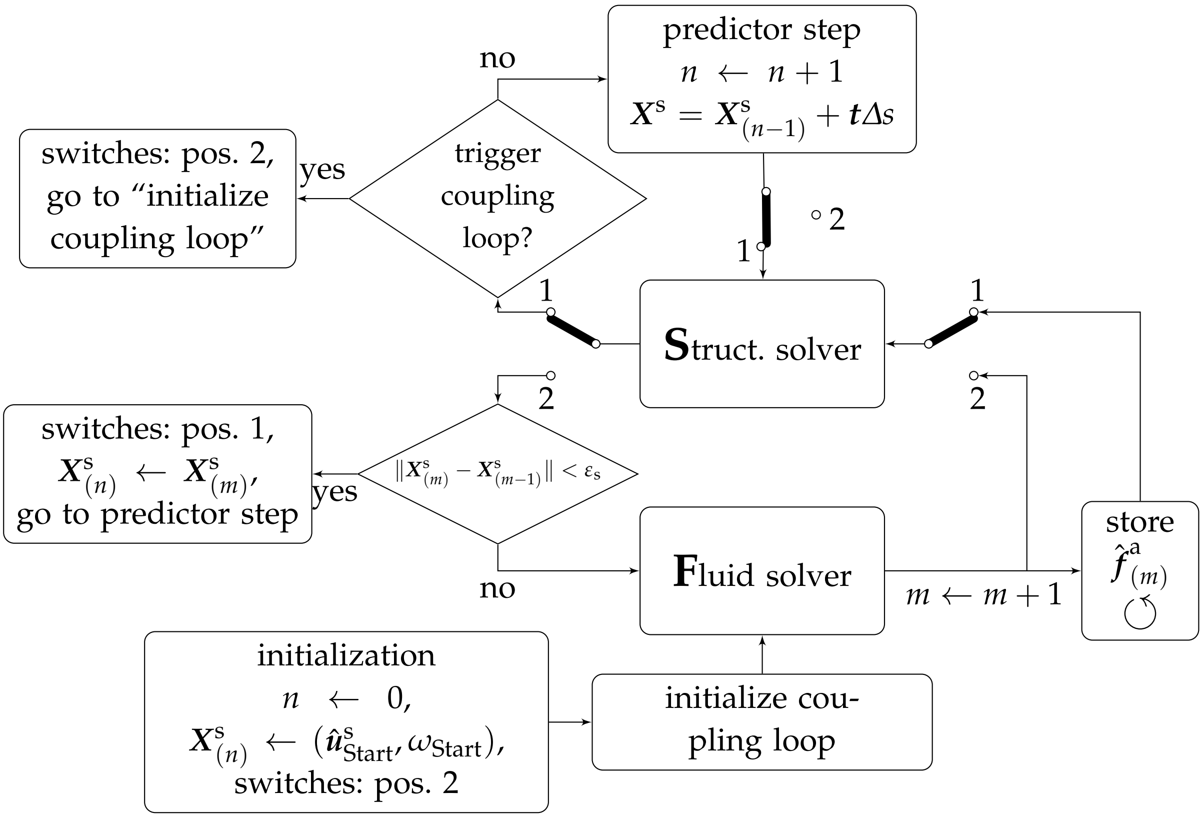

Figure 4.4: The coupled continuation of the solution path.

are in position 1, then the conventional predictor-corrector technique of numerical path continuation is recovered. Switching from position 1 to position 2 activates the fixed point iteration algorithm of the FD-FSI solver. In the FD-FSI algorithm's illustration **Figure 4.2**, dotted lines indicate the paths of the fixed point algorithm which are connected to the environment of the coupled continuation procedure, cf. **Figure 4.4**. During the continuation (switches in position 1), the extended structural residual, cf. Eq. (4.9), is solved with the pseudo arc-length constraint

$$r^{\text{con}}\left(X^s_{(n+1)}\right) = ||(X^s_{(n+1)} - X^s_{(n)})||^2 - \Delta s^2_{(n)} = 0 \tag{4.17}$$

to ensure local uniqueness and define where on the solution branch the next point ends up (*parametrization constraint*). This constraint is also in the case of the fixed point iterations of the FD-FSI solver (switches in position 2).

Starting from the prediction, the correction could be made, in principle, employing the coupled solver in each continuation step (n). To robustly continue a strongly nonlinear, near-resonant solution branch, often several hundred solution points are needed. Due to the large computational effort associated with the fluid solver, this may be practically infeasible. A simple way to reduce the computation effort is to approximate $\hat{f}^a$ for a number of points along the solution branch and only activate the coupling loop occasionally. For the approximation the superposition principle from Eq. (2.44) is used where $\hat{f}^a$ is split into the wake and vibration induced contributions $\hat{f}^a_{\text{wake}}$ and $\hat{f}^a_{\text{vib}}$ respectively. For $\hat{f}^a_{\text{vib}}$ the dominating-mode linearization approach from Eq. (4.16) is used. In order to be consistent with the last coupled solution result $\hat{\boldsymbol{f}}^{\mathrm{a}}_{(m)}$ obtained by the FD-FSI solver, $\hat{\boldsymbol{f}}^{\mathrm{a}}$ is linearized around this solution according to

$$\hat{\boldsymbol{f}}^{\mathrm{a}}\left(\hat{\boldsymbol{u}}^{\mathrm{s}}\right) = \hat{\boldsymbol{f}}^{\mathrm{a}}_{\mathrm{wake}} + \underbrace{\left(\hat{\boldsymbol{f}}^{\mathrm{a}}_{(m)} - \hat{\boldsymbol{f}}_{\mathrm{wake}}\right) \cdot \frac{\boldsymbol{e}^{\mathrm{T}}\hat{\boldsymbol{u}}^{\mathrm{s}}}{\boldsymbol{e}^{\mathrm{T}}\hat{\boldsymbol{u}}^{\mathrm{s}}_{(m)}}}_{\hat{\boldsymbol{f}}_{\mathrm{vib}}} . \tag{4.18}$$

Different criteria are conceivable for activating the coupling loop, which may account, for instance, for a change of amplitude or rotor speed. In the present work, the coupling loop was simply activated after a fixed number of solution points. As alternative, the coupling loop was activated when the vibrational deflection shape had changed to a certain extent. To quantify the change of the deflection shape, the correlation measure

$$\beta\left(\hat{\boldsymbol{u}}^{\mathrm{s}}\right) = 1 - \left(\frac{\Re\left\{\left(\hat{\boldsymbol{u}}^{\mathrm{s}}\right)^{\mathrm{H}}\hat{\boldsymbol{u}}^{\mathrm{s}}_{(n-1)}\right\}}{\|\hat{\boldsymbol{u}}^{\mathrm{s}}\|\,\|\hat{\boldsymbol{u}}^{\mathrm{s}}_{(n-1)}\|}\right)^{2} \tag{4.19}$$

was used, where H denotes the Hermitian. Upon completion of the coupling loop, the path continuation is carried on.

The linearization of the aerodynamic force according to Eq. (4.18) is also used as convergence acceleration inside the structural solver during the FD-FSI coupling iterations analogously to the application of the FD-FSI solver to flutter problems, cf. Section 4.3.3. Hence, once the FD-FSI solver is converged, the solution is not affected by the linearization. It only introduces an error during the path continuation, when the FD-FSI solver is deactivated (i.e. for subsequent solution points for which the coupling loop is inactive).

4.4.2 Coupled Re-iteration of Selected Solution Points

An important weakness of the coupled continuation is that it is inherently sequential; the computationally involved fluid solver iterations cannot be run in parallel. This motivated the development of the coupled re-iteration approach. First, the whole solution branch is computed in a decoupled way, i. e., using the structural solver only. For the aerodynamic force, a low-fidelity state-of-the-art model can be used; e g. the linear superposition of the wake-induced loading and an approximation of the vibration-induced loading using a single modal aerodynamic influence coefficient. Second, a relevant subset of solution points along the branch are selected. Here, regions that are of high engineering relevance, such as the resonance peak, can be resolved with a finer spacing of points. Finally, starting from this subset of points of the decoupled solution, the coupled FD-FSI solver is applied to obtain a corresponding point on the branch of the coupled solution. This idea is illustrated in **Figure 4.5**. It should be emphasized that the coupled solver can be applied to all selected solution points in parallel. To define where the corresponding point ends up on the new solution branch, it is required that the new solution $\boldsymbol{X}^{\mathrm{s}}$ lies on the hyper-plane orthogonal to the tangent $\boldsymbol{t}$ at the point $\boldsymbol{X}^{\mathrm{s}}_{\mathrm{ref}}$ on the old solution branch. This is enforced

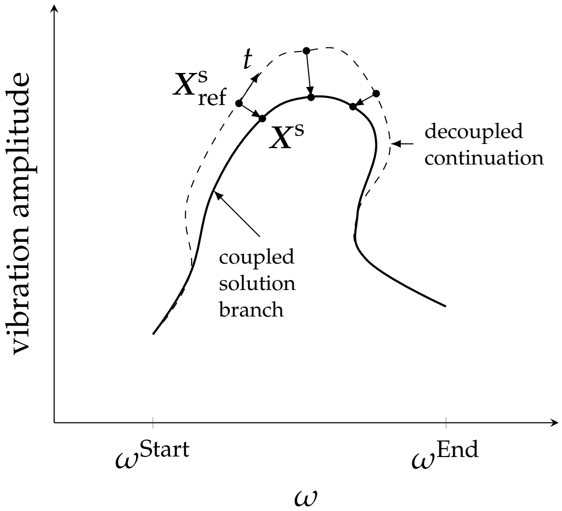

Figure 4.5: Numerical path continuation using a tangent predictor in combination with an arc-length constraint

by setting the constraint residual of Eq. (4.9) to

$$r^{con}(X^s) = t^T (X^s - X^s_{ref}) . \tag{4.20}$$

It is expected that this parametrization constraint is relatively robust to a substantial change in topology between old and new solution branch, compared to, for instance, the local parametrization obtained by imposing a fixed rotor speed/excitation frequency.

4.5 Data Exchange at the Fluid-Structure Interface and Fluid Mesh Deformation

For all methods introduced in this chapter, the fluid mesh must deform conforming to the structural deformation at the blade surface and the fluid forces must be transferred back to the structural solver (either for the coupled solver or for the evaluation of the damping ratio). In the following subsections, the methods used for transferring the data are presented.

4.5.1 Interpolation of Surface Data and Conservation of Energy at the Fluid-Structure Interface

For transferring the displacement data from the structure mesh, the structural vertex based (harmonic) displacements $\hat{q}_{FE}$ are interpolated onto the fluid mesh at the boundary $\Gamma_{\text{Blade Surface}}$,

$$\hat{q}_{FV}(x)^{\text{interpolated}} = \Phi(\hat{q}_{FE}, x) \quad \forall x \in \Gamma_{\text{Blade Surface}} , \tag{4.21}$$

using a bilinear interpolation function Φ with respect to the spatial coordinate $\boldsymbol{x}$. From this a linear relation for the vertex based harmonic fluid mesh surface displacements

$$\hat{\boldsymbol{q}}_{k,\mathrm{FV}} = \boldsymbol{L}\hat{\boldsymbol{q}}_{k,\mathrm{FE}} \quad k = 0, \ldots, K \tag{4.22}$$

can be derived where $\boldsymbol{L}$ denotes the interpolation matrix, cf. Eq. (2.24). Inserting the relation between nodal displacements and generalized coordinates Eq. (2.4) into Eq. (4.22) yields

$$\hat{\boldsymbol{q}}_{k,\mathrm{FV}} = \boldsymbol{L}\boldsymbol{T}\hat{\boldsymbol{u}}^{\mathrm{s}}_{k} = \boldsymbol{T}'\hat{\boldsymbol{u}}^{\mathrm{s}}_{k}, \tag{4.23}$$

where $\boldsymbol{T}' = \boldsymbol{L}\boldsymbol{T}$ is the structural ROM's basis vectors interpolated on the fluid mesh, which can be computed once in a preprocessing step. This allows to directly compute the (harmonic) deformation of the fluid mesh surface from the generalized coordinates $\hat{\boldsymbol{u}}^{\mathrm{s}}$.

Analogous to the conservative approach presented in [4] for time marching schemes, the fluid forces are interpolated according to

$$\hat{\boldsymbol{f}}^{\mathrm{a}}_{\mathrm{FE}} = \boldsymbol{L}^{\mathrm{T}}\hat{\boldsymbol{f}}^{\mathrm{a}}_{\mathrm{FV}} \tag{4.24}$$

with $\hat{\boldsymbol{f}}^{\mathrm{a}}_{\mathrm{FV}}(\hat{\boldsymbol{u}}^{\mathrm{a}})$ containing the vertex based (harmonic) forces due to the surface pressure of the fluid mesh, analogous to Eq. (2.30) including higher harmonics. Notice that $\boldsymbol{L}$ is a real matrix and thus its transpose is equal to its hermitian. In order to obtain the generalized aerodynamic forces $\hat{\boldsymbol{f}}^{\mathrm{a}}$, the fluid forces on the structure surface mesh $\hat{\boldsymbol{f}}^{\mathrm{a}}_{\mathrm{FE}}$ are projected on the basis vectors of the structural ROM (cf. Section 2.2.2), which yields

$$\hat{\boldsymbol{f}}^{\mathrm{a}} = \boldsymbol{T}^{\mathrm{H}}\hat{\boldsymbol{f}}^{\mathrm{a}}_{\mathrm{FE}} = \boldsymbol{T}^{\mathrm{H}}\boldsymbol{L}^{\mathrm{H}}\hat{\boldsymbol{f}}^{\mathrm{a}}_{\mathrm{FV}} = \boldsymbol{T}'^{\mathrm{H}}\hat{\boldsymbol{f}}^{\mathrm{a}}_{\mathrm{FV}}\,. \tag{4.25}$$

In general, conservative interpolation has the disadvantage of the occurrence of unphysical spatial oscillations in the fluid force once it is interpolated using the transpose of $\boldsymbol{L}$ [4]. In the special case of a reduced structural ROM as introduced above, however, the spatial oscillations are of no practical relevance since they are filtered out during the projection on the ROM's basis.

The conservative approach used above is valid for time marching schemes. It is however easily shown that it can also be applied to the current frequency domain approach. To start with, global conservation of work across the FSI interface for one fundamental period T is required:

$$\int_0^T \boldsymbol{f^{\mathrm{a}}}_{\mathrm{FE}}(t)^{\mathrm{T}}\dot{\boldsymbol{q}}_{\mathrm{FE}}(t)dt = \int_0^T \boldsymbol{f^{\mathrm{a}}}_{\mathrm{FV}}(t)^{\mathrm{T}}\dot{\boldsymbol{q}}_{\mathrm{FV}}(t)dt\,. \tag{4.26}$$

Inserting the truncated Fourier series of the forces and displacements yields

$$\begin{aligned}&\int_0^T \Re\left\{\sum_k \hat{\boldsymbol{f}}^{\mathrm{a}}_{k,\mathrm{FE}}e^{ik\omega t}\right\}^{\mathrm{T}} \Re\left\{\sum_k ik\omega\hat{\boldsymbol{q}}_{k,\mathrm{FE}}e^{ik\omega t}\right\}dt\\ =&\int_0^T \Re\left\{\sum_k \hat{\boldsymbol{f}}^{\mathrm{a}}_{k,\mathrm{FV}}e^{ik\omega t}\right\}^{\mathrm{T}} \Re\left\{\sum_k ik\omega\hat{\boldsymbol{q}}_{k,\mathrm{FV}}e^{ik\omega t}\right\}dt\,.\end{aligned} \tag{4.27}$$

Inserting Eq. (4.22) into Eq. (4.27) and rearranging the RHS results in

$$\begin{aligned}&\int_0^T \Re\left\{\sum_k \hat{\boldsymbol{f}}^{\mathrm{a}}_{k,\mathrm{FE}} e^{ik\omega t}\right\}^{\mathrm{T}} \Re\left\{\sum_k ik\omega \hat{\boldsymbol{q}}_{k,\mathrm{FE}} e^{ik\omega t}\right\} dt \\ &= \int_0^T \Re\left\{\sum_k \boldsymbol{L}^{\mathrm{T}} \hat{\boldsymbol{f}}^{\mathrm{a}}_{k,\mathrm{FV}} e^{ik\omega t}\right\}^{\mathrm{T}} \Re\left\{\sum_k ik\omega \hat{\boldsymbol{q}}_{k,\mathrm{FE}} e^{ik\omega t}\right\} dt \qquad (4.28)\end{aligned}$$

which is satisfied when $\hat{\boldsymbol{f}}^{\mathrm{a}}_{k,\mathrm{FE}}$ is computed according to Eq. (4.24).

4.5.2 Fluid Mesh Deformation

Without further treatment, the deformation of the fluid mesh surface according to $\hat{\boldsymbol{q}}_{\mathrm{FV}}$ would lead to degenerated FV cells. Hence, the inner FV mesh needs to be deformed appropriately in order to keep a good mesh quality. Similar to Eq. (4.23), the mesh deformation is treated as a linear superposition,

$$\chi\left(\boldsymbol{u}^{\mathrm{s}}\right) = \chi_0 + [\chi_1\, \chi_2 \cdots \chi_N]\boldsymbol{u}^{\mathrm{s}}\,, \qquad (4.29)$$

of the mesh deformations χ_ℓ with $N^{\mathrm{s}} \geq \ell \geq 1$ corresponding to a unit displacement of the ℓ-th generalized structural coordinate, and the coordinates $\boldsymbol{u}^{\mathrm{s}}$ used as weights. χ_0 is the location of the undeformed mesh. χ_ℓ with $\ell \geq 1$ are computed analogous to a linear-elastic deformation problem [65]

$$\nabla \cdot (\mu(\boldsymbol{x})\nabla\chi_\ell\,(\boldsymbol{x})) = 0 \qquad \forall \boldsymbol{x} \in \Omega_{\text{Fluid Domain}}\,, \qquad (4.30)$$

$$\chi_\ell(\boldsymbol{x}) = \Phi(\boldsymbol{T}\boldsymbol{e}_\ell, \boldsymbol{x}) \qquad \forall \boldsymbol{x} \in \Gamma_{\text{Blade Surface}}\,, \qquad (4.31)$$

where the vector $\boldsymbol{e}_\ell$ is the ℓ-th unit vector (containing only zeros, except for the ℓ-th element which is equal to one), ∇ denotes the gradient, $\cdot$ denotes the inner product, and $\mu(\boldsymbol{x})$ corresponds to the equivalent elastic modulus. In each cell, $\mu(\boldsymbol{x})$ is made proportional to the inverse of the cell volume which makes sure that small cells, e g. in a boundary layer, are not sheared excessively. Eqs. (4.30)-(4.31) are efficiently solved with the generalized minimal residual method. The above equations are presented with state variables ($\boldsymbol{u}^{\mathrm{s}}$), however they are also valid for harmonic quantities ($\hat{\boldsymbol{u}}^{\mathrm{s}}$).

Having an explicit expression for the mesh deformation, obtained in a pre-processing step, substantially reduces the computation effort compared to computing the mesh deformation simultaneously with the solution of the governing equations of the fluid. The described procedure preserved good mesh quality throughout the amplitude range considered in this work.

5 Numerical LPT Rotor Testcase with Span-to-Chord Ratio of 4

The contents of this chapter is primarily taken from [D]. A model of a low pressure turbine bladed disk with interlocked tip shroud is considered. The structural finite element model of one sector is shown in **Figure 5.1**; the whole bladed disk contains 50 sectors. Geometric and material properties are listed in **Table 5.1**. Mistuning is known for its potential to significantly distort the modal deflection shapes and for its tendency to stabilize flutter [46, 44]. On the other hand, for the case of strong inter-sector coupling, here via tip shrouds, the effect of small mistuning is known to be negligible [67]. Thus, the system is assumed as rotationally periodic; i. e., each sector has identical properties. It is further assumed that the periodic response of the system inherits the symmetry suggested by the system; i. e., the response is assumed to take the form of a traveling wave, where each sector undergoes the same oscillation, however, with a constant time shift between neighboring sectors. This permits to reduce the problem domain to only a reference sector with appropriate time-shift boundary conditions at the cyclic sector boundaries.

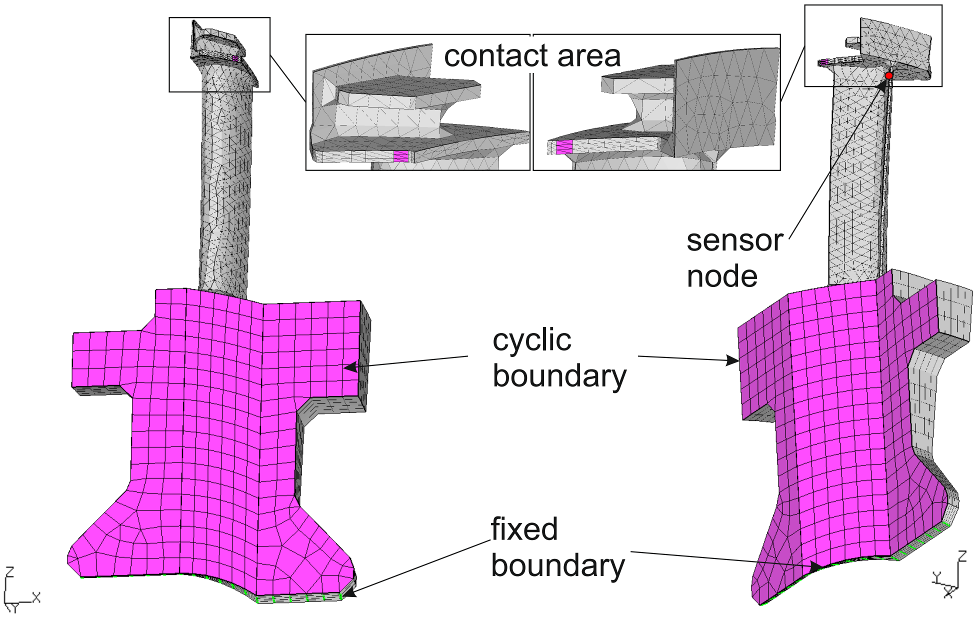

Figure 5.1: Structural finite element model of the sector of a bladed disk (kindly provided by MTU Aero Engines AG).

Nonlinear dry frictional interactions are taken into account between the tip shrouds of

Number of blades	50
Blade span	86 mm
Blade chord	22 mm
Youngs modulus blade + disk	110 GPa
Poisson ratio blade + disk	0.343
Density blade + disk	$4.43 \times 10^3\,\mathrm{kg\,m^{-3}}$
Youngs modulus shroud	210 GPa
Poisson ratio shroud	0.3
Density shroud	$7.83 \times 10^3\,\mathrm{kg\,m^{-3}}$
Radius hub	134 mm
Radius tip	221 mm

Table 5.1: Geometric and material properties of the benchmark model [D].

neighboring blades. In accordance with the cyclic symmetry assumption, the contact is defined under consideration of the time shift between the interfaces on either side of the sector. In the tangential plane, dry friction is modeled in terms of the common elastic Coulomb law, see e g. [34, 20, 52], which can be written in differential form as

$$\mathrm{d}\boldsymbol{p}_\mathrm{t} = \begin{cases} k_\mathrm{t}\,\mathrm{d}\boldsymbol{g}_\mathrm{t} & : \ \|\boldsymbol{p}_\mathrm{t} + k_\mathrm{t}\,\mathrm{d}\boldsymbol{g}_\mathrm{t}\| \leq \mu p_\mathrm{n} \\ \frac{k_\mathrm{t}\mathrm{d}\boldsymbol{g}_\mathrm{t}}{\|\boldsymbol{p}_\mathrm{t} + k_\mathrm{t}\,\mathrm{d}\boldsymbol{g}_\mathrm{t}\|} & : \ \|\boldsymbol{p}_\mathrm{t} + k_\mathrm{t}\,\mathrm{d}\boldsymbol{g}_\mathrm{t}\| > \mu p_\mathrm{n} \end{cases} . \tag{5.1}$$

Herein, $\boldsymbol{p}_\mathrm{t}$ and p_n are tangential traction vector and normal pressure, $\boldsymbol{g}_\mathrm{t}$ is the tangential gap vector, and k_t is the tangential stiffness per area value. A constant friction coefficient μ is considered for both static and dynamic friction. The normal pressure p_n is assumed as time-constant and uniformly distributed within the contact interface. Hence, the contact is always closed in the normal direction; liftoff is prohibited. The specific values of μp_n and k_t are defined later. The contact law in Eq. (5.1) is spatially discretized using six C2D3 surface elements with a total of 8 nodes (each side), conform with the underlying solid elements. The elements and nodes of the opposing sides coincide in the cyclic sense. The nodes are used as integration points. Dry frictional damping in the mechanical joints is the only source of structural damping considered in this work; i. e., material damping is neglected. Fully sticking contacts are assumed during the static analysis step for simplicity. This allows to select the active contact region (where friction is modeled) in order to obtain numerical test case configurations with a relatively large (nonlinear) impact of the contact friction on the vibration behavior

For convenience, a coordinate transform to the relative tangential displacements at each contact node pair is carried out (two orthogonal directions per node pair). Assuming small vibrations around the equilibrium position, the structural elastic and inertia forces are linear in the structural displacement. To reduce the mathematical model order, the Craig-Bampton method is applied [12]. Here, the static constraint modes are associated with the relative displacements at the contact node pairs. Based on the results of a convergence study, the 5 lowest-frequency normal modes were retained. Consequently, the dimension of $\boldsymbol{u}^{\mathrm{s}}$ is $N^{\mathrm{s}} = 2 \times 8 + 5 = 21$.

5.1 Fluid Model

The Mach number at the inlet is 0.33 and at the exit 0.75. The Reynolds number with respect to the exit flow conditions and the chord of the blade is 720 000 and the total pressure ratio amounts to 1.02. The equations are closed with the k-ω turbulence model [69], the ideal gas law and the Sutherland law for the molecular viscosity. The problem domain is discretized with a finite volume mesh containing $N_{\mathrm{cell}} = 820,000$ cells per sector. In accordance with the assumption of a traveling-wave-type response, only a single passage of the blade row is considered in the fluid model. At the cyclic sector boundaries, phase lag boundary conditions are imposed. At the inlet and outlet, two-dimensional non-reflecting boundary conditions are considered [55].

5.1.1 Aerodynamic Damping for Sticking and Frictionless Sliding Limit Cases

Elastic sticking and frictionless sliding contact conditions are linear limit cases of the elastic dry friction nonlinearity reached for sufficiently small and (asymptotically) for very large vibration amplitudes, respectively. For very small vibration amplitudes the norm of the frictional traction will not exceed μp_{n}. In this case the contact elements will behave as linear springs (which corresponds to elastic sticking). For the case of very large amplitudes the contact elements slide most of the time during the vibration cycle. The norm of the frictional traction is limited by the finite value of μp_{n}, and thus become negligible compared to the stresses within the body, which further increase linearly with the vibration amplitude. Hence, the behavior for large vibrations asymptotically approaches the behavior for frictionless sliding.
By convention, a positive ND refers to a wave traveling in the same direction as the rotor, while a negative ND refers to the opposite direction. The aerodynamic damping has a characteristic dependence on the wave number and the traveling direction of a particular mode. **Figure 5.2(a)** depicts the aerodynamic damping ratio as function of the ND for the lowest-frequency mode family, for both sticking and frictionless sliding limit cases. The aerodynamic damping shows a considerable sensitivity to the contact boundary conditions at the tip shrouds. The detailed view in **Figure 5.2(b)** reveals that the contact boundary conditions even affect the sign of the aerodynamic damping. The ND -7 mode, for instance, is aerodynamically self-excited for sticking contact conditions but positively damped for frictionless sliding contact conditions. Consequently, a stable LCO can be expected here. Conversely, the ND -4 mode receives positive aerodynamic damping for sticking, but negative damping for free sliding boundary conditions. Thus, one can expect that this mode loses stability beyond a certain vibration level, as the nonlinear contact in-

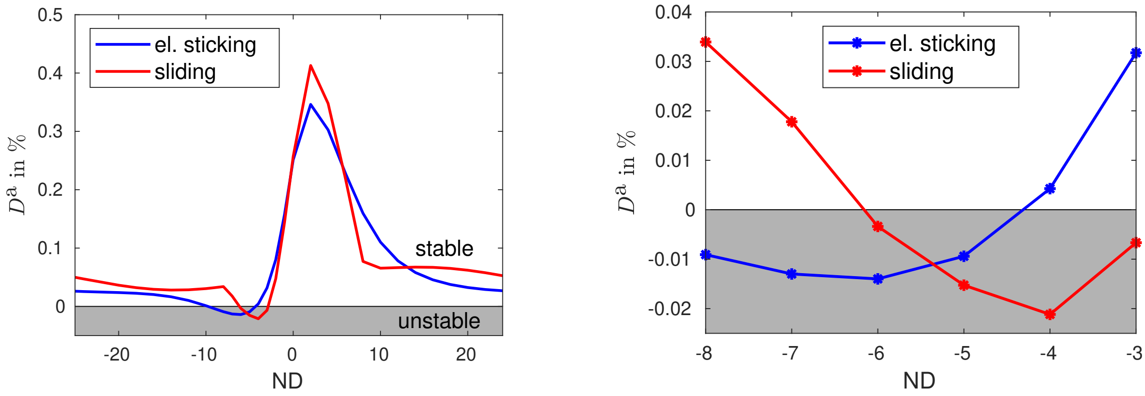

(a) (b)

Figure 5.2: Aerodynamic damping ratio vs. ND, configuration 2: (a) Overview; (b) Detail [D].

teractions gradually transition from the sticking to the frictionless sliding limit case. This flutter curve corresponds to configuration 2, of which the stability limit of ND -4 is analyzed later in more detail.

5.1.2 Dependence of Aerodynamic Forces on the Structural Response Level

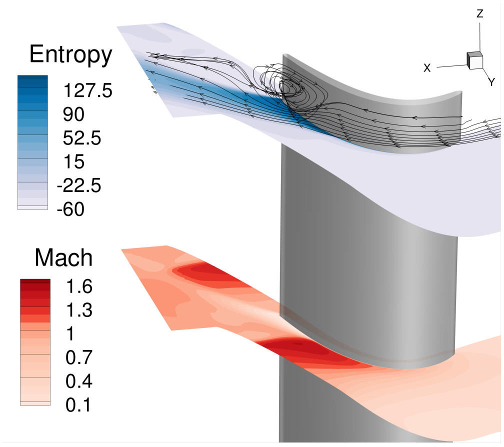

Figure 5.3: Instantaneous flow field around the blade (mach and entropy contours), configuration 2 [D].

Figure 5.3 shows an instantaneous snapshot of the cyclic symmetric flow field around the blade. The contours are plotted at constant radius. The lower contour shows the position of a shock and the upper contour visualizes the generation of entropy due to the flow separation in the latter part of the suction side. The flow separation covers roughly the upper two third of the blade span.

In the following, the vibrational amplitude denoted by $\hat{u}_{\text{Sensor}}$ is the amplitude of the (circumferential) Y-component of the sensor node depicted in **Figure 5.1**. This coordinate is chosen since the investigated mode with ND -4 deforms considerably in this direction at the selected sensor node. For this nodal diameter, the tip shroud displacement is relatively large, such that the displacement of the sensor node (located near the tip shroud) properly reflects the global vibration level of the blade. In the following plots $\hat{u}_{\mathrm{Sensor}}$ is normalized by the blade span L_{Span}.

To analyze the amplitude-dependence of the aerodynamic forces, the aerodynamic damping is computed for different vibration amplitudes of the mode shape $\boldsymbol{\psi}^{\mathrm{stick}}$ and natural frequency ω^{stick} obtained with sticking contact conditions. In **Figure 5.4** a nonlinear behavior of the aerodynamic response can be identified, however the change in damping due to the amplitude is not significant compared to the impact of the ND or the contact conditions. For amplitudes larger than $\hat{u}_{\mathrm{Sensor}}/L_{\mathrm{Span}} = 2 \times 10^{-3}$ the fluid solver failed to converge. However, the computed range covers the LCO amplitudes which will later be analyzed. The modes associated with several other NDs showed similar behavior under various flow conditions for the given test case.

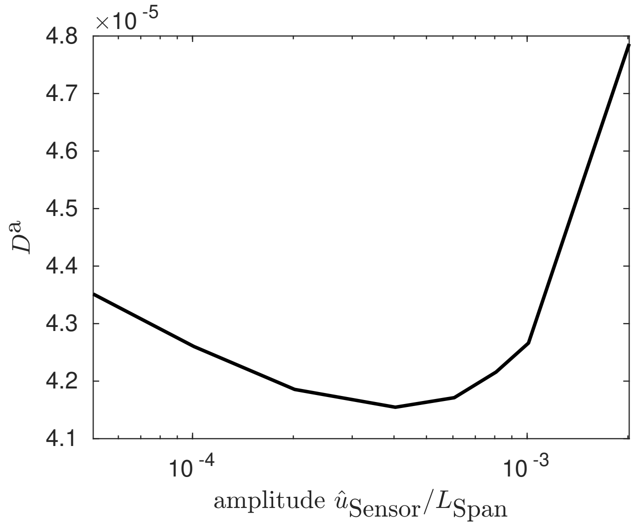

Figure 5.4: Aerodynamic damping ratio vs. amplitude for ND -4 mode under sticking contact conditions, configuration 2 [D].

It should be emphasized that a linear dependence of the aerodynamic forces on the vibration amplitude should not be confused with a linear dependence on the conservative flow variables. The highly unsteady flow phenomena can certainly be captured only with nonlinear computational fluid dynamics. Even if there is no significant direct amplitude dependence (for fixed deflection shape and frequency, $\boldsymbol{\psi}^{\mathrm{stick}}$, ω^{stick}), the nonlinear contact conditions will induce an amplitude dependent natural frequency $\omega^{\mathrm{nl}}(\hat{u})$ and deflection shape $\boldsymbol{\psi}^{\mathrm{nl}}(\hat{u})$, which in turn generates an *indirect amplitude dependence* of the aerodynamic damping and stiffness.

5.2 Benchmark Configurations

If multiple ND modes are aerodynamically self-excited, it is expected that each of these gives rise to a limit cycle [43], which however is not necessarily stable, as shown later in

Chapter 7. The larger the aerodynamic self-excitation ($-D^{\mathrm{a}}$) of a given mode, the larger is the corresponding basin of attraction, i. e., the set of initial conditions from which the trajectories approach the respective limit cycle. As a representative example, the fundamental mode with ND -4 is analyzed, which also has the highest aerodynamic self-excitation in the frictionless sliding limit case shown in **Figure 5.2**.

configuration:	1	2
inlet total pressure	1.9×10^5 Pa	1.9×10^5 Pa
static pressure at outflow	9.0×10^4 Pa	7.8×10^4 Pa
contact area	4.55 mm^2	4.55 mm^2
contact stiffness k_{t}	2.19 N mm^{-3}	21.95 N mm^{-3}
limit frictional traction μp_{n}	0.22 N mm^{-2}	6.58×10^{-4} N mm^{-2}
D^{a} (stick)	-1.8×10^{-4}	4.3×10^{-5}
D^{a} (slip)	*	-2.1×10^{-4}
natural frequency (stick)	437 Hz	520 Hz
natural frequency (slip)	418 Hz	418 Hz

Table 5.2: Parameters of the two benchmark configurations and corresponding linear modal properties. *The aerodynamic damping D^{a} (slip) of configuration 1 (used for the stable limit cycle) was not computed since it is not relevant.

Two configurations are studied in the following, which differ in terms of contact properties and static outflow pressure, as listed in **Table 5.2**. During a long service life, the normal preload in the interlocked shrouds can decrease significantly due to creep and wear. This is the motivation to set different normal preloads in the two configurations. In this sense, configuration 1 corresponds to the *initially built setting*, while configuration 2 corresponds to a *setting after a long service life*. First the expected and well-known stable limit cycle is analyzed for configuration 1. By reducing the contact stiffness parameter for this configuration, the natural frequency and thus also the reduced frequency for the sticking case are reduced leading to an aerodynamically unstable situation for small amplitudes. As discussed in Section 5.1.1, the ND -4 mode is stable under sticking contact, but unstable under frictionless sliding contact in configuration 2, where the reduced frequency is higher for sticking contact conditions. This suggests that there is an unstable limit cycle (stability limit), which will be analyzed subsequently.

For the results presented in the following, a single harmonic was found sufficient for the Harmonic Balance equation of the structural subproblem ($H^{\mathrm{s}} = 1$), while two harmonics were needed to properly resolve the dynamic processes in the fluid domain ($H^{\mathrm{a}} = 2$).

5.3 Stable Limit Cycle (configuration 1)

5.3.1 Comparison of the Results Obtained by Energy Methods and FD-FSI Solver

Figure 5.5 shows the structural and aerodynamic damping ratios as function of the vibration amplitude. For sufficiently small vibration amplitudes, the contact is always sticking, and thus the structure behaves linear and there is no frictional dissipation ($D^{\mathrm{s}} = 0$). As soon as the vibration amplitude is sufficiently large (here beyond $|\hat{u}_{\mathrm{Sensor}}| \approx 0.185\%\, L_{\mathrm{Span}}$), dissipative sliding friction starts to occur, which leads to an increase of D^{s}. For the given contact stiffness and area, a maximum structural damping ratio of about 4% is reached. The aerodynamic damping ratio D^{a} is negative, has a relatively small magnitude and does not considerably depend on the amplitude, as compared to D^{s}. Recall that a limit cycle requires $D^{\mathrm{s}} + D^{\mathrm{a}} = 0$. Hence, a limit cycle occurs at the intersections in **Figure 5.5(b)** where $D^{\mathrm{s}} = -D^{\mathrm{a}}$. Because of the relatively small magnitude of D^{a}, the aerodynamic self-excitation is cancelled by friction damping already just shortly beyond the onset of sliding friction. Consequently, the oscillation frequency at the limit cycle is very close to that of the sticking limit case. Indeed, the difference in frequency is only 0.003 % here. Therefore, the frequency-dependence in the refined energy methods was neglected in this case. In **Table 5.3** the results of the energy methods and the FD-FSI solver are summarized in terms of amplitude and frequency of the stable limit cycle. The black lines refer to the refined energy method while the blue lines refer to the conventional energy method (where D^{a} is constant). The structural damping for the conventional energy method is explicitly evaluated as a function of amplitude (but with constant vibration shape). It can be concluded that all methods are in very good agreement for this particular case. For completeness, also the change of the vibrational deflection shape is assessed by computing the MAC (modal assurance criterion) defined as the correlation measure

$$MAC(\boldsymbol{\psi}_1, \boldsymbol{\psi}_2) = \frac{|\boldsymbol{\psi}_1^{\mathrm{H}} \boldsymbol{\psi}_2|^2}{(\boldsymbol{\psi}_1^{\mathrm{H}} \boldsymbol{\psi}_1)(\boldsymbol{\psi}_2^{\mathrm{H}} \boldsymbol{\psi}_2)} \,. \tag{5.2}$$

The MAC values shown in Table 5.3 are all very close to unity. Thus, it is concluded that the deflection shape at the stable limit cycle is practically identical in all methods and agrees well with the modal deflection shape obtained for sticking contact conditions.

5.3.2 Numerical Performance of the FD-FSI Solver

The decay of the residuals in either domain is shown in **Figure 5.6(a)** for the first four iterations of the FD-FSI solver. The residuals decrease with rates typical for the decoupled subproblems. The convergence of the limit cycle amplitude and frequency is depicted in **Figure 5.6(b)**. Recall that $\hat{u}_i^{\mathrm{s}}$ denotes the fundamental Fourier coefficient of the dominant fixed-interface mode. The results almost do not change after the first iteration and the

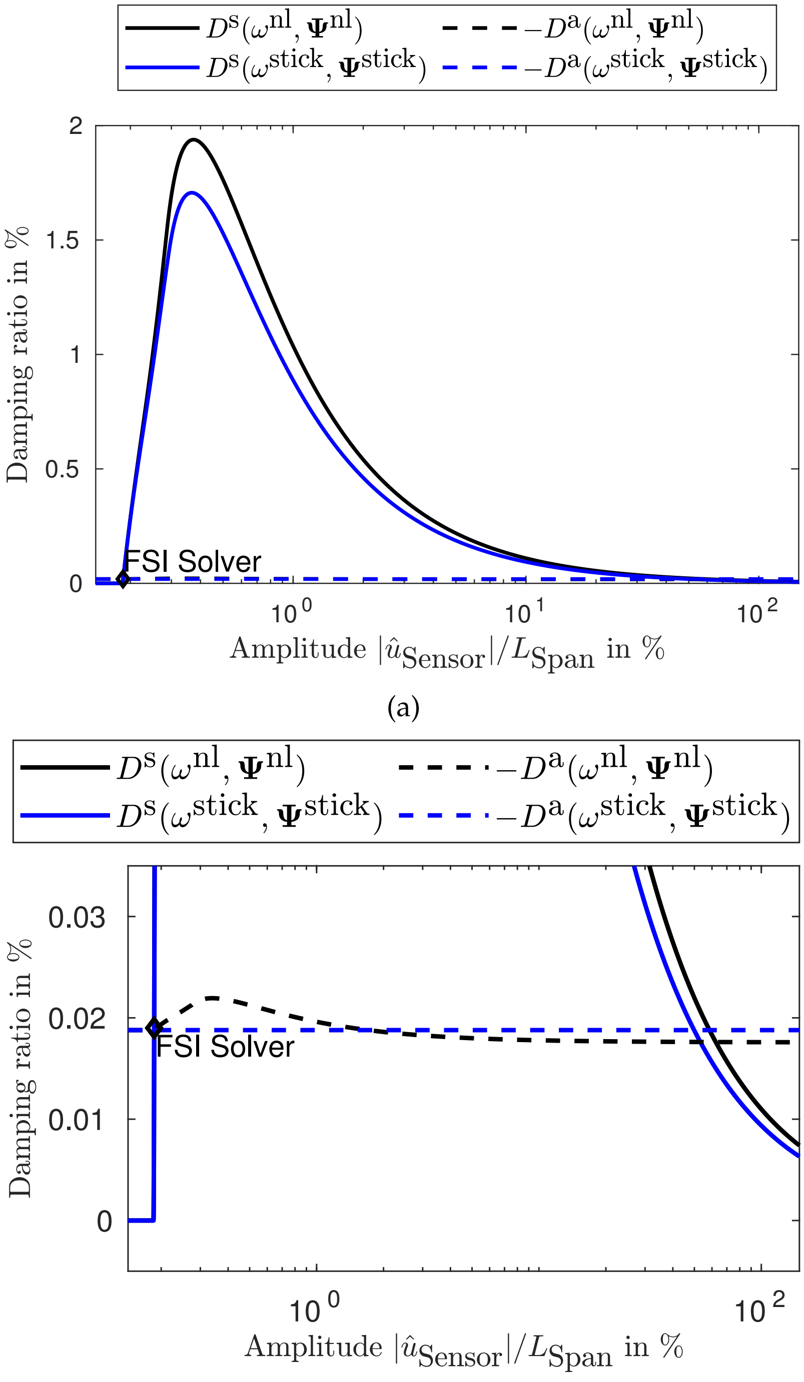

(a)

(b)

Figure 5.5: Results of the conventional and refined energy methods, and the FD-FSI solver, configuration 1: (a) Global view; (b) Detailed view at LCO solution.

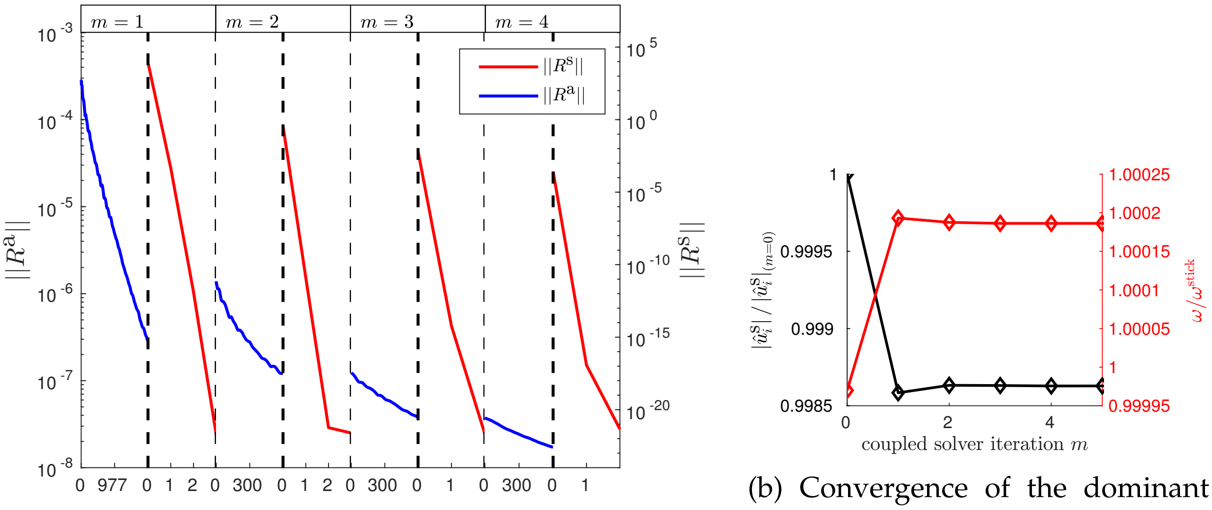

(a) Successive decay of the residuals in fluid and structural domain

(b) Convergence of the dominant amplitude and frequency of the limit cycle

Figure 5.6: Behavior of the FD-FSI solver, configuration 1

full-coupled solver reaches convergence in accordance with the specified tolerances already after 5 iterations. Both the linearization involving the frequency-constant influence coefficient matrix (with the natural frequency of the sticking contact) and the dominant-mode linearization were assessed and found to lead to numerically identical results in the same number of iterations. The simulation took 19.5 hours on 10 cores.

	Energy Method	Refined Energy Method	FD-FSI solver
Frequency	436.952 Hz	436.941 Hz	437.032 Hz
$\hat{u}_{\mathrm{Sensor}} / L_{\mathrm{Span}}$	1.861×10^{-3}	1.861×10^{-3}	1.859×10^{-3}
$MAC(\boldsymbol{\psi}, \boldsymbol{\psi}^{\mathrm{stick}})$	1	0.999 999 95	0.999 996 6
$MAC(\boldsymbol{\psi}, \boldsymbol{\psi}^{\mathrm{nl}})$	-	1	0.999 997 4

Table 5.3: Summary of stable limit cycle data.

5.4 Stability Limit (configuration 2)

5.4.1 Comparison of the Results Obtained by Energy Methods and FD-FSI solver

The structural and aerodynamic damping ratios are depicted as function of the vibration amplitude in **Figure 5.7**. In contrast to the case of the stable limit cycle, the unstable limit cycle does not occur close to the linear case with sticking contact conditions. Consequently, the oscillation frequency and the deflection shape differ considerably from the modal properties of the sticking limit case. The conventional energy method (blue lines) ignores the amplitude-dependence of the oscillation frequency and deflection shape (assuming $\boldsymbol{\psi}^{\mathrm{stick}}$, ω^{stick} for all $\hat{u}$), and thus the aerodynamic damping ratio is invariant according to this method. As the damping ratio is positive in the sticking limit case, the energy method does not predict a stability limit, but predicts stable behavior for all amplitudes.

In **Table 5.4** the results of the energy methods and the FD-FSI solver are summarized in terms of amplitude and frequency of the stability limit. The results of the refined energy method and the FD-FSI solver agree very well. The deviations of frequency, $\hat{u}_{\mathrm{Sensor}}$ are 0.02 %, 0.88 % respectively. The MAC values of about 0.91 with respect to the sticking limit case show that the vibrational deflection shape is significantly affected by the nonlinear contact interactions in the tip shrouds. This leads to a considerable influence on the aerodynamic response, cf. $-D^{\mathrm{a}}(\omega^{\mathrm{nl}}, \boldsymbol{\Psi}^{\mathrm{nl}})$ and $-D^{\mathrm{a}}(\omega^{\mathrm{nl}}, \boldsymbol{\Psi}^{\mathrm{stick}})$ in **Figure 5.8**. The vibrational deflection shape predicted by the coupled solver and the refined energy method agree very well, as indicated by a MAC value close to unity (right column, bottom row). This means that the vibrational deflection shape is mainly driven by structural forces, and can thus be well-represented by a nonlinear mode. Hence, the fluid does not add substantial stiffness (causing a significant frequency shift) or even change the deflection shape. The aerodynamic self-excitation merely determines the vibration level.

	Energy Method	Refined Energy Method	FD-FSI solver
Frequency	519.661 Hz	418.049 Hz	418.671 Hz
$\hat{u}_{\mathrm{Sensor}} / L_{\mathrm{Span}}$	-	1.57×10^{-3}	1.59×10^{-3}
$MAC(\boldsymbol{\psi}, \boldsymbol{\psi}^{\mathrm{stick}})$	1	0.910 69	0.910 73
$MAC(\boldsymbol{\psi}, \boldsymbol{\psi}^{\mathrm{nl}})$	-	1	0.999 996

Table 5.4: Summary of stability limit data.

5.4.2 Influence of the Modal Deflection Shape and Frequency

To further study the influence of the amplitude-dependent modal deflection shape $\boldsymbol{\psi}^{\mathrm{nl}}$ and frequency ω^{nl}, the refined energy method is applied with either the frequency or modal deflection shape held constant, denoted by $-D^{\mathrm{a}}(\omega^{\mathrm{stick}}, \boldsymbol{\Psi}^{\mathrm{nl}})$ and $-D^{\mathrm{a}}(\omega^{\mathrm{nl}}, \boldsymbol{\Psi}^{\mathrm{stick}})$, respectively. Both results are plotted in **Figure 5.8**. For larger amplitudes, there is a noticeable difference to $-D^{\mathrm{a}}(\omega^{\mathrm{nl}}, \boldsymbol{\Psi}^{\mathrm{nl}})$ which shows that both effects are important to determine the accurate flow response for this case. Here, the frequency dependency is mainly responsible for the aerodynamic behavior changing from damping to self-excitation. This appears plausible since a decrease in vibrational frequency leads to a decrease in reduced frequency which can trigger aerodynamic instability [62].

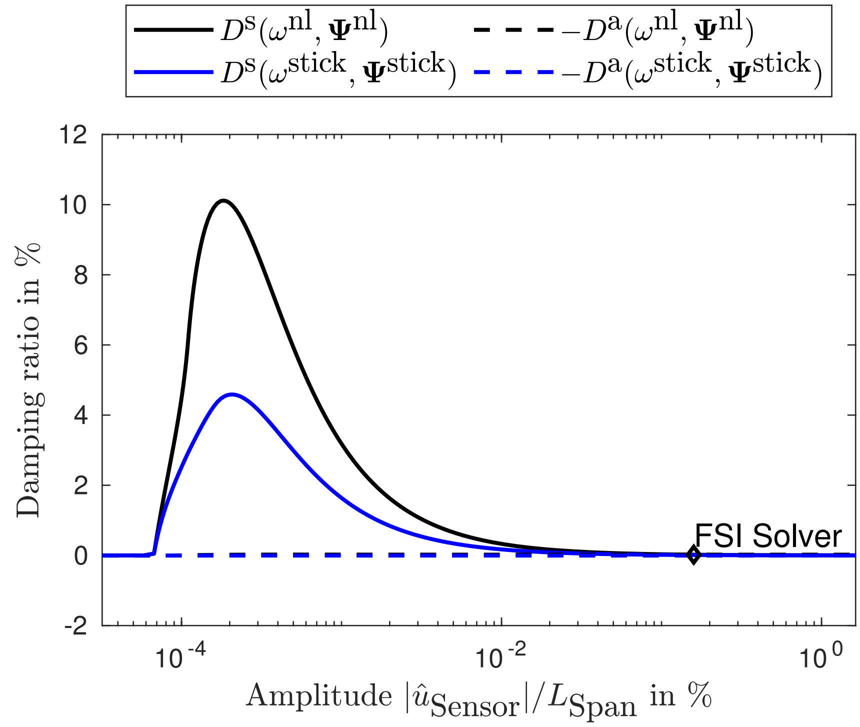

(a) Global view

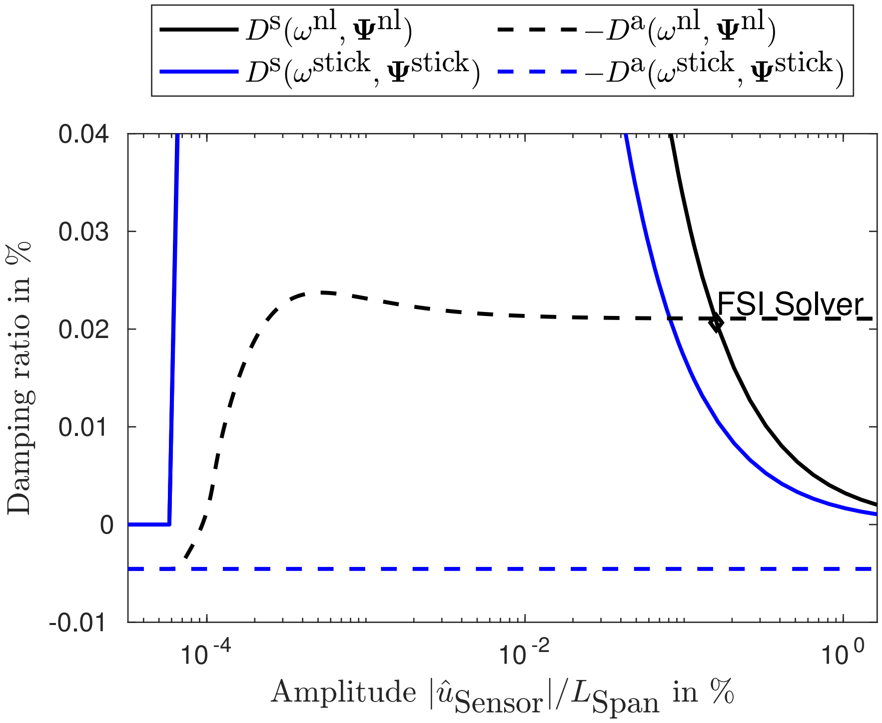

(b) Detailed view

Figure 5.7: Results of the conventional and refined energy methods, and the FD-FSI solver, configuration 2

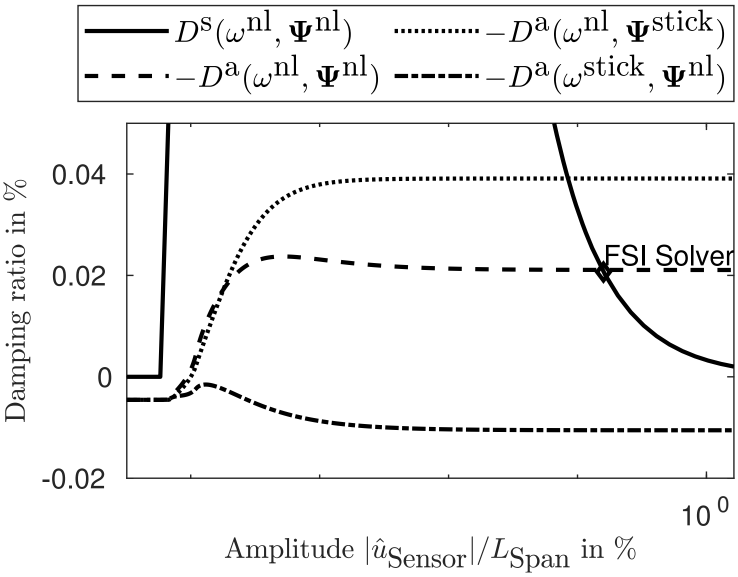

Figure 5.8: Results of the refined energy method (ND -4) with constant frequency or constant modal deflection shape.

5.4.3 Numerical Performance of the FD-FSI Solver

The convergence behavior of the FD-FSI solver is illustrated in **Figure 5.9(a)** and **Figure 5.9(b)**. Again, the solver converges quickly, but more iterations are needed for the same tolerances compared to the previous benchmark configuration. In this configuration, the type of linearization used for the representation of the aerodynamic forces within the structural subproblem (cf. Section 4.3.3) was found to have an important influence. The dominating mode linearization performed well, whereas the frequency-dependent influence-coefficient-matrix linearization did not lead to convergence in a reasonable number of iterations. The behavior could be improved by introducing a relaxation factor of 0.3 for $\hat{\boldsymbol{u}}^{\mathrm{s}}_{(m)}$, which took however approx. 60 coupled solver iterations. The coupled solver required 24 hours and 62 hours on 10 cores for the dominating-mode linearization and the influence-coefficient-matrix linearization (with the described relaxation) respectively.

5.5 Discussion of the Computational Effort of FD-FSI Solver and Refined Energy Method

The computational costs for solving the structural subproblem was practically negligible in the considered benchmark. For instance, the nonlinear modal analysis took only about 30 seconds. For the refined energy method, thus the computational effort is driven by the computation of the influence coefficient matrix $\boldsymbol{G}$. This effort scales with the number of generalized coordinates, N, of the reduced structural model (here $N = 21$). For one column of $\boldsymbol{G}$, one flow simulation is required which took approximately 5.25 hours on 9

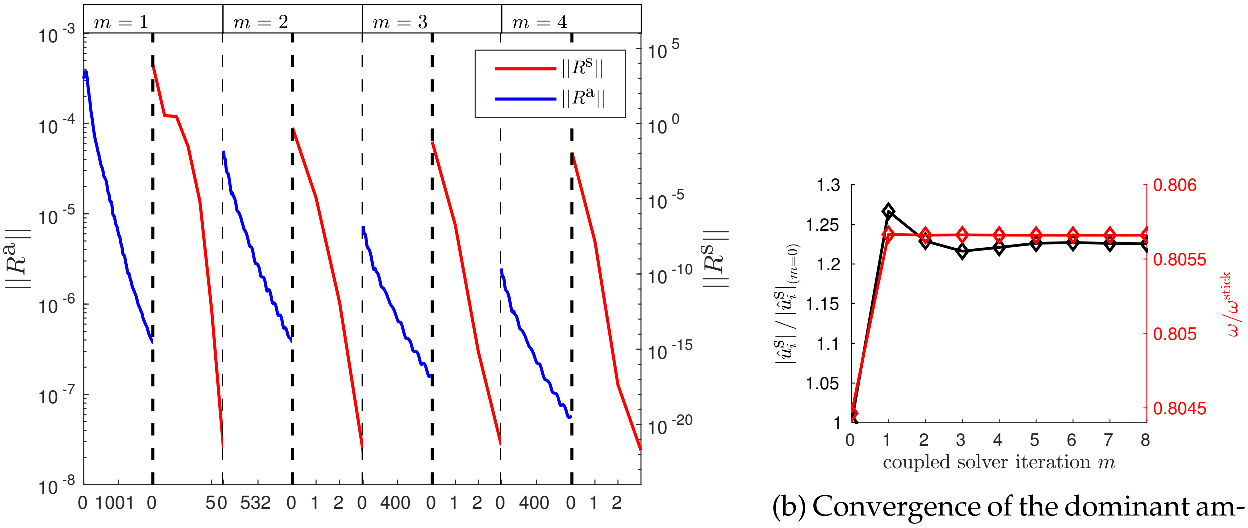

(a) Successive decay of the residuals in fluid and structural domain

(b) Convergence of the dominant amplitude and frequency of the limit cycle

Figure 5.9: Convergence of the FD-FSI solver, configuration 2

cores. This sums up to 110.25 hours on 9 cores. For the linear interpolation with respect to frequency, $\boldsymbol{G}$ must be computed for two frequencies, which doubles the computational effort. The advantage of this approach is that one obtains a closed-form expression for the aerodynamic forces, which can be useful to analyze the aerodynamic damping (and stiffness) for a large number of different vibrational deflection shapes and frequencies (in the considered frequency range). An alternative to this approach is to directly compute the aerodynamic forces for a given structural vibration, and to determine the resulting aerodynamic damping. The effort for such a computation is about the same as that for computing a single column of $\boldsymbol{G}$. Thus, this alternative becomes computationally more attractive than using the influence coefficient matrix once the number of amplitude levels for which ΔW^{a} is of interest falls below the number of generalized coordinates (or twice this number in the case of the two-point interpolation with respect to frequency).

6 Numerical LPT Rotor Testcase with Span-to-Chord Ratio of 6

6.1 Test Case and Modeling

A state-of-the-art aero-elastic model of a low pressure turbine bladed disk (60 blades) with interlocked shrouds (**Figure 6.1**) is considered. The illustration shows the suction side and the pressure side of the blade together with a modeshape (5 nodal diameters (ND)) of the fully assembled disk. The geometry was kindly provided by MTU Aero Engines. The blade has a high span-to-chord ratio of 6, which makes it prone to flutter due to the relatively low reduced frequency.

6.1.1 Structure Model

The mechanical solid is spatially discretized using finite elements. Contact is defined at the area of the tip shrouds indicated in **Figure 6.1**. Within this relatively small area, a homogeneous initial pressure distribution is specified. Planar friction under constant normal loading is considered. Dry stick-slip friction is modeled by the elastic Coulomb law in the same way as in Chapter 5, however with other values (not presented here due to confidentiality). The nonlinear contact surface elements are formulated consistently with the underlying solid elements. The contact interface contains 25 node pairs (conforming meshes). Again, to reduce the mathematical model order, the Craig-Bampton method is applied [12]. Based on the results of a convergence study, the 5 lowest-frequency fixed interface modes were retained in order to achieve a good compromise between accuracy and computational efficiency. A lower amount of fixed interface modes would lead to inconsistent results (regarding modeshape and eigenfrequencies) between the linear eigenvalue analysis of the full model and the reduced order model. A higher amount does not significantly contribute to the accuracy but only increase the computational effort. This yields a total number of 55 generalized coordinates of the structural reduced order sector model.

As in before, mistuning is neglected; i. e., the system is assumed as rotationally periodic, and again, symmetry of the system and its boundary conditions is assumed, which leads to a spatial symmetry of the time-periodic response in the form of a wave traveling around the circumference. Thus only a single sector needs to modeled.

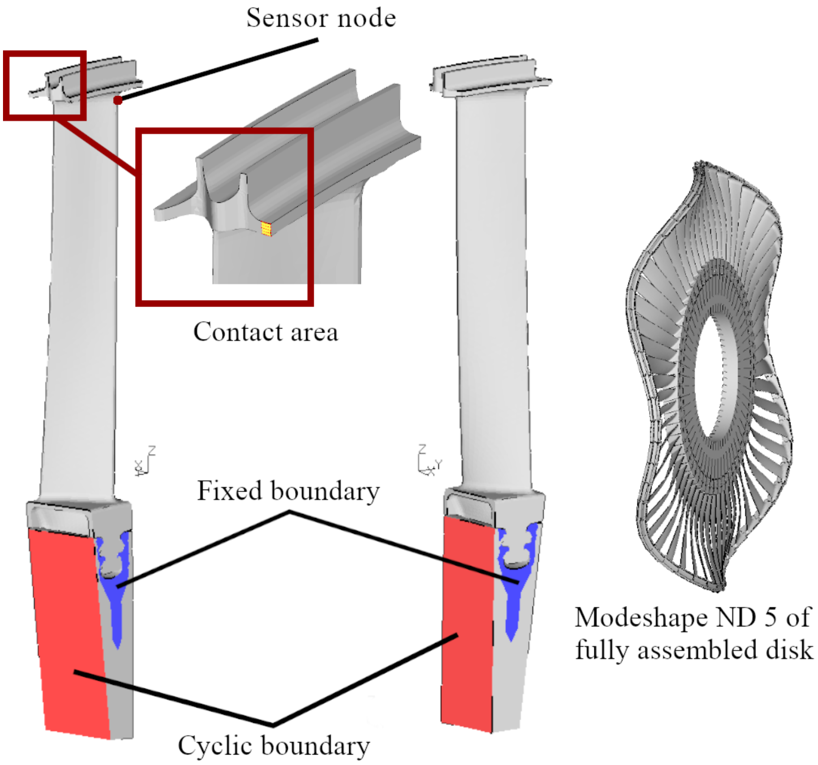

Figure 6.1: Structural model with a detailed view of the contact area (yellow) [C].

6.1.2 Flow Model

In accordance with the assumption of a traveling-wave-type response, only a single passage of the blade row is considered in the flow model. At the cyclic sector boundaries, phase lag boundary conditions are imposed. At the inlet and outlet, 2D non-reflecting boundary conditions are considered [55]. The Mach number at the inlet is 0.33 and the exit 0.75. The Reynolds number with respect to the exit flow conditions and the chord of the blade is 720 000 and the total pressure ratio amounts to 1.02. All values refer to the rotating frame of reference. The compressible unsteady Reynolds-averaged-Navier-Stokes equations are formulated with respect to the conservative variables (density, linear momentum in three directions, energy). The equations are closed with the k-ω turbulence model [69], the ideal gas law and the Sutherland law for the molecular viscosity. The problem domain is discretized with a finite volume mesh containing $N_{\text{cell}} = 476,000$ cells.

6.1.3 Aerodynamic Damping for Sticking and Frictionless Limit Cases

For the two linear limit cases (fully sticking and fully sliding contact conditions), the aerodynamic damping is depicted in **Figure 6.2** for the fundamental mode family as function of the number of nodal diameters (ND). For small nodal diameters, acoustic resonances can be identified. Due to the strong inter-sector coupling, the modal deflection shape

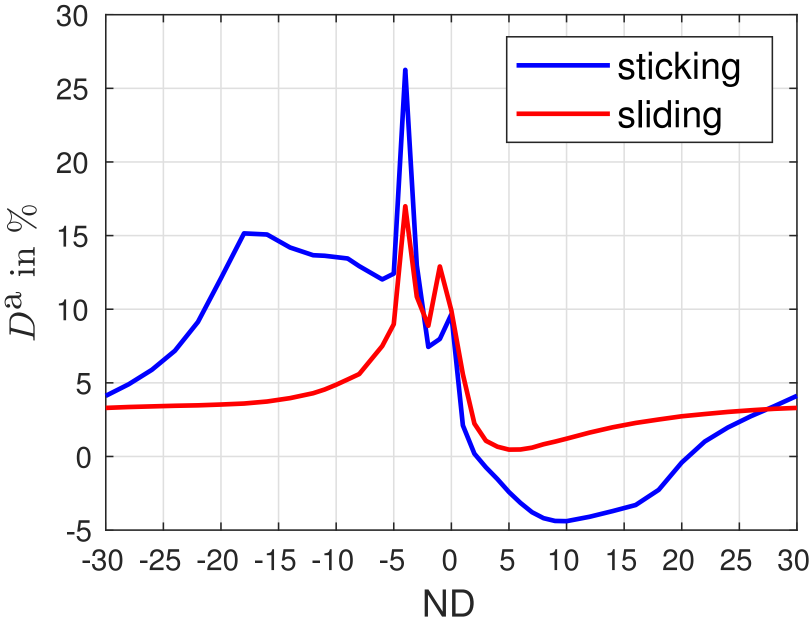

Figure 6.2: Aerodynamic damping of the fundamental mode family for the LPT test case under sticking and frictionless sliding contact conditions at the tip shrouds [C].

and also the natural frequency vary strongly with the ND. In contrast to the test case in Chapter 5, the system is aero-elastically stable for the frictionless sliding case. For sticking contact conditions, the fundamental modes with ND between 2 and 17 are unstable. The flutter intensity (negative aerodynamic damping ratio) amounts to more than 4%. Thus, the aerodynamic influence is relatively strong, but not unrealistic, see e g. the results reported in [11].

It is interesting to discuss what nonlinear behavior can be expected just based on the linear limit cases and the qualitative knowledge of dry friction damping. Suppose, for simplicity, that the structural damping under sticking contact is negligible. Then, clearly, the static equilibrium position is unstable and the vibrations will grow. It is also plausible that there will be a stable limit cycle, as the mode obtained for large vibrations is aeroelastically stable. Moreover, to determine the amplitude level of this LCO a nonlinear analysis is required.

6.1.4 Amplitude Dependence of the Aerodynamic Force

As mentioned before, the test case was designed to have strong aerodynamic influence and, in particular, a severe flutter intensity. The steady flow field of a single passage of the bladerow rotating at 4500 RPM is depicted in **Figure 6.3**. The inlet is located on the left and the x-axis of the coordinate system is aligned with the rotor's axis of rotation. For the given static pressure at the exit, a small shock on the suction side is present. It is therefore interesting to assess the validity of the common linearity assumption of the aerodynamic forces. To this end, the fundamental mode with 5 ND under sticking contact conditions is considered (shape $\boldsymbol{\Psi}$ and frequency ω fixed). The amplitudes cover

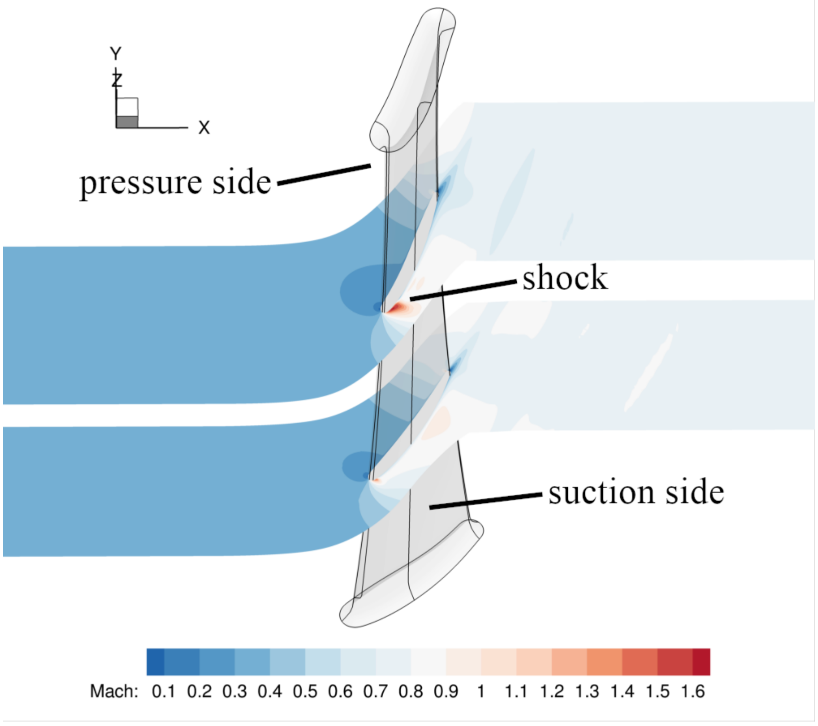

Figure 6.3: Mach contour of the steady flow field at 33 % and 66 % span [C].

the relevant range. In **Figure 6.4(a)** the dependence of magnitude and phase angle of the

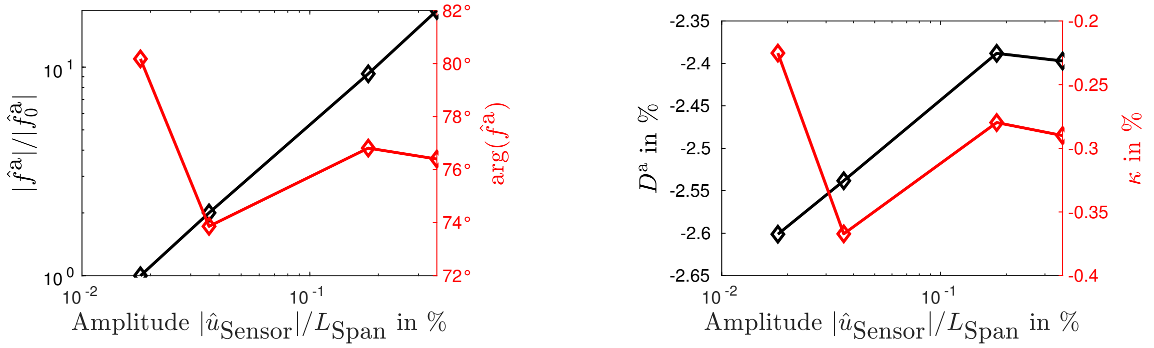

(a) Magnitude and argument of aerodynamic force vs. modal amplitude

(b) Aerodynamic damping and relative frequency shift κ vs. modal amplitude

Figure 6.4: Amplitude dependence of the aerodynamic response (with a linear structure model) [C].

aerodynamic modal force $\hat{f}^{\mathrm{a}}$ are depicted. The modal force is normalized by the respective value for the lowest computed amplitudes. The impact of the aerodynamic force on the linear structure model can also be quantified as damping ratio and relative frequency shift which are shown in **Figure 6.4(b)**. The relative frequency shift κ expresses the change in frequency due to the linearized aerodynamic influence ($\Delta\omega = \kappa\omega$). A distinct but very small nonlinearity with respect to the structural vibration amplitude can be inferred. The influence of the vibration amplitude appears negligible in the light of the influence of the contact boundary conditions which are responsible for a relative frequency shift of $-13\,\%$. Even if there is no significant direct amplitude dependence (for fixed deflection shape and frequency), the nonlinear contact conditions will induce an amplitude dependent natural frequency and deflection shape, which in turn generates an indirect amplitude dependence of the aerodynamic damping and stiffness.

In the following, the focus lies on the fundamental mode with five forward traveling waves around the circumference (ND 5). The modal deflection shape for sticking contact conditions is illustrated in **Figure 6.1**.

6.2 Computation of the LCO via FD-FSI Solver

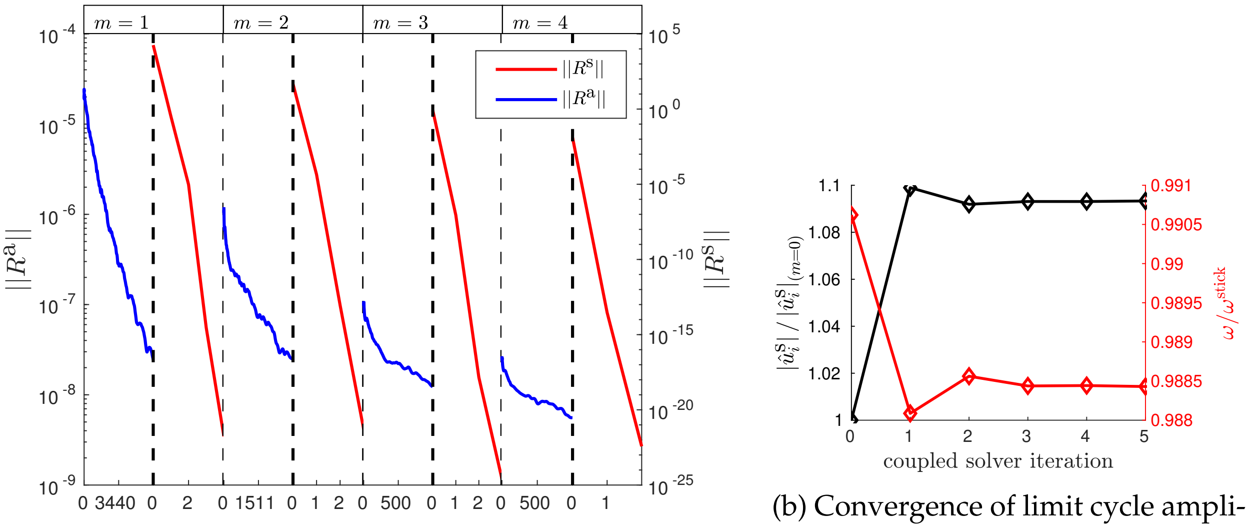

(a) Successive decay of the residuals in fluid and structural domain

(b) Convergence of limit cycle amplitude and frequency (index i refers to dominant fixed-interface mode [C]

Figure 6.5: Convergence of the FD-FSI solver

First, the arising LCO is computed by the FD-FSI solver. **Figure 6.5(a)** and **Figure 6.5(b)** show the convergence behavior of the FD-FSI solver. The residuals in each domain decrease with rates typical for the decoupled subproblems. Thus, the Newton-like solver in the structural domain converges in only a few iterations, while the pseudo time stepping solver in the fluid domain requires a higher amount of iterations/steps. The robustness of the coupled solver is further increased by setting a minimum pseudo time step count for the fluid solver for each iteration (in this case 1000 pseudo time steps). It can be noticed that the necessary pseudo time steps per iteration of the fluid solver decrease with subsequent coupled solver iterations. As expected, the norm of the residual jumps from an iteration of the coupled solver to the next, because the conditions in the respective other domain have changed. The aero-elastic response stabilizes after about 4 outer iterations of the coupled algorithm (**Figure 6.5(b)**). The convergence behavior is quite robust, in spite of the severe aerodynamic influence.

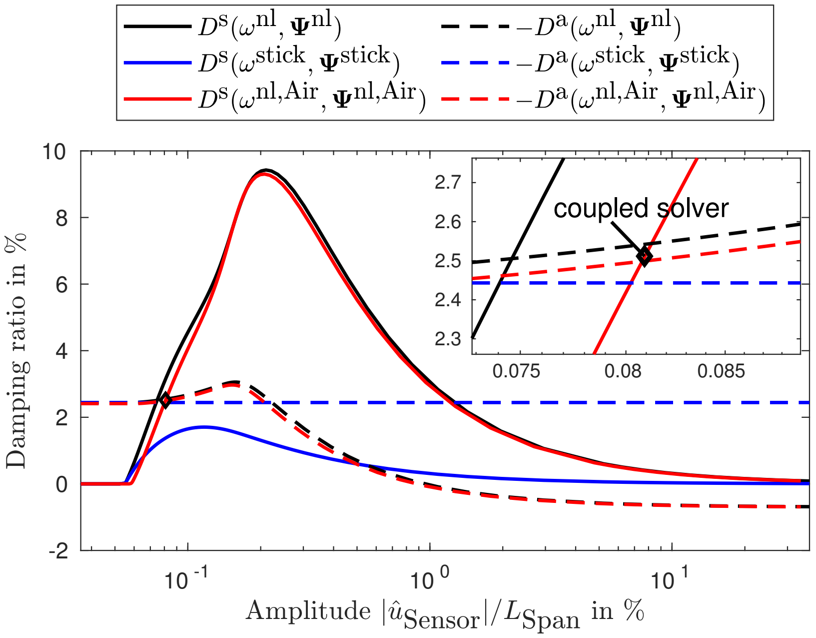

Figure 6.6: Refined Energy Methods and the solution of the coupled FSI solver [C].

6.3 Comparison of the Results Obtained by Energy Methods and FD-FSI Solver

The negative aerodynamic damping ratio (or flutter intensity), $-D^{\mathrm{a}}$, and the positive structural damping ratio, D^{s}, are depicted in **Figure 6.6** as function of the vibration amplitude. Recall that a limit cycle requires $D^{\mathrm{s}} + D^{\mathrm{a}} = 0$. Hence, a limit cycle occurs at the intersections in **Figure 6.6**, where $D^{\mathrm{s}} = -D^{\mathrm{a}}$. The vibration amplitude is measured as the axial displacement at the sensor node indicated in **Figure 6.1**, normalized by the blade span at the leading edge. The results are depicted for three different variants of the energy method:

(a) assuming natural frequency ω^{stick} and mode shape $\boldsymbol{\Psi}^{\mathrm{stick}}$ obtained for linearized contact conditions and in vacuum,

(b) assuming natural frequency ω^{nl} and mode shape $\boldsymbol{\Psi}^{\mathrm{nl}}$ obtained for nonlinear contact conditions in vacuum, and

(c) assuming natural frequency $\omega^{\mathrm{nl,air}}$ and mode shape $\boldsymbol{\Psi}^{\mathrm{nl,air}}$ obtained for nonlinear contact conditions and under linearized aerodynamic influence (REM in air, see Section 4.1.2).

The qualitative dependence of the frictional damping is as expected: For sufficiently small vibrations, the contact is always sticking, so that no frictional dissipation occurs and, thus, $D^{\mathrm{s}} = 0$. For very large vibrations, the bounded dry friction forces become negligible compared to elastic and inertia forces, so that $D^{\mathrm{s}} \to 0$ asymptotically as the vibration amplitude goes to infinity. In between, the frictional damping ratio attains a maximum value. Apparently, the (conventional) energy method (assuming sticking mode shape) strongly underestimates the friction damping. In this case, the flutter intensity is always larger than the structural damping. As a consequence, the (conventional) energy method predicts unbounded growth of the flutter-induced vibrations (no limit cycle).

For the Refined Energy Methods (REMs), which account for the nonlinear dynamic contact interactions, a single limit cycle occurs. In the neighborhood of the limit cycle amplitude, the friction damping increases more quickly than the flutter intensity. Hence, the limit cycle is stable, at least from an energy balance point of view. Remarkably, no further limit cycle occurs. The picture changes completely if the effect of the nonlinear contact boundary conditions on the aerodynamic damping is neglected. In that case, the aerodynamic damping ratio is constant. Hence, another intersection with the friction damping curve would occur at larger vibration levels (here at an amplitude of about 1.3 % span). This intersection would correspond to an unstable limit cycle (stability limit). This means that for sufficiently large external perturbation, the friction forces would not be able to saturate the flutter-induced vibrations. Consequently, the effect of the nonlinear contact boundary conditions on natural frequency and mode shape must be considered, both in the evaluation of the friction damping and in the aerodynamic damping, in order to predict the correct qualitative behavior.

	CEM	REM	REM in air
Frequency	-	$-0.035\,\%$	$-0.011\,\%$
Amplitude	-	8.43 %	0.13 %

Table 6.1: Relative deviation between the energy methods and the FD-FSI solver with regard to limit cycle amplitude and frequency; CEM: conventional energy method, REM: refined energy method [C].

The two REMs show a significant quantitative difference, depending on whether the nonlinear mode is computed with or without aerodynamic influence. Interestingly, the difference is particularly prominent for the friction damping. Note that the friction damping is relatively sensitive in the relevant amplitude range. Thus, even a moderate aerodynamic stiffness has a significant effect on the nonlinear modal properties. When the aerodynamic influence is taken into account, the REM shows very good agreement with the FD-FSI solver. It should be noted that the FD-FSI solver was initialized with the result obtained from the REM in vacuum. The relative deviations of limit cycle amplitude and frequency are also listed in **Table 6.1**. The REM in vacuum underestimates the limit cycle amplitude by about 10 %.

To gain further physical insight in the aerodynamic damping behavior, the influence of the modeshape and frequency on the aerodynamic damping is investigated. For this, the same analysis as in Section 5.4.2 is carried out: the aerodynamic damping is evaluated with either the modeshape $\boldsymbol{\Psi}$ or the frequency ω set equal to the values for sticking contact conditions (constant for all amplitudes). The outcome is shown in **Figure 6.7**. For the investigated testcase the influence of the modeshape plays a major role regarding the aerodynamic damping while the influence of the frequency is not as severe.

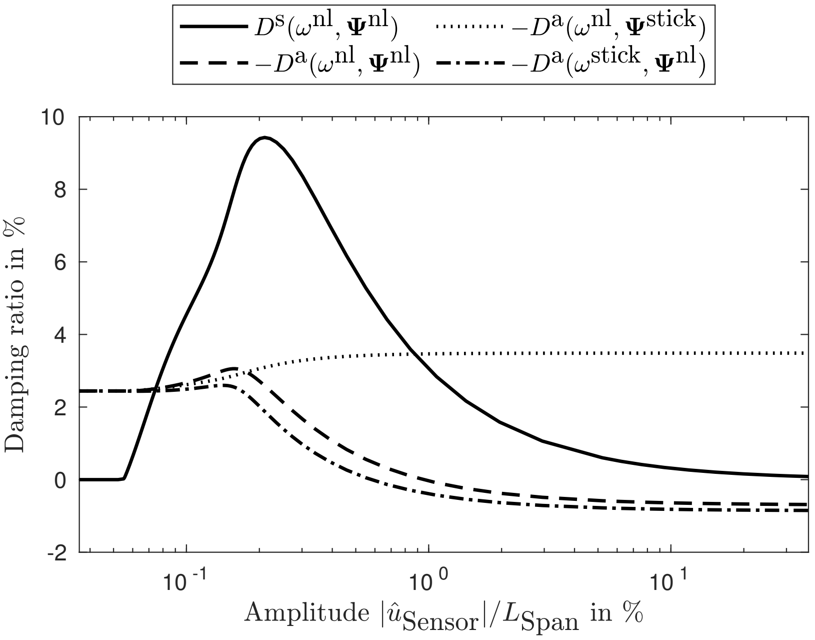

Figure 6.7: Influence of the modeshape and frequency on the aerodynamic damping [C].

6.4 Discussion of the Computational Effort

The computational effort for the REMs is dominated by the computation of the aerodynamic influence coefficient matrix $\boldsymbol{G}(\omega)$. As described before, the matrix is computed column-wise, and for two different oscillation frequencies. For the 55 component modes considered in this study, this requires 110 computational fluid dynamics simulations. In each simulation, a harmonic structural deformation in the form of a component mode is imposed, and the vibration-induced generalized forces are determined. In average, such a simulation takes about 5 hours on 24 cores. Hence, the computation of $\boldsymbol{G}(\omega)$ required a total simulation effort of 550 hours on 24 cores. For comparison, the FD-FSI solver required only 10 hours on 24 cores for the first 4 iterations beyond which the results are deemed stabilized. However, as explained before, the matrix $\boldsymbol{G}(\omega)$ was used in order to construct an initial guess for the FD-FSI solver. From these results, one can derive two interesting perspectives to simplify the construction of the initial guess in future work: (a) one could attempt to compute not every single column of $\boldsymbol{G}(\omega)$ but only those associated with component modes strongly participating in the nonlinear vibration, (b) one could use the REM in vacuum and compute the aerodynamic damping only for a set of amplitudes (rather than relying on the matrix $\boldsymbol{G}(\omega)$ as in this study).

6.5 Harmonic Convergence Analysis

The previously presented results of the coupled solver were computed with one fundamental harmonic for the structural solver ($H^{\mathrm{s}} = 1$) and two harmonics for the flow solver ($H^{\mathrm{a}} = 2$). In **Figure 6.8** the behavior of the coupled solver results under a varying number

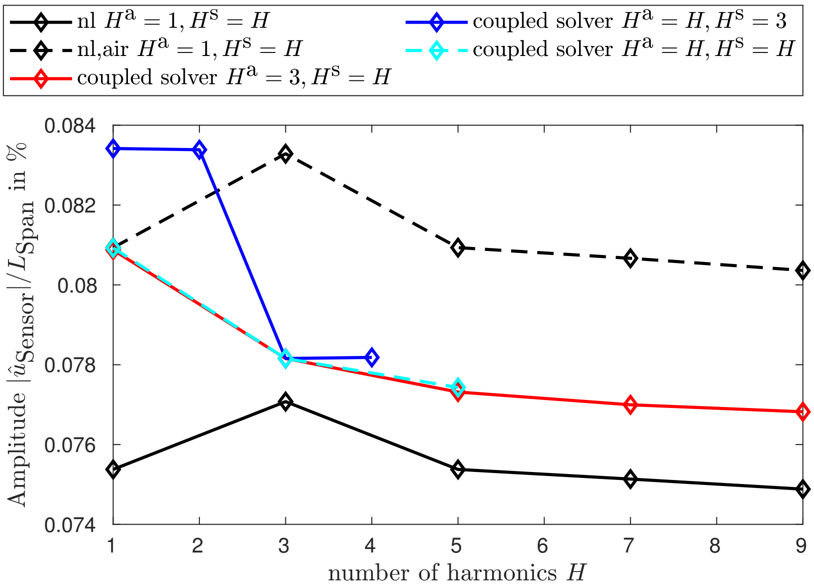

Figure 6.8: Harmonic convergence of the coupled solver and the REM [C].

of harmonics H in both domains is shown. Two graphs are plotted with either the number of structural or flow harmonics kept constant to 3 ($H^{a} = 3$, $H^{s} = H$) and ($H^{a} = H$, $H^{s} = 3$). In the third variant ($H^{a} = H$, $H^{s} = H$) equally many harmonics in both domains are used which yields the most accurate results with the lowest harmonic truncation error (but also comes with the highest computational costs). The outcome of the REMs (nl and nl, air) are also depicted in the same figure. From the results of the coupled solver with ($H^{a} = 3$, $H^{s} = H$) and the REMs it can be observed that for this test case $H^{s} \geq 7$ should be used to achieve harmonic convergence in the structural domain. From the simulations with varying number of fluid harmonics ($H^{a} = H$, $H^{s} = 3$) a sudden drop between $H^{a} = 2$ and $H^{a} = 3$ is observed. This can be explained with a strong interaction between the third harmonics of both domains which in the case of $H^{a} \leq 2$ cannot take place. The fact that the coupled solver result with $H^{a} = 3$ and $H^{s} = 5$ is very similar to the one with $H^{a} = 5$ and $H^{s} = 5$ shows that the interaction between the fifth harmonics of both domains is not as severe as for the third harmonics.

All coupled solver results which are computed with one harmonic in both domains $H^{a} = 1$, $H^{s} = 1$ match the outcome of the corresponding REM in air result (nl, air $H^{a} = 1$, $H^{s} = 1$). Furthermore the REM in air result (nl, air $H^{a} = 1$, $H^{s} = 3$) agrees with the coupled solver result ($H^{a} = 1$, $H^{s} = 3$). Both observations confirm the consistency between the coupled solver and the REM in air approach. Note that the only difference of both approaches lies in the modeling of the aerodynamic forces (influence coefficients vs. direct computation, see discussion after Eq. (2.41)). It can thus be concluded that the linear interpolation according to Eq. (4.4) is accurate. The results obtained by the REM in vacuum do not directly correspond to any of the other results which comes with no surprise since it is the only method with only a one-way coupling approach.

It is emphasized that the qualitative differences in the results of the energy methods and the FD-FSI solver as discussed in the previous sections are still present in all cases where an increased amount of harmonics are used. Thus the qualitative behavior of the coupled system can be captured with a relatively low number of harmonics in both domains. An increased amount of harmonics is only necessary if highly accurate results are desired. The most expensive simulations are the ones with a high amount of fluid harmonics. An increase in the amount of structural harmonics does not impact the computational effort significantly due to the low amount of unknowns in the structural solver compared to the fluid solver.

In **Figure 6.9** the convergence of the coupled solver with $H^{\mathrm{a}} = 5$ and $H^{\mathrm{s}} = 5$ is illustrated. In the case with $H^{\mathrm{a}} = 2$ and $H^{\mathrm{s}} = 1$, convergence is achieved after about 5 coupled solver iterations.

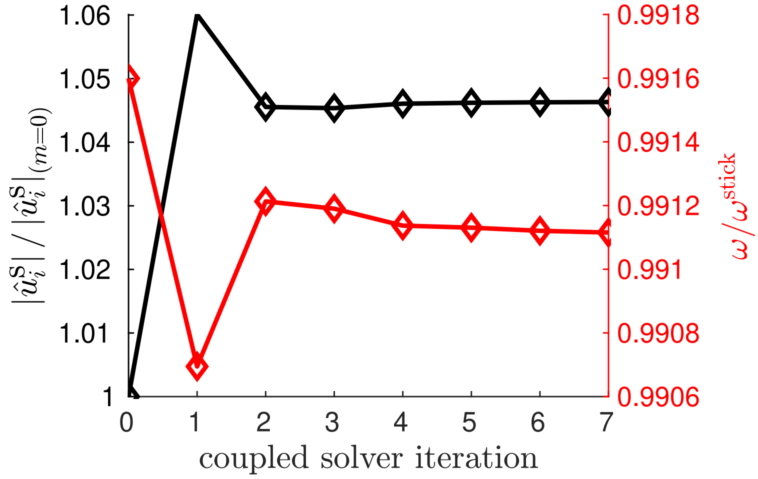

Figure 6.9: Convergence of limit cycle amplitude and frequency for $H^{\mathrm{a}} = 5$ and $H^{\mathrm{s}} = 5$ [C].

7 Verification of Nonlinear Frequency Domain Methods with Time Domain Simulations

For a successful numerical validation, a consistent modeling for both methodologies (coupled frequency and time domain solvers) is essential. Hence, the modeling approach presented in the following two sections applies to both domains. Subsequently, time-domain and frequency-domain specific topics addressed and finally the simulation results are presented.

7.1 Structure Model

For the structural model, the same configuration as in Chapter 6 is used. One sector of the rotationally periodic structure of 60 sectors is illustrated in **Figure 6.1**. In a preprocessing step a static equilibrium under centrifugal loading due to the rotation speed is computed. This static equilibrium serves as a reference configuration for the following dynamic force balance:

$$\boldsymbol{M}_{\mathrm{FE}}\ddot{\boldsymbol{q}}_{\mathrm{FE}} + \boldsymbol{K}_{\mathrm{FE}}\boldsymbol{q}_{\mathrm{FE}} + \boldsymbol{f}^{\mathrm{c}}_{\mathrm{FE}} = \boldsymbol{f}^{\mathrm{a}}_{\mathrm{FE}}. \tag{7.1}$$

For now the FE model of the full bladed disk is considered. The sparse, symmetric and positive definite matrices $\boldsymbol{M}_{\mathrm{FE}}$ and $\boldsymbol{K}_{\mathrm{FE}}$ are the mass and the stiffness matrix respectively and $\boldsymbol{q}_{\mathrm{FE}}$ denotes the FE nodal displacement coordinates (counted from the static equilibrium). The elastic forces are linearized which implies a linear material behavior and linear kinematics and thus the model is only suitable for small vibrations. In the current model the blades are rigidly attached to the disk (no nonlinear contact interactions).

In the contact area (marked yellow in **Figure 6.1**) the normal relative displacement is constrained (separation of the contact surfaces is neglected). Similar to the last two test cases, spatial dry friction is modeled using coupled 2-dimensional elastic Coulomb dry friction elements with a constant normal load [36, 70], which have a hysteretic force-displacement relationship. One contact element connects each of the 25 pairs of cyclically matching nodes on either side of the contact interface.

To reduce the mathematical order of the structural model, it is common practice to use component mode synthesis techniques such as the Craig-Bampton method [12], as is done in the last two chapters. It is well-known that these techniques lead to a relatively high numerical stiffness so that extremely small time steps are needed, which would have made the application of the TD-FSI solvers practically impossible or at least very challenging,

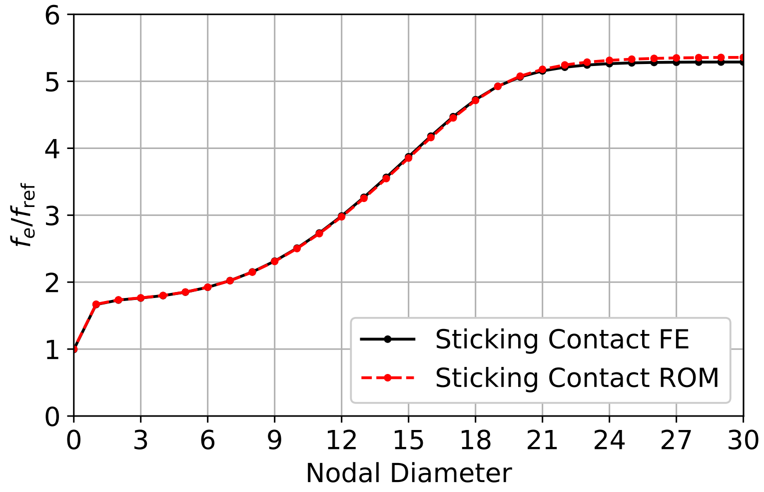

Figure 7.1: Lowest eigenfrequency of the linearized structure (FE model and ROM) for each nodal diameter (ND) [F].

which however is out of scope for this work. To overcome this, conventional modal truncation is used. More specifically, the motion is approximated with the 10 lowest-frequency mode families. The normal modes are computed neglecting the aerodynamic forces and the friction forces (frictionless sliding contact conditions).

The strict truncation to only 10 mode families leads to a poor representation of the static compliance with respect to loads applied at the contact interface. To compensate for that effect to some extent, a relatively low contact stiffness is selected. The resulting natural frequencies under sticking contact conditions are in good agreement with those of the FE model, see **Figure 7.1**. Note that for the linear extreme case of frictionless sliding, the natural frequencies and mode shapes are represented as accurately as in the FE model (due to the chosen modal ROM). For confidentiality, only normalized quantities are reported. As in **Figure 7.1**, frequencies will be scaled by $f_{\mathrm{ref}} = f_e(\mathrm{ND} = 0)$.

7.2 Aerodynamic Model

The fluid is modeled with the compressible unsteady Reynolds-averaged Navier-Stokes (URANS) equations. Ideal gas is assumed and a $k - \omega$ turbulence model [69] is used. For the spatial discretization of the fluid domain 862,848 finite volume cells for a single sector are used and 60 times that (51×10^6 cells) for the full blade row with a second order Fromm scheme and a slope limiter in order to prevent numerical instability. At the inlet and exit of the fluid domain, NRBCs are imposed. 2-dimensional spectral NRBCs are commonly used because they provide high accuracy, but they require the fundamental oscillation frequency which is not available in the TD-FSI approach. To keep the modeling consistent among time and frequency domain, 1-dimensional fluid NRBCs [30] are imposed. In **Figure 7.2** the Mach number contour at a channel height of 85% is shown.

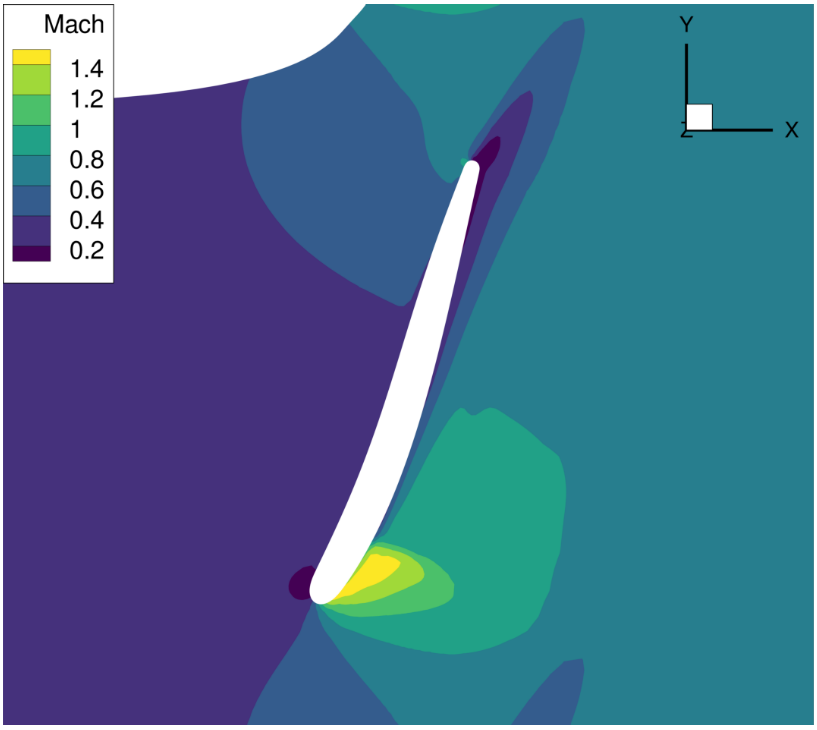

Figure 7.2: Mach number contour at 85% channel height [F].

The total pressure ratio amounts to 1.16 (in the absolute frame of reference). By prescribing a relatively low static pressure at the exit a transonic point of operation with a shock on the suction side is achieved, which leads to an increased fluid velocity and thus to a low reduced frequency [62]. A low exit pressure also increases the aerodynamic blade loading (the mean net force acting on the blade). The low reduced frequency and the high aerodynamic blade loading leads to a strong aerodynamic excitation of the blade row.

The flutter curve is presented in **Figure 7.3** which shows the aerodynamic damping ratio D_a as function of the nodal diameter (ND) for the linearized structure model (with sticking contact conditions in the shroud). It can be observed that blade vibrations are aerodynamically unstable for travelling wave modes with ND between 3 and 19.

Analogous to the comparison of the eigenfrequencies of the linearized structure (sticking contact conditions) in **Figure 7.1** also the aerodynamic damping ratio D_a is evaluated for the FE model and the ROM and plotted in **Figure 7.3**. The good agreement shows that the aerodynamic behavior is surprisingly well described for this linear limit case in spite of the relatively simple structural ROM.

Due to the nonlinear flow features, D_a depends on the vibration amplitude (even for fixed deflection shape and frequency). This explicit amplitude dependence was investigated and found to be relatively small: For the largest amplitude obtained in the numerical examples, D_a varies not more than 8 % compared to its asymptotic value for vanishing amplitudes.

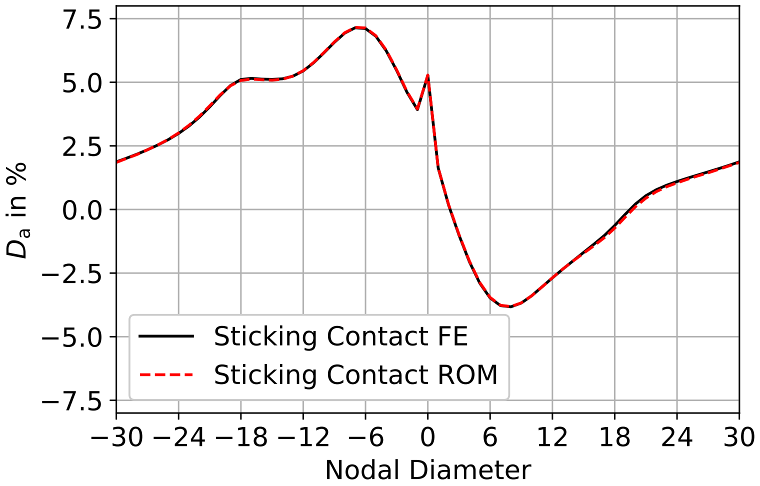

Figure 7.3: Fluttercurve of the linearized structure (FE model and ROM) for the first mode [F].

7.3 TD-FSI Solver

In the time step integration approach, the coupled problem is solved using a sequential fixed-point algorithm as described and illustrated in Section 2.8.6. For each time step, coupled iterations are performed until convergence is achieved according to a specified tolerance. Throughout this work, it was found that at most 3 coupling iterations are needed, and for simplicity, a fixed number of 3 coupling iterations was therefore used.

The time integration schemes used for the fluid solver is the second-order Backward Differencing Formula (BDF2) in conjunction with a pseudo-time stepping scheme. On the structure side, the average constant acceleration (second-order) Newmark scheme is used. Here, the arising nonlinear algebraic equations are solved with a predictor-corrector method.

During the analysis, the slope limiter was found to produce a numerical artefact that had to be compensated. The slope limiter is needed to avoid unphysical spatial oscillations in the fluid variables. To achieve affordable computational effort, a simplified formulation of the slope limiter is used in the fluid solver, which is not rotation-invariant [16]. This was observed to cause a small but noticeable static pressure field perturbation and corresponding structural forcing. Interestingly, the form of this distortion is rotationally periodic with 4 repetitions around the circumference. This symmetry is related to the fact that the fluid volume is meshed with hexahedral elements which essentially have three 4-fold rotation axes. The distortion induced by the rotational variance of the slope limiter should be compensated. To this end, it is assumed that the vibration-induced variation of the flow field is small compared to the steady (mean) flow field. Then the modal aerodynamic force is computed in a steady fluid analysis (for $\boldsymbol{u}^{\mathrm{s}} = \boldsymbol{0}$), $\boldsymbol{f}^{\mathrm{a}}_{\mathrm{limiter}} = \boldsymbol{f}^{\mathrm{a}}(\boldsymbol{u}^{\mathrm{a}}_{\mathrm{steady}})$, which is then subtracted from $\boldsymbol{f}^{\mathrm{a}}$ in the coupled analysis. The results without and with the proposed compensation are compared, and it is found that indeed the static distortion of ND 4 form does not occur anymore (to machine precision).

A further simplification was introduced to achieve reasonable computational efficiency: The coupling of the 0-th spatial harmonic between fluid and structure was neglected. The 0-th spatial harmonic represents the circumferential mean value and is typically associated with the temporal mean value. Thus, a change of the 0-th harmonic corresponds to a change of the aerodynamic operating point. While the vibration-induced change of the operating point might be an interesting investigation itself, it is considered to be beyond the scope of the present study. Furthermore, the (TD-FSI) simulation time would increase further due to a longer transient of low frequency (ND 0) modes. To avoid the coupling of the 0-th harmonic, the modal deflection of the corresponding (ND0/umbrella) modes is not accounted for in the mesh deformation within the fluid domain. Analogously, the modal forcing of the corresponding modes due to the fluid field is ignored. It should be emphasized that these simplifications affect only the coupling, whereas the 0-th harmonic is still considered (and may thus assume non-zero values) in the respective domain.

7.4 Temporal Resolution

For the fluid HB solver the number of sampling points used for the evaluation of the nonlinear terms with the AFT scheme is $4 \cdot H^{\mathrm{a}} + 1$, which is above Orszag's suggestion [48]. Since some terms of the compressible URANS are rational functions of the conservative flow variables, errors of third order due to aliasing may still occur [21]. The above rule however proved to be sufficiently accurate for turbomachinery applications. In case of the structural HB solver a fixed amount of 512 sampling points for the treatment of the nonlinear terms is used, for all considered H^{s}. This was found to be sufficient to obtain converged results (with respect to the number of sampling points).
In the time domain solvers, a fixed time step size is used. For reasonable resolution of the stick-slip transitions, each time step of the TD-FSI solver is subdivided into 8 increments for the structural solver. For the increments, $\boldsymbol{f}^{\mathrm{a}}$ is linearly interpolated between $\boldsymbol{f}_i^{\mathrm{a}}$ and $\boldsymbol{f}_{i+1}^{\mathrm{a}}$. It was ensured that the depicted results do not change significantly upon further time step refinement. For the example of the LCO8 (see next section), this led to 76 time steps per period for the fluid TD solver (vs. 33 for the FD solver) and 610 steps per period for the structural TD solver (vs. 512 for the FD solver).

7.5 Limitations of TD-FSI and FD-FSI Solvers

The TD-FSI approach solves an initial value problem using conventional forward time step integration. Consequently, only asymptotically stable limit states can be reached. The spatial symmetry (ND contributions) and the type of limit state (fixed point, periodic, quasi-periodic, chaotic) are not a priori known and depend on the initial value. In contrast, the FD-FSI approach solves a periodic boundary value problem (in time and in space) and is limited to traveling-wave type oscillations. The limit state is thus a priori periodic and the associated fundamental spatial wave number has to be specified. Generalizations to quasi-periodic limit states are possible but the current version of the FD-FSI solver is limited to the periodic case. The computed limit state is not necessarily asymptotically stable, so additional knowledge is needed to filter out physically realizable from non-realizable solutions. However, the ability to compute unstable limit states can be important to obtain a more complete picture of the dynamic behavior including the definition of stability limits (as shown in Chapter 5).

Recall that for the considered (first) mode family, travelling wave modes with ND in the range between 3 and 19 are aerodynamically excited (negative damping). According to [43, 10], each unstable traveling-wave mode is associated with a certain LCO dominated by the corresponding ND. The basin of attraction, i.e., the range of initial conditions that lead to a certain LCO, tends to be larger, the more negative the aerodynamic damping. Rather recently, it was found that the LCOs corresponding to the barely negative NDs tend to be not asymptotically stable [23]. The flutter-induced vibrations are initialized with three different NDs, namely ND 3 (barely unstable), ND 8 (most unstable), and ND 14 (moderately unstable). Also, other NDs are studied, but it is found that these cases are representative. Notice that the space of sensible initial conditions for the TD-FSI solver is very large since also combinations of initially perturbed NDs are contained, however, only single NDs are perturbed which are likely to result in the LCOs of interest.

In the TD-FSI simulations, the initialization is done by imposing initial modal displacements and velocities for the whole bladed disk in the form of the given traveling-wave mode (linearized for sticking contact conditions). In the FD-FSI simulations, a nonlinear modal analysis is first carried out under in-vacuum conditions (aerodynamic forces neglected) as proposed in [C]. This yields amplitude-dependent structural damping, modal frequency and deflection shape for the given traveling-wave mode. The amplitude at which (positive) structural and (negative) aerodynamic damping cancel is then selected and the corresponding periodic vibration is provided as initial guess to the coupled FD-FSI solver.

As shown in the following, the initialization with ND 8 and ND 14 leads to corresponding limit cycles, which are denoted as LCO8 and LCO14, respectively. In contrast, the initialization with ND 3 yields a limit torus with dominating wave numbers 12, 14, 16 which is denoted as LTO12-14-16. Results obtained by the TD-FSI solver / FD-FSI solver are denoted by 'TD' / 'FD', respectively, in the legends. For the FD-FSI solver, the harmonic truncation orders in the fluid domain (H^{a}) and in the structural domain (H^{s}) are also indicated.

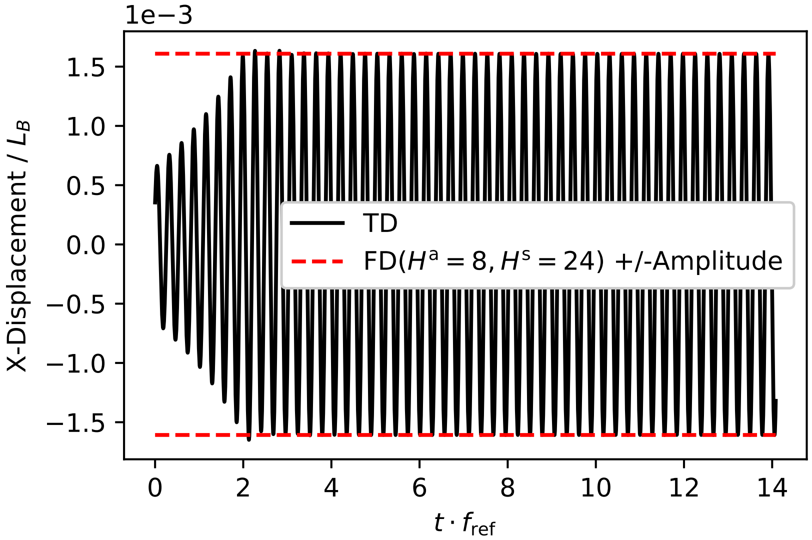

Figure 7.4: X-Displacement over time at sensor node for LCO14 [F].

7.6 LCO14

For the TD-FSI simulation the initial amplitude lies in the regime of sticking contact conditions. Consequently, the vibrations increase at first, until they saturate in a limit cycle here (**Figure 7.4**). The depicted response is the displacement of the sensor node in X-direction (see **Figure 6.1**), normalized by the blade length L_B. As discussed above, the aerodynamic forces were found to be almost linear in the vibration amplitude (in the relevant amplitude range). Thus, the nonlinear saturation of the self-excited vibrations is primarily due to nonlinear structural forces, namely dry frictional dissipation. The transient TD-FSI solution confirms the asymptotic stability of LCO14. The limit cycle amplitudes predicted by TD- and FD-FSI solvers are in very good agreement.

To analyze the spectral content of LCO14, a two-dimensional discrete Fourier transform in time and in space (along the blades in the blade row) is carried out. The results are depicted in **Figure 7.6(a)**, where the amplitudes are illustrated in logarithmic color scale. One can see that the fundamental frequency component is dominated by ND 14. Odd higher temporal harmonics appear which is typical for dry friction nonlinearity with constant normal load. Due to the traveling-wave character of the vibration, the associated spatial harmonics (NDs) are also odd integer multiples of the fundamental ND 14, but due to the finite blade count, aliasing occurs. For instance, the ND corresponding to the third harmonic is $3 \cdot 14 = 42 \mathrel{\hat{=}} (42 + 30) \bmod 60 - 30 = -18$. The modulus operation and the $+30$ and -30 ensure that the resulting ND is in the conventional range $[-N_{\mathrm{Blades}}/2, +N_{\mathrm{Blades}}/2]$. Consequently, the spot in **Figure 7.6(a)** at (ND $-18, 3f_0$) corresponds to the third harmonic of LCO14.

As expected, the results of the FD-FSI solver successively approach those of the TD-FSI solver with increasing harmonic truncation order. This can be seen for the phase projections of the limit cycle in **Figure 7.5(a)**. Here, the normalized X-, Y- and Z-displacements of the sensor node are depicted. Due to the simplified treatment of the coupling with

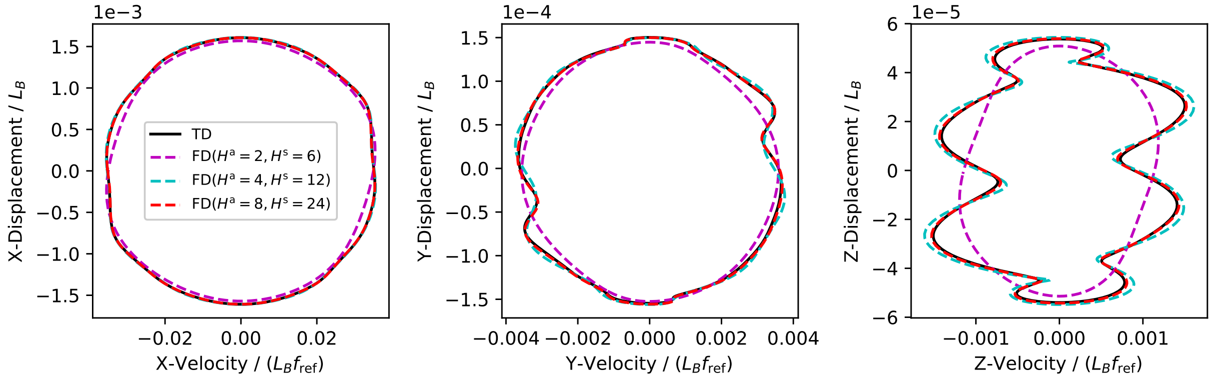

(a) Phase diagrams of LCO14.

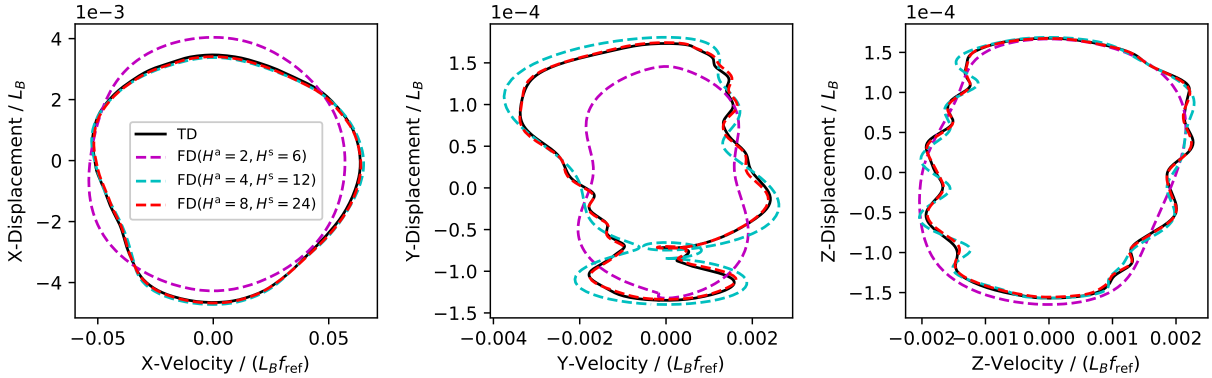

(b) Phase diagrams of LCO8.

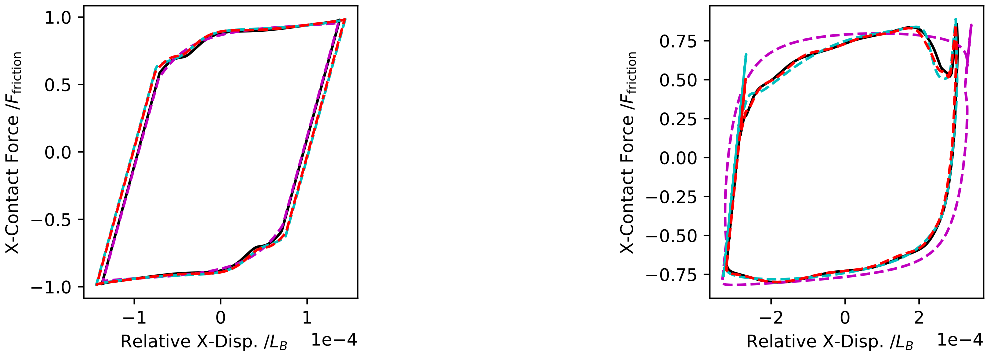

(c) X-contact force hysteresis of contact element 1 for LCO14. (Same legend as in phase diagrams applies.)

(d) X-contact force hysteresis of contact element 1 for LCO8. (Same legend as in phase diagrams applies.))

Figure 7.5: Phase diagrams of sensor node displacement and force-displacement hysteresis plots [F].

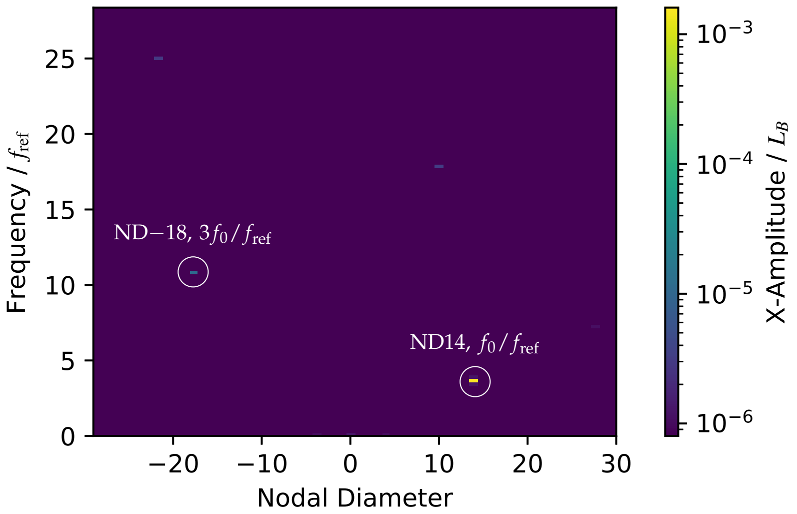

(a) LCO14

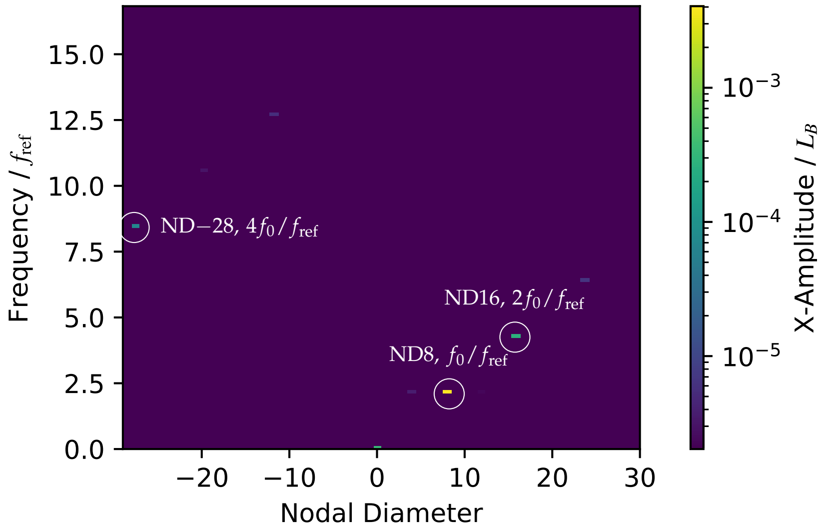

(b) LCO8

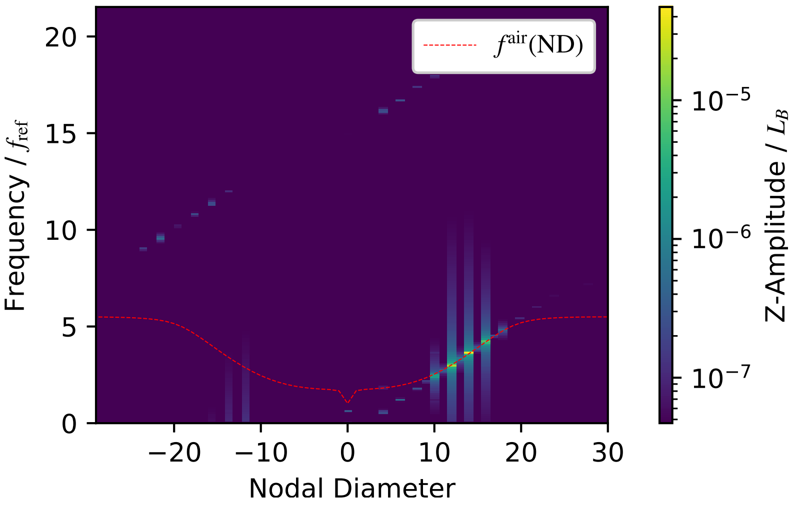

(c) LTO12-14-16

Figure 7.6: 2D-DFT of X-displacement at sensor [F].

regard to the 0-th harmonic, the mean component of the displacement is removed from the TD-FSI result and neglected in the Fourier synthesis of the FD-FSI results. A prominent participation of odd higher harmonics can be ascertained from the phase projections, especially in the Z-direction. Note, however, that the Y- and Z-displacements are 1-2 orders of magnitude smaller than the X-displacements. The good agreement between time and frequency domain results is also reflected in the force-displacement hysteresis (**Figure 7.5(c)**). Here, the contact force in the X-direction is normalized by the limit friction force F_{friction}. Finally, the results also agree with regard to the frequency of the limit cycle: The deviation to the TD-FSI result in terms of fundamental frequency is $-0.37\,\%$ for the $\text{FD}(H^{\text{a}} = 2, H^{\text{s}} = 6)$ and $0.09\,\%$ for the $\text{FD}(H^{\text{a}} = 8, H^{\text{s}} = 24)$ result.

7.7 LCO8

The spectral content of LCO8 has a distinctly different pattern than that of the previously considered LCO14: Even harmonics strongly participate in the vibration, especially the second and the fourth harmonic, cf. **Figure 7.6(b)**. Consequently, the phase projections in **Figure 7.5(b)** and the force-displacement hysteresis in **Figure 7.5(d)** are no longer rotation-symmetric. Before analyzing this peculiar phenomenon, it is remarked that, again, the FD-FSI solver is in excellent agreement with the TD-FSI solver if sufficiently many harmonics are considered. In this case, the fundamental frequency deviation is $-0.09\,\%$ for $\text{FD}(H^{\text{a}} = 2, H^{\text{s}} = 6)$ and $-0.008\,\%$ for $\text{FD}(H^{\text{a}} = 8, H^{\text{s}} = 24)$.

Now, the appearance of even harmonics is analyzed. It is postulated that these are caused in the following way: The negative aerodynamic damping of ND 8 leads to the usual excitation of the fundamental harmonic of the corresponding traveling-wave mode. This vibration induces a fundamental harmonic perturbation in the fluid domain. The subsequent motion of the shock generates even harmonics in the fluid domain. The strong presence of both odd and even harmonics in the fluid domain near the shock is illustrated in **Figure 7.7** in terms of the four pressure harmonics ($\hat{p}_k$, $k = 1, 2, 3, 4$, normalized by the static exit pressure p_e) at 85% channel height. Responsible for the generation of odd and even higher harmonics in the fluid domain is the aerodynamic nonlinearity. These higher harmonics in the conservative variables lead to corresponding higher harmonics in the aerodynamic forcing. Even higher harmonic forcing is also generated in case of the LCO14. However, the structure responds with pronounced even harmonics only in the LCO8 case. This is due to an internal resonance: The ND 8 mode's frequency and the ND 16 mode's frequency are close to a 1:2 ratio (cf. **Figure 7.1**). Such a condition does not hold in the LCO14 case (where the ND 28 mode's frequency is not close to twice the ND 14 mode's frequency). The internal resonance condition opens the door for modal interaction, i.e., nonlinear energy exchange among the corresponding harmonics. The modal interaction is further affected by the negative aerodynamic damping of the ND 16 mode. The strength of the fourth pressure harmonic also explains why at least 4 fluid harmonics are necessary for the FD-FSI solver in order to achieve a reasonable approximation of the

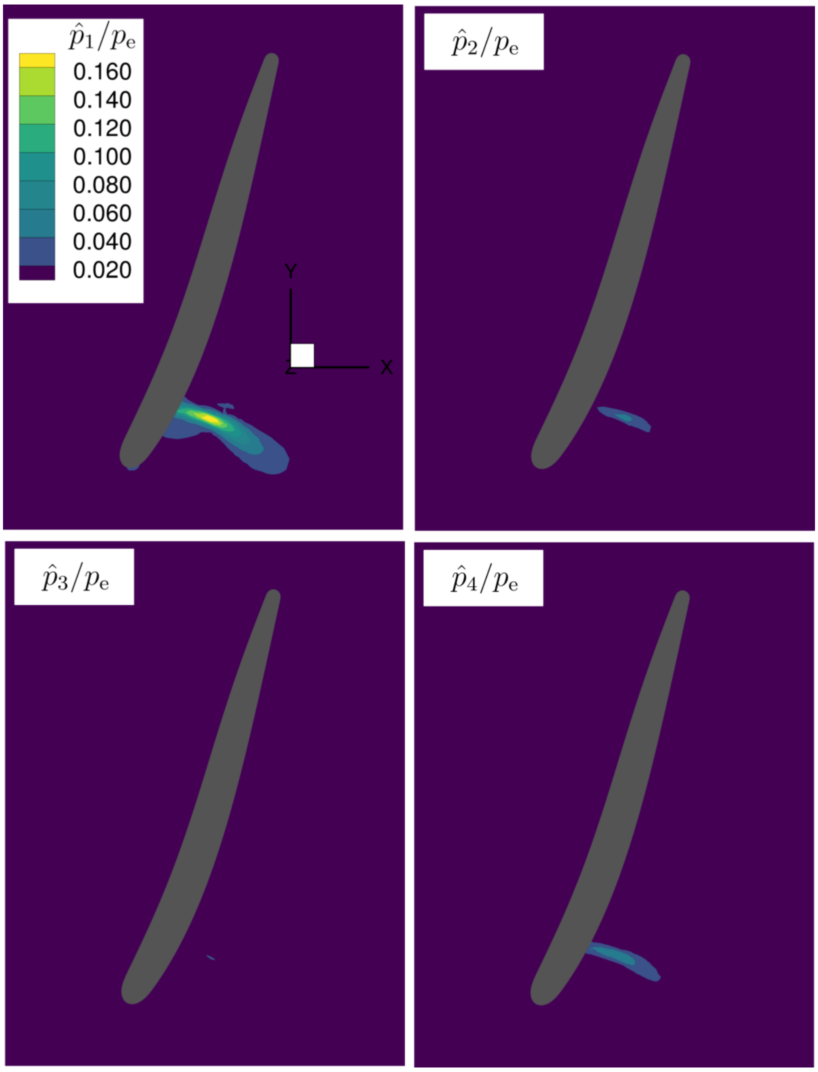

Figure 7.7: Amplitude of pressure harmonics at 85% channel height [F].

LCO.

The nonlinear modal interaction is further analyzed using the FD-FSI solver. More specifically, the work done by the second harmonic of the aerodynamic force (per cycle) is computed for three different cases: $W^{\mathrm{a}}_{\mathrm{cyc},2}(\hat{\boldsymbol{u}}^{\mathrm{s}}_1)$ is the work done by the aerodynamic force, $\hat{\boldsymbol{f}}^{\mathrm{a}}_2(\hat{\boldsymbol{u}}^{\mathrm{s}}_1)$, induced solely by the fundamental harmonic of the blade vibration, $\hat{\boldsymbol{u}}^{\mathrm{s}}_1$. To compute $\hat{\boldsymbol{f}}^{\mathrm{a}}_2(\hat{\boldsymbol{u}}^{\mathrm{s}}_1)$, the blade motion imposed in the fluid solver is restricted to the fundamental harmonic, $\hat{\boldsymbol{u}}^{\mathrm{s}}_1$, while setting all other harmonics to zero, $\hat{\boldsymbol{u}}^{\mathrm{s}}_k = \mathbf{0}$ for all $k \neq 1$. Analogously, $W^{\mathrm{a}}_{\mathrm{cyc},2}(\hat{\boldsymbol{u}}^{\mathrm{s}}_2)$ is the work done by the aerodynamic force, $\hat{\boldsymbol{f}}^{\mathrm{a}}_2(\hat{\boldsymbol{u}}^{\mathrm{s}}_2)$, induced solely by the second harmonic of the blade vibration, $\hat{\boldsymbol{u}}^{\mathrm{s}}_2$. Finally, $W^{\mathrm{a}}_{\mathrm{cyc},2}(\hat{\boldsymbol{u}}^{\mathrm{s}})$ is the work done by the aerodynamic force, $\hat{\boldsymbol{f}}^{\mathrm{a}}_2(\hat{\boldsymbol{u}}^{\mathrm{s}})$, induced by all H^{s} retained harmonics of the blade vibration. It is found that $W^{\mathrm{a}}_{\mathrm{cyc},2}(\hat{\boldsymbol{u}}^{\mathrm{s}}_2) \approx 59\% \cdot W^{\mathrm{a}}_{\mathrm{cyc},2}(\hat{\boldsymbol{u}}^{\mathrm{s}})$ while $W^{\mathrm{a}}_{\mathrm{cyc},2}(\hat{\boldsymbol{u}}^{\mathrm{s}}_1) \approx 13\% \cdot W^{\mathrm{a}}_{\mathrm{cyc},2}(\hat{\boldsymbol{u}}^{\mathrm{s}})$. This analysis confirms that the aerodynamic force induced by the fundamental harmonic vibration component indeed accounts for a significant portion of the power provided to the second harmonic vibration component. Note also that the superposition of the individual work contributions yields $W^{\mathrm{a}}_{\mathrm{cyc},2}(\hat{\boldsymbol{u}}^{\mathrm{s}}_1) + W^{\mathrm{a}}_{\mathrm{cyc},2}(\hat{\boldsymbol{u}}^{\mathrm{s}}_2) < W^{\mathrm{a}}_{\mathrm{cyc},2}(\hat{\boldsymbol{u}}^{\mathrm{s}})$. Thus, the power input to the second harmonic vibration component cannot be explained by the individual work contributions, which indicates that the nonlinear coupling (energy exchange) among harmonics is relevant to explain the observed phenomenon. It should be emphasized that the above described analysis is only feasible with a frequency domain approach since individual harmonics cannot simply be activated/deactivated in the time domain.

7.8 LTO12-14-16

As stated above, when initial values corresponding to the ND 3 mode are imposed, a limit torus (quasi-periodic) is reached instead of a LCO3. While a periodic oscillation has a single base frequency, quasi-periodic ones have two or more rationally independent (incommensurable) base frequencies, cf. Eq. (2.15). The Harmonic Balance method relies on a truncated Fourier series with a single base frequency (Eq. (2.25)). Generalizations exist that account for multiple base frequencies. For two base frequencies, ω_1 and ω_2, the truncated Fourier series would generalize to

$$\boldsymbol{u}^{\mathrm{s}}(t) \approx \Re\left\{ \sum_{(j,k)\in\mathcal{H}} \hat{\boldsymbol{u}}^{\mathrm{s}}_{j,k} e^{\mathrm{i}(j\omega_1 + k\omega_2)t} \right\}, \quad \mathcal{H} \subset \mathbb{Z}^2. \tag{7.2}$$

In its current form, the FD-FSI solver is limited to a single base frequency and thus strictly periodic oscillations. Thus, although no useful comparison to the results of the FD-FSI solver can be made, this interesting form of vibration is analyzed in the following.

The transient to the limit torus is illustrated in **Figure 7.8**. Interestingly, the initial vibrations grow and seem to settle in a LCO3 first (with an amplitude also reported by the FD-FSI solver for ND 3). Then, however, a transition occurs (at $t \cdot f_{\mathrm{ref}} \approx 20$) and the vibrations instead reach a quasi-periodic limit state with a noticeable increased spectral

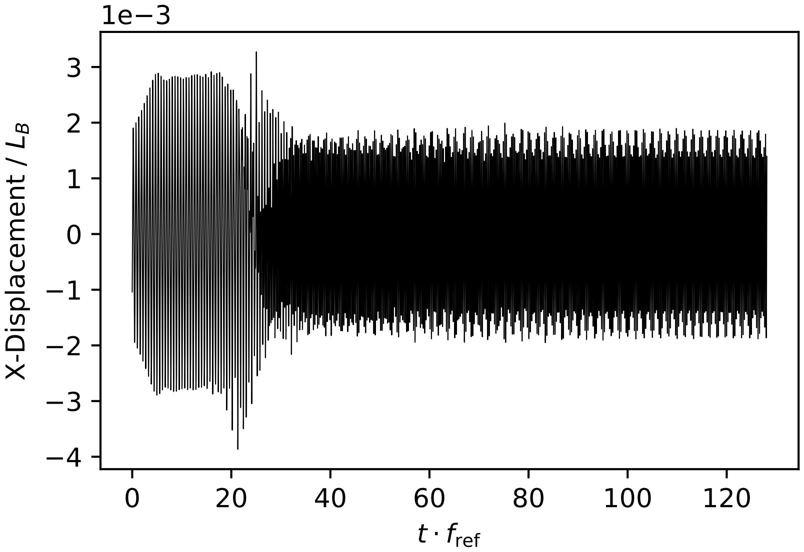

Figure 7.8: X-Displacement over time at sensor node for LTO12-14-16 [F].

content. This means that either the LCO3 is not asymptotically stable or that the initial value is not in the corresponding basin of attraction.

7.8.1 Spectral Content of the LTO; Internal Combination Resonance Condition

The results in **Figure 7.6(c)** reveal one "basic wave package" in the lower right part of the spectrum and three barely visible "wave packages" above the basic one. Each wave package contains a handful of harmonics and the basic wave package has three dominant harmonics with NDs 12, 14 and 16 with associated frequencies $f_{\text{ND12}} = 3.0 f_{\text{ref}}$, $f_{\text{ND14}} = 3.6 f_{\text{ref}}$ and $f_{\text{ND16}} = 4.2 f_{\text{ref}}$, respectively. The NDs oscillate essentially with their individual natural frequency. To support this statement, the frequencies, f^{air}, of the lowest-frequency mode family (sticking contact conditions, in air) are plotted as red curve in **Figure 7.6(c)**. In [24] an internal combination resonance is postulated as necessary condition for the occurrence of LTOs. For the present LTO with dominating NDs 12, 14, 16, this condition takes the form $n_1 12 + n_2 14 + n_3 16 = 0$ and $n_1 f_{\text{ND12}} + n_2 f_{\text{ND14}} + n_3 f_{\text{ND16}} \approx 0\,\text{Hz}$. Indeed, it is confirmed that both relations, that concerning the spatial wave numbers and that concerning the temporal harmonics, hold for $n_1 = -1$, $n_2 = 2$ and $n_3 = -1$.

An additional interesting observation is that the harmonic with the largest amplitude ($f = 3.6 f_{\text{ref}}$, ND $= 14$) and multiples of it are "central members" of the four visible wave packages. Within each wave package, the remaining harmonics are located with a constant spacing of $\Delta f = 0.3 f_{\text{ref}}$ and $\Delta\text{ND} = 2$ around these members. This observation suggests a compact two-dimensional grid in the Fourier space for the participating waves and it could be useful for the further development of computational methods for the simulation of LTOs.

7.9 Computational Effort

In general, it is remarked that both FD-FSI and TD-FSI solvers provided very good convergence behavior throughout this work. It is very difficult to compare TD- and FD-FSI solvers in a fair way in terms of computational effort. The main reason is that the tasks are quite different: In the time domain, an initial value problem is solved until transients have sufficiently decayed. Consequently, the computational effort depends sensitively on the initial value. In the frequency domain, a periodic boundary value problem is solved and the approximation is a priori periodic. A suitable initial guess is needed, otherwise convergence cannot be expected. In spite of these quite different tasks, an idea of the orders of magnitude of the required computation effort is provided in the following.
The TD-FSI solver consists of the flow solver TRACE and a custom structural solver written in python. All simulations of the current test case are done on a cluster with two AMD EPYC 7601 CPUs on each node (64 physical cores per node). The computational costs of the FD-FSI solver vary from 115 core hours for 2 fluid harmonics to 2880 core hours for 8 fluid harmonics. A high number of fluid harmonics does not only increase the numerical costs of the fluid solver within each FSI-iteration but also increases the number of necessary FSI-iterations until the coupled solver converges. The numerical cost of the structural solver and thus the number of structural harmonics only plays a minor role. The TD-FSI simulations require a lot more computational effort than the FD-FSI simulations. Here, an important reason is the drastically reduced problem domain in case of the FD-FSI solver. The shortest simulation (LCO14) required 156,160 core hours and the LTO12-14-16 simulation took 904,320 core hours. In practice the FD-FSI simulations can be run on a single computing node while for the TD-FSI simulations 15 to 20 nodes are necessary.

8 Numerical Forced Response Analysis of a LPT Rotor Testcase with Upstream Wake Excitation

8.1 Aeroelastic Problem Setting

The content of this chapter is mainly taken from [G]. A state-of-the-art model of a low pressure turbine rotor stage subjected to aerodynamic wake excitation is considered as numerical example in the present work. The bladed disk illustrated in **Figure 6.1** comprises 60 blades with interlocked tip shrouds. The steady-state forced response is sought in the form of a symmetric and time-periodic traveling wave. This permits to reduce the problem domain to a single sector, containing one section of the bladed disk and one passage, with appropriate phase-lag boundary conditions. This is a common idealization in the presence of strong inter-sector coupling, here via tip shrouds, because then mistuning-induced localization and amplitude magnification are usually negligible [68]. A partitioned modeling approach using the FD-FSI solver is pursued, where the solid is described using three-dimensional finite elements, and the flow is resolved using a finite volume method. In the following subsections, the models of the structure and the flow are further described.

8.1.1 Structure Model

The model is largely adopted from Section 6.1.1, where additional details are given e g. on the meshing and the nonlinear static analysis carried out to account for the centrifugal loading and the subsequent linearization. Nonlinear contact interactions are considered in the yellow area indicated in **Figure 8.1**. Unilateral elastic interactions are accounted for in the normal contact direction and elastic dry friction is modeled in the tangential contact plane. The friction coefficient is set to 0.5 and the contact stiffness per area is specified as 5.3563×10^4 N/mm^3. The contact laws are imposed using contact elements coinciding with the faces of the underlying solid elements. The 12 node pairs of the conforming contact mesh are used as integration points. The shroud contact and the aerodynamic loading are the only considered sources of nonlinearity. This permits to reduce the linear finite element model of the inner structure using the conventional Craig-Bampton method. More specifically, the static constraint modes associated with

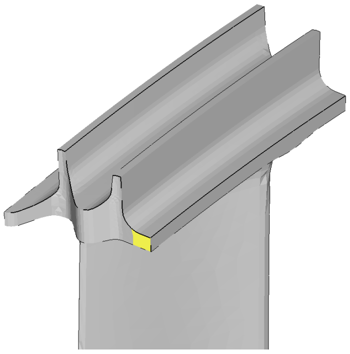

Figure 8.1: Detailed view of the contact area (yellow) [G].

the three relative displacements at each contact node pair are retained, along with the 30 lowest-frequency fixed-interface normal modes (based on a preliminary convergence study). Thus, the reduced structural sector model contains a total of $M = 66$ component modes.

8.1.2 Flow Model

The compressible unsteady Reynolds-averaged-Navier-Stokes (URANS) equations are formulated with respect to the conservative variables (density, linear momentum in three directions, energy) and with respect to the rotor's rotating frame of reference. The equations are closed with the k-ω turbulence model [69], the ideal gas law and the Sutherland law for the molecular viscosity. The passage is discretized with a finite volume mesh containing $C = 476,000$ cells.

At the inlet and the exit, two-dimensional non-reflecting boundary conditions are imposed [55]. The Mach number in the relative frame of reference at the inlet is 0.33 and at the exit 0.75. The Mach contour at 80% channel height is depicted in **Figure 8.2**. The Reynolds number with respect to the exit flow conditions and the chord of the blade is 720 000 and the stagnation pressure ratio in the absolute frame of reference amounts to 1.17. The aerodynamic wake excitation is modeled as an imposed traveling-wave type inlet disturbance, corresponding to an Engine Order of $EO = 20$. The disturbance resembles an acoustic and a vorticity wave. The prescribed generic wake is illustrated in **Figure 8.3** for six segments/blades in terms of the stagnation pressure, normalized by the maximum stagnation pressure at the inlet. The three blades on the right side are plotted transparently while the remaining blades on the left side are removed for better visibility of the inlet plane.

The forced response near the resonance of the lowest-frequency mode family with engine order 20 is analyzed in the following. The depicted results were obtained for truncation orders $H^{\mathrm{s}} = 1$ and $H^{\mathrm{a}} = 2$. This way, the effects of multi-harmonic fluid-structure interac-

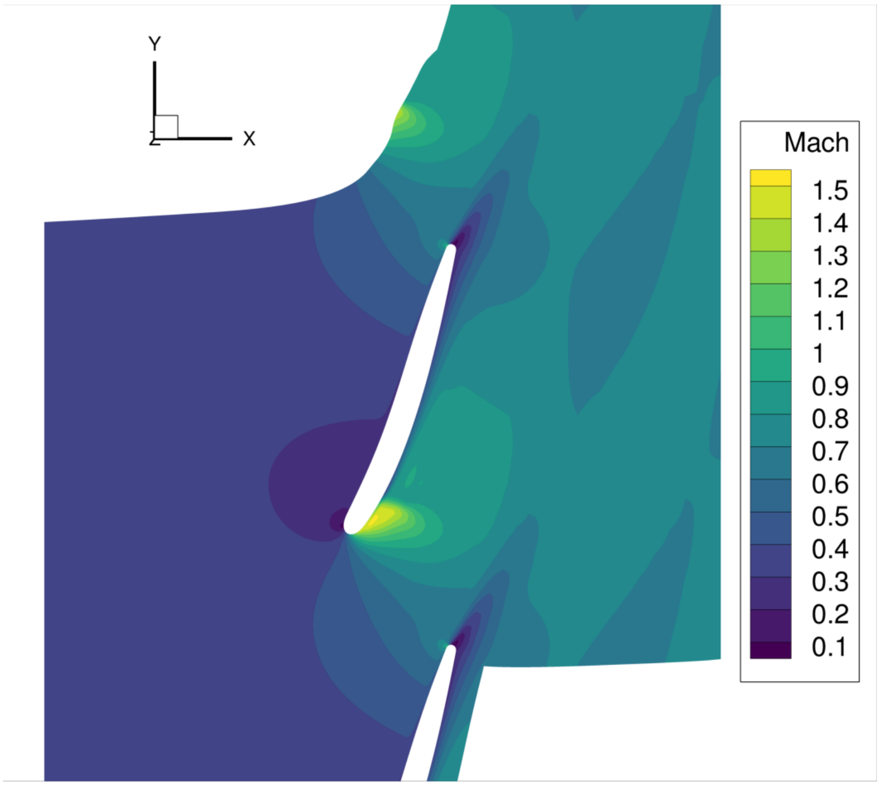

Figure 8.2: Mach number at 80% channel height for the steady flow field [G].

tion are suppressed, much like in the case of the influence-coefficients-based state-of-the-art methods. This permits a clearer interpretation of the deviations between those methods and the proposed fully coupled methods: The deviations can only be due the amplitude dependence of the aerodynamic forces and the nonlinear superposition of wake- and vibration-induced flow. It should be remarked that simulations with higher truncation orders have been carried out. The results show only slight quantitative deviations and are not depicted for brevity. In the following, first, the results of the coupled analysis are compared against the state of the art. Then the numerical performance of the distinct variants of the proposed method is assessed.

8.2 Comparison of Coupled Analysis Results Against the State of the Art

It is the current state of the art to model the aerodynamic forces in a linear way using influence coefficients, see Section 2.8.7. This corresponds to solving the structural extended residual Eq. (2.37) by numerical path continuation using as approximation for the aerodynamic force $\hat{\boldsymbol{f}}^{\mathrm{a}}$:

$$\hat{\boldsymbol{f}}_1^{\mathrm{a}} = \hat{\boldsymbol{f}}_{\mathrm{wake},1}^{\mathrm{a}} + \boldsymbol{G}_{\mathrm{a}} \hat{\boldsymbol{u}}_1^{\mathrm{s}}, \quad \hat{\boldsymbol{f}}_h^{\mathrm{a}} = \boldsymbol{0}: \;\; h = 0, 2, \ldots, H^{\mathrm{s}}. \tag{8.1}$$

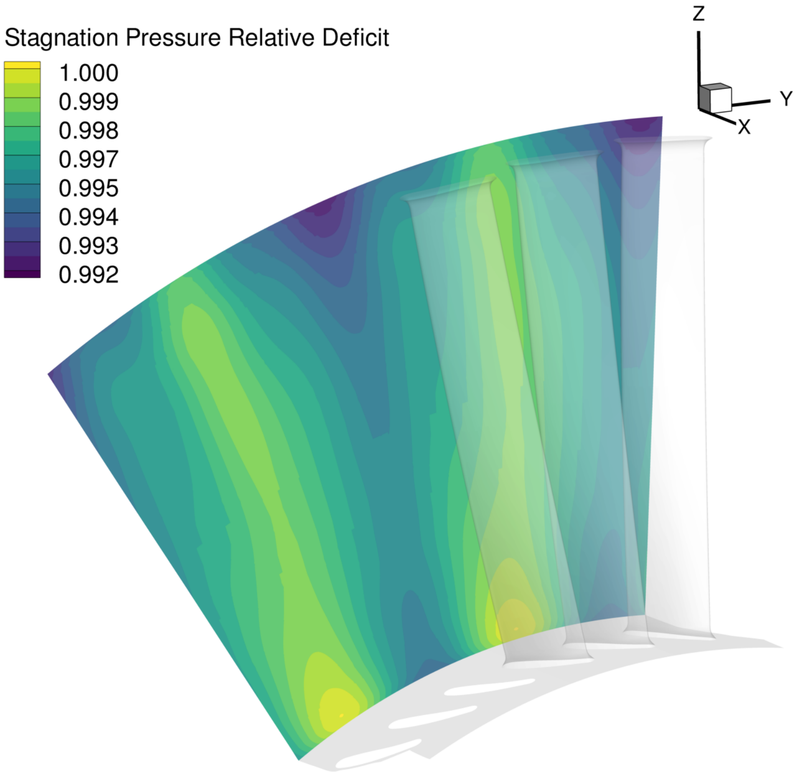

Figure 8.3: Inlet stagnation pressure relative deficit contour of generic wake excitation [G].

Herein, $\boldsymbol{G}_{\mathrm{a}}$ is the aerodynamic influence coefficient matrix, formulated in the space spanned by the component modes. Note that the approximation is inherently limited to the fundamental harmonic. Two variants are distinguished, the single-aerodynamic-influence-coefficient (*single AIC*) method, and the full-matrix-of-influence-coefficients (*AIC matrix*) method.

For the AIC matrix method, M CFD simulations are carried out, one for each component mode, where the structure vibrates with unit amplitude in the respective component mode. The resulting fundamental Fourier coefficient of the generalized aerodynamic force is used as respective column of the matrix $\boldsymbol{G}_{\mathrm{a}}$.

For the single AIC method, only a single CFD simulation is carried out, where the structure vibrates with unit amplitude in the resonant normal mode, $\boldsymbol{\psi}$, of the linearized structure (sticking contact conditions). By projecting the resulting fundamental harmonic of the generalized aerodynamic force onto $\boldsymbol{\psi}$, one obtains a scalar coefficient α. A consistent matrix $\boldsymbol{G}_{\mathrm{a}}^{\alpha}$ is then formulated,

$$\boldsymbol{G}_{\mathrm{a}}^{\alpha} = (\boldsymbol{M}\boldsymbol{\psi})\ \alpha\ (\boldsymbol{M}\boldsymbol{\psi})^{\mathrm{H}}\ , \tag{8.2}$$

where $\boldsymbol{M}$ is the mass matrix, and it is assumed that $\boldsymbol{\psi}$ is mass-normalized ($\boldsymbol{\psi}^{\mathrm{H}}\boldsymbol{M}\boldsymbol{\psi} = 1$).

The forced response is illustrated in **Figure 8.4**. As amplitude measure, the maximum X-displacement of the sensor node (see **Figure 6.1**) is used, normalized by the blade length L_{B}. The abscissa shows the rotor speed normalized by the resonance speed for the linearized structure (sticking contacts). All methods predict a sharp resonance peak (indicat-

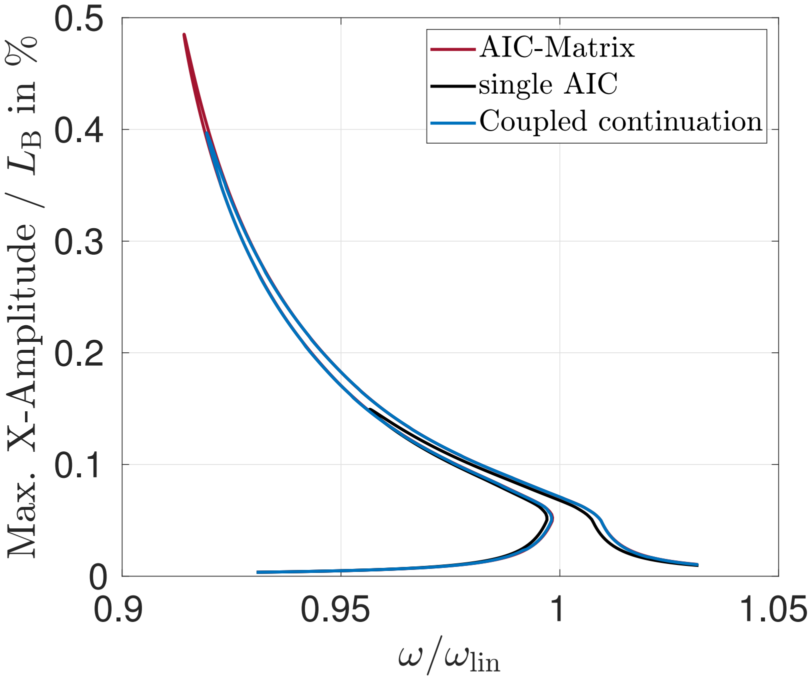

Figure 8.4: Amplitude-frequency curve: Coupled continuation vs. AIC methods [G]

ing very light damping) and a softening characteristic (resonance frequency decreasing with amplitude). These aspects are typical for pronounced normal contact interactions, in the form of temporary opening of (parts of) the interlocked shroud joint, without much sliding in the tangential contact plane (which would lead to a substantial increase of frictional damping with vibration level). This is confirmed by the contact behavior illustrated in **Figure 8.5**, which indicates a rolling-type motion at intermediate and high amplitudes. The combination of softening with light damping yields turning points with respect to the excitation frequency, a phenomenon which is probably best known from the Duffing oscillator. The overhanging branch between the two turning points is known to be unsta-

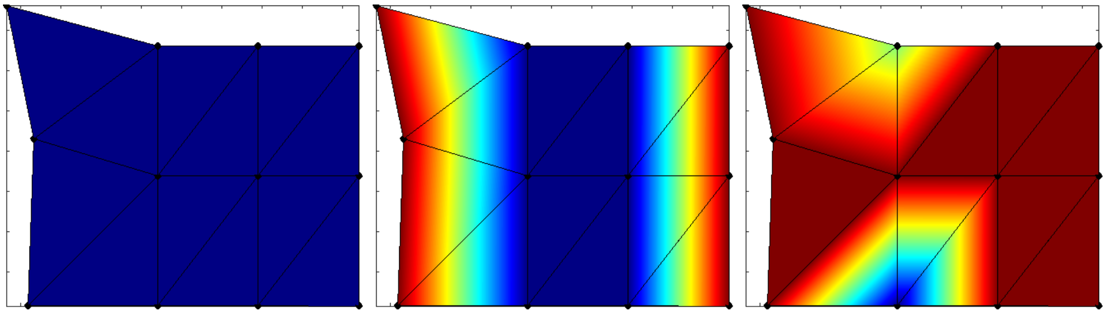
(a) (b) (c)

Figure 8.5: Contact behavior at three representative points along the upper solution branch of the forced response in **Figure 8.4** (coupled continuation result): (a) low amplitude at $\omega/\omega_{\text{lin}} = 1.03$; (b) intermediate amplitude at $\omega/\omega_{\text{lin}} = 0.98$; (c) high amplitude at $\omega/\omega_{\text{lin}} = 0.93$. Color blue represents permanently sticking contact elements. Red indicates elements, which separate at least once during the vibration cycle. Intermediate colors indicate amount of sliding during the vibration cycle [G].

ble.

While the results obtained by the three methods agree qualitatively, substantial quantitative differences appear. All results align well at sufficiently low amplitudes, where the shroud contact is permanently sticking (**Figure 8.5**a) and the system behaves in good approximation linear. In that case, the vibrational deflection shape is dominated by the resonant linear mode, $\boldsymbol{\psi}$, and the single AIC method is consistent with the AIC matrix method. At higher amplitudes, dynamic contact interactions occur, including sliding and temporary liftoff phases during the vibration cycle. Thus, the effective deflection shape changes, and the single AIC method is no longer consistent with the AIC matrix method. Remarkably, the results differ with respect to the resonant amplitude by a factor of two. In this numerical example, apparently, the deflection shape changes in such a way that the effective aerodynamic damping is lower. The aerodynamic damping for the linear mode (sticking contacts) amounts to about 1% logarithmic decrement. A strong sensitivity of the aerodynamic damping on the deflection shape was also found in the flutter analyses in [C, D]. Besides the state-of-the-art AIC methods, the newly developed coupled continuation methodology introduced in Section 4.4.1 is applied to the current test case. The coupled continuation result is somewhere between those of the two AIC methods in this case. Like the coupled continuation method, the AIC matrix method is generally able to account for a change of the deflection shape. The difference between AIC matrix method and coupled continuation could be due to the amplitude-dependence of the aerodynamic force or due to the invalid superposition of wake- and vibration-induced flow, and this is further analyzed in the following.

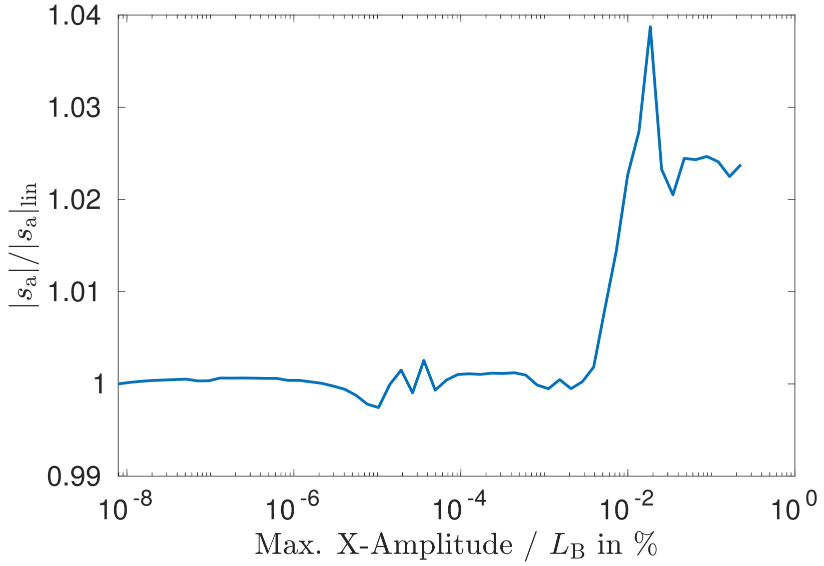

Figure 8.6: Modal aerodynamic stiffness (according to Eq. (8.3)) vs. amplitude [G]

To analyze the amplitude-dependence of the aerodynamic force, a ratio s_a is analyzed, which is defined as

$$s_\mathrm{a} = \frac{\boldsymbol{e}^\mathrm{T}\hat{\boldsymbol{f}}}{\boldsymbol{e}^\mathrm{T}\hat{\boldsymbol{u}}^\mathrm{s}} \,. \tag{8.3}$$

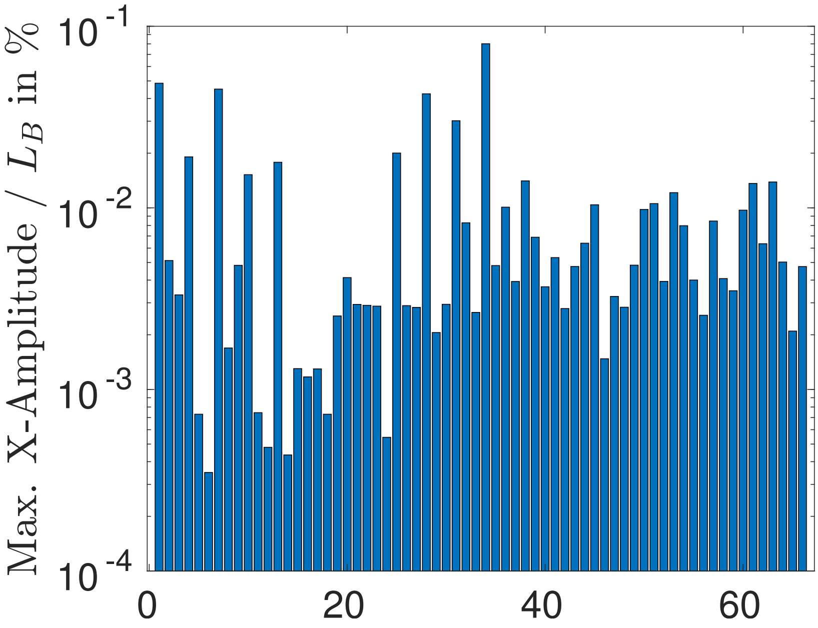

Figure 8.7: Amplitude of X-Displacement at sensor node for component modes with unit amplitude [G]

Herein, $\boldsymbol{e}$ selects the entry corresponding to the fundamental Fourier coefficient associated with the resonant fixed-interface normal mode (also used in Eq. (4.18)). $\hat{f}$ is obtained by a CFD simulation where the blade vibrates in this mode. The amplitude of this mode is varied and the results are shown in **Figure 8.6**. In the plot, $|s_{\mathrm{a}}|$ is normalized to have a value of 1 in the linear case. For amplitudes up to $2 \cdot 10^{-3}\%L_{\mathrm{B}}$, the deviation from linearity is in the numerical noise floor. Then a distinct but small deviation of up to 3.8% is visible, which is induced by a slight change of the shock dynamics in the tip region of the blade. This small deviation alone does not seem to have the potential to explain the discrepancy between AIC matrix method and coupled continuation observed in **Figure 8.4**. It should be noted that the influence coefficients are obtained for finite amplitudes. More specifically, a unit amplitude is prescribed. To get an idea of the order of magnitude of this amplitude, it is depicted in **Figure 8.7** for the X-displacement of the sensor node. Note that some amplitudes are very low because the deflection shape is mainly oriented orthogonal to the X-direction. Clearly, the amplitudes are small and largely negligible when compared to the forced response amplitudes in **Figure 8.4**. It should be remarked that the evaluation with finite amplitudes (and with harmonic balance) was chosen over a linear CFD solver in order to achieve a consistent turbulence modeling, which requires second-harmonic terms that cannot be captured by a linear solver.

Next, it is analyzed to what extent the superposition of wake- and vibration-induced flow holds. To this end, the coupled solution point with the highest vibration amplitude is considered. The pressure field induced solely by the vibration, $\hat{p}_{\mathrm{vib}}$, is computed, and the deviation $\Delta\hat{p}$,

$$\Delta\hat{p} = \hat{p} - \left(\hat{p}_{\mathrm{wake}} + \hat{p}_{\mathrm{vib}}\right) , \tag{8.4}$$

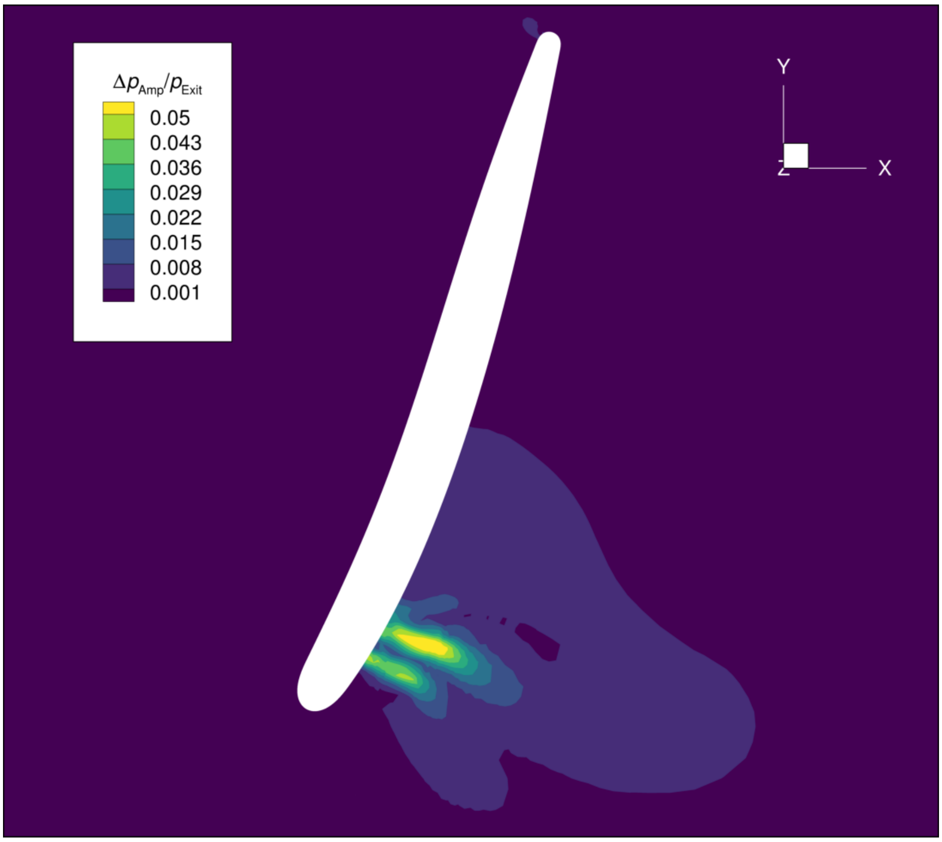

Figure 8.8: Deviation $\Delta\hat{p}_1$ between the pressure field obtained by the coupled solver and the linear superposition of wake- and vibration-induced pressure field, normalized by the exit pressure, depicted at 80 % blade height [G].

between the sum of wake- and vibration-induced pressure field, on the one hand, and the pressure field $\hat{p}$ obtained from the coupled solver, on the other hand, is determined. The fundamental Fourier coefficient, $\Delta\hat{p}_1$, is depicted in **Figure 8.8** at 80 % blade height, normalized by the exit pressure. Apparently, the superposition fails, in particular, near the location of the shock (see also **Figure 8.2**), where the superposition error amounts to 5.5%.

8.3 Assessment of the Numerical Performance of the Developed Methods

For the coupled continuation results shown so far, the coupling loop was simply activated every 15th point. As alternative, the coupling loop is activated if the vibrational deflection shape (or mode shape) changed, in accordance with the correlation measure in Eq. (4.19) and with the threshold $\beta > 0.02$, using the mode shape of the previous coupled solution point as reference. The results are compared in **Figure 8.9(a)**. The amplitude-frequency curves are largely indistinguishable. Minor deviations occur only at low amplitudes before the coupling loop is activated for the second time, see zoom in **Figure 8.9(a)**. With the

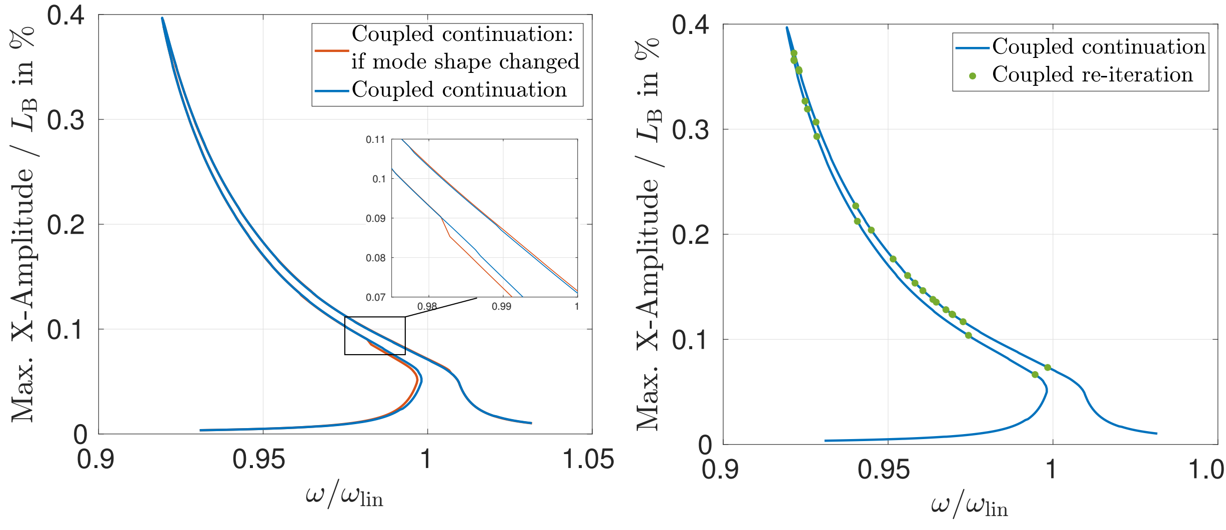

(a) Coupled continuation with two different activation criteria for the coupling loop.

(b) Coupled continuation vs. coupled re-iteration.

Figure 8.9: Amplitude-frequency curves [G]

mode-shape-based activation criterion, the number of coupled iterations along the continued branch is reduced from 29 to 16. This reduced the wall clock time of two weeks by one week (**Table 8.1**). There is certainly potential for more sophisticated and problem-adapted criteria for activating the coupling loop; but these are considered beyond the scope of the present work.

Coupled continuation and coupled re-iteration results (introduced in Section 4.4.2) are compared in **Figure 8.9(b)**. The green dots correspond to the re-iterated solution points and are in excellent agreement with the solution branch obtained by coupled continuation. A total of 25 points is selected for re-iteration. These are indicated as black circles on the old solution branch (black solid line) in **Figure 8.10**a, whereas the re-iterated points are indicated as green dots. Comparing closely **Figure 8.4** and **Figure 8.10**a, one may notice that the single AIC solution branch differs. This is because not the consistent influence coefficient (α) obtained by CFD was used but a generic value in the same order of magnitude (1.5% instead of 1% logarithmic decrement). Still, consistent results of both coupled analysis methods are achieved.

For a representative initial point near the resonance peak, the sequence of points generated during the coupled re-iterations is shown in **Figure 8.10**b. Recalling that the iterated solution points are required to lie in the hyper-plane orthogonal to the tangent at the selected point on the old solution branch, one may wonder why the iterated points are not on a straight line in **Figure 8.10**b. The reason for this is that the orthogonality holds only in the space of the unknowns, X_S, not in the amplitude-frequency space depicted here, since the amplitude is a nonlinear function (weighted Euclidean norm) of X_S. Further, it is remarkable that only three iterations are needed. The corresponding decay of the residual norms in the fluid and the structure domain is depicted in **Figure 8.11**. That result is in line with the results of the coupled flutter analysis in [C, D]. However, a very good initial

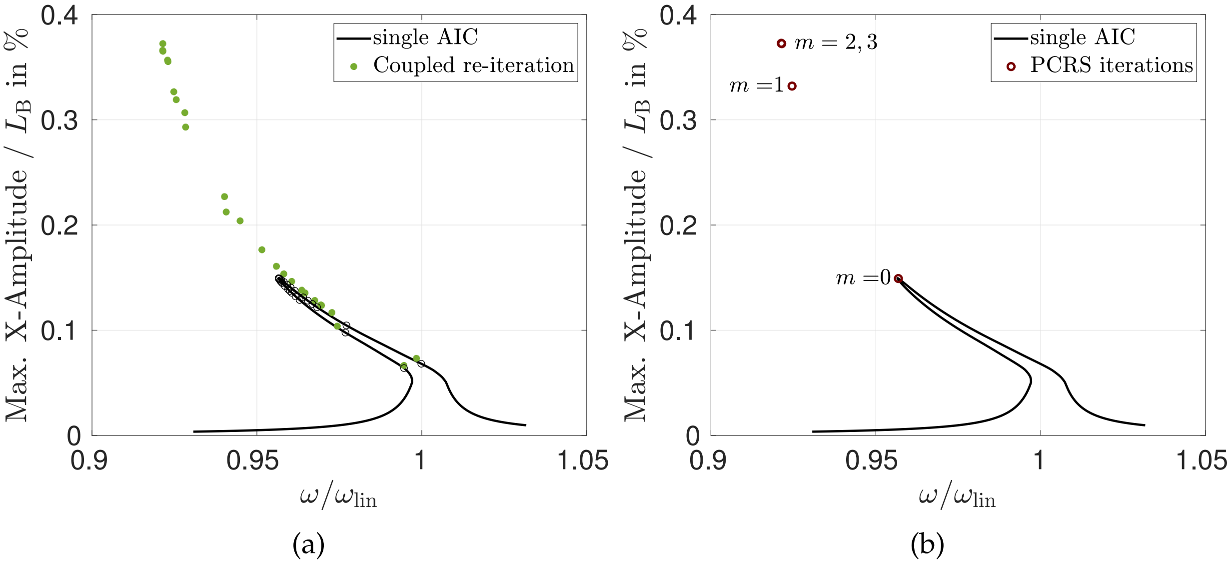

Figure 8.10: Amplitude-frequency curve obtained by coupled re-iteration: (a) initial points (black circles) on old branch and final points (green dots) on new branch; (b) sequence of points generated by coupling loop iterations for a representative point near the resonance peak [G]

guess was available in those studies, whereas the initial solution point deviates substantially (at least in terms of amplitude) in the present forced response example. The fact that still three iterations are sufficient, and the residual norms decay well, demonstrates the high robustness of the proposed numerical methods. As can be seen in **Figure 8.11**, the Newton-type structural solver requires around 5 iterations, whereas the pseudo-time fluid solver requires a few thousands of iterations. This is expected, because of the generally higher convergence rate of Newton-type solvers and much smaller number of unknowns in the structural domain.

In general, one may expect that the coupling loop converges more rapidly during the continuation, because the initial guess then always remains close to the actual solution, in contrast to the points on the decoupled branch which could be much further away. Thanks to the excellent convergence of the coupled re-iterations, however, the computational effort per solution point is not much larger than in the case of the coupled continuation method. As the coupled re-iterations can be run completely in parallel, the wall clock time is reduced from two weeks to only two days, while the total number of core hours is slightly larger (**Table 8.1**). In fact, the wall clock time of the coupled re-iteration is in the order of magnitude of the (generally less accurate) state-of-the-art methods, and the total number of core hours is smaller than in the case of the AIC matrix method (**Table 8.1**).

A weakness of the coupled re-iteration is that the obtained points are not necessarily distributed in a favorable way along the new solution branch. One means to close the gaps between the, in some regions scarce, re-iterated points is to relaunch path continuation form these points. This, again, could be done in parallel for all re-iterated points. The continuation should stop when another re-iterated point is reached. One possibility is to carry out a fully coupled continuation when closing those gaps. In **Figure 8.12**, instead, results

Method	wct (fluid+solid) /h	tch (fluid+solid) /h
steady CFD	3.4+0=3.4	217+0=217
single AIC	9.45+0.19=9.64	605+0.19=605.19
AIC matrix	10.2+0.28=10.48	43084.8+0.38=43085.18
coupled cont. (coupling every 15th point)	290.0+0.30=290.3	18560+0.3=18560.3
coupled cont. (cpl. if mode shape changed)	144.0+0.30=144.3	9216.0+0.3=9216.3
coupled re-iteration (parallel)	29.3+0.02=29.32	32286.8+0.02=32286.82

Table 8.1: Comparison of wall clock time (wct) and total core hours (tch) for the different methods [G].

are shown for a decoupled continuation. More specifically, the approximation $\hat{f}$ according to Eq. (4.18) is updated at the re-iterated point, and this approximation is subsequently used. The important advantage of this procedure is that no further CFD simulation is needed, so that the computational effort is negligible. The downside is that the results are slightly less accurate. Indeed, the error increases with the distance from the re-iterated point. Still, the amplitude deviation of the resonance peak is less than 3%, which can be deemed acceptable.

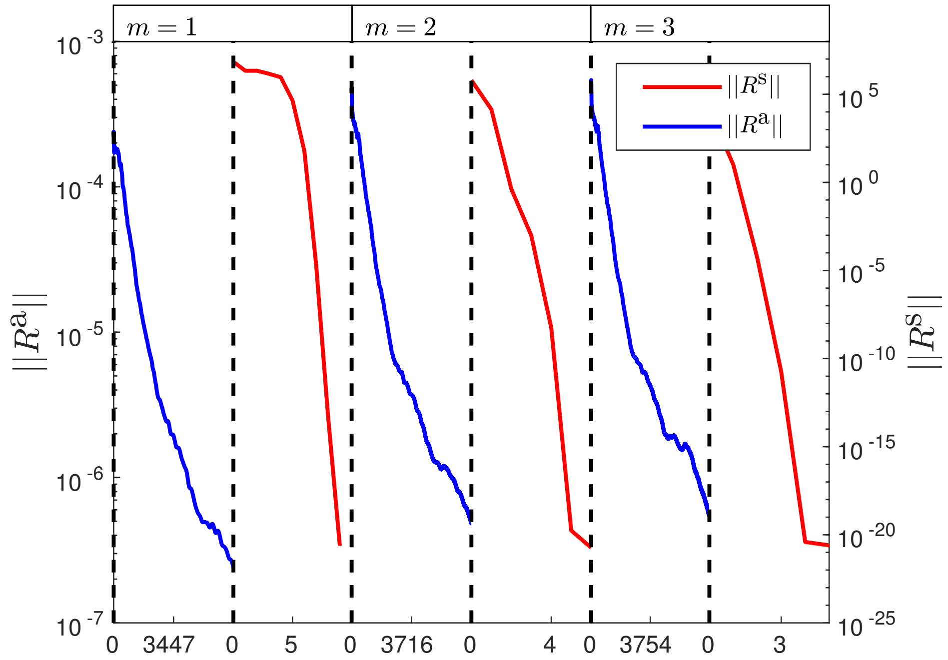

Figure 8.11: Decay of residuals in fluid and structural domain for the coupling loop iterations illustrated in **Figure 8.10**b [G].

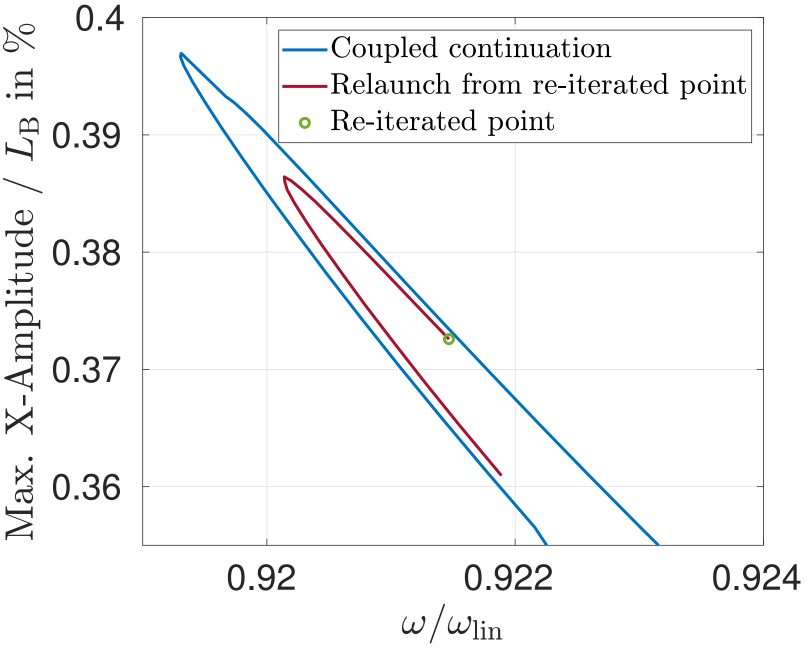

Figure 8.12: Amplitude-frequency curve near resonance peak: coupled continuation vs. relaunch of (decoupled) continuation from a re-iterated point [G]

9 Discussion of the Results

In this work new numerical methods for the analysis of flutter induced LCOs are presented and applied to LPT testcases with contact friction interfaces in the shroud. In the following, the research findings are summarized, the potential of the developed methods is evaluated and advantages and disadvantages are discussed.

9.1 The Refined Energy Method

As benchmark, two state-of-the-art aeroelastic models of bladed disks subject to nonlinear contact interactions at the interlocked tip shrouds were considered. The current practice for the prediction of friction-saturated flutter induced LCOs relies on the assumption that frequency and form match the natural frequency and deflection shape obtained for linearized contact conditions and in vacuum. The present work demonstrates that this practice can lead to qualitatively wrong results.

In contrast to the conventional energy method, the Refined Energy Method (REM) accounts for the amplitude-dependence of the oscillation frequency and the mode shape. Thus, it is suitable for an assessment of several possible limit cycles over a wide amplitude range from a balance of energy perspective and furthermore it helps to analyze the different effects of contact and aerodynamic forces in isolation, which allows deeper understanding of the physics of nonlinear aeroelastic interactions. Two ways of including the aerodynamic influence have been presented.

The first possibility is to use an aerodynamic influence coefficient matrix, which allows parameter studies, provided that the parameters of interest have no effect on the component modes of the ROM (e.g. contact parameters). In this case, the influence coefficients must be determined only once in a preprocessing step, cf. Section 5.5. For other parameters, which influence the ROM modes, however the AIC matrix must be recomputed. Furthermore, using the AIC matrix allows a bidirectional analysis (REM "in air", see Section 6.3), where the interaction between nonlinear structural behavior and the fluid can be taken into account, at least to the extent where the assumption of linear aerodynamic forces remains valid. The disadvantage of the AIC matrix are the numerical costs which are proportional to the structural model's number of generalized coordinates, which can be quite significant for a detailed description of the contact interface. Finally, nonlinear effects of the aerodynamic forces are neglected, which however turned out to be an acceptable approximation for most cases.

The second possibility is to evaluate the aerodynamic forces for a set of different amplitudes (of the nonlinear modal analysis), spanning a technically relevant amplitude range. For this purely uni-directional approach, the computational costs are proportional to the number of evaluated solution points and thus, usually lower than for a fully populated influence coefficient matrix. For each parameter variation of the mechanical system however, the aerodynamic forces must be recomputed for the set of different amplitudes, which makes this option less flexible and more appropriate for the evaluation of a single mechanical design. Finally, the explicit evaluation of the aerodynamic forces with a nonlinear fluid solver allows to capture nonlinear aerodynamic effects. Although this did not play a significant role in case of the REM applied to flutter induced LCO test cases, it turned out to be necessary for the forced response analysis (see Section 9.4).

The application of the REM to the test cases shows, that the REM delivers a significant advantage over the classical energy method due to the consideration of (structural and fluid) nonlinear effects such as friction with a moderate amount of computational costs. It is emphasized that the REM allows the modeling of the structure and the fluid on a very detailed and sophisticated level with state-of-the-art methods, and it has the potential to have a significant impact in the future development of turbomachinery components. Thus, the developed method fulfills the goals formulated in Chapter 3.

9.2 Frequency Domain - Fluid Structure Interaction Solver

The FD-FSI solver is developed in order to simulate flutter induced LCOs and forced response of turbomachinery blades in a highly accurate fashion. It showed excellent convergence behavior for reasonable computational effort and harmonic convergence of the results against reference time domain solutions was demonstrated. As the FD-FSI solver follows a serial coupling strategy, available frequency domain codes can be used which are optimized for the respective structural and fluid subproblem. Thus, it can be considered as a high-fidelity method.

In Section 7.7 it was demonstrated for a flutter induced LCO, that higher harmonics may appear due to vibration-induced shock motion under the condition of an internal resonance. Here, the FD-FSI solver proved to be able to resolve the complex fluid-structure interactions also among higher harmonics, but only at a fraction of the computational costs of coupled time The solver allows to analyze and understand the physical mechanism behind this interesting phenomenon efficiently and directly, because the frequency domain solution permits to assess the harmonic spectrum without any further postprocessing. While the REM in air could be extended to the treatment of higher harmonics for this kind of interaction, the influence coefficient matrix would need to be computed not only for the fundamental harmonic but for all relevant harmonics, which makes this approach very costly and thus unfeasible. Furthermore, it is questionable whether all nonlinear interactions can be resolved with linearized aerodynamic forces, as the evaluation of the transfer of energy among the harmonics showed.

Even if the aerodynamic forces remain linear in the vibration amplitude and no complex fluid-structure interactions are to be expected, the FD-FSI solver might nevertheless be an attractive alternative to the REM in air. The reason for this is that the influence coefficients need to be computed for a large number of component modes in order to accurately describe variation of the vibrational deflection shape within the REM while for the FD-FSI solver usually not more than 5 iterations (and thus 5 CFD simulations) are necessary to converge.

A further big advantage of the FD-FSI solver over coupled time domain solvers is the ability of harmonic balance to simulate very stiff differential equations without using very small time steps or artificial damping, which makes it more convenient for simulating blade vibrations with dry friction compared to coupled time integration methods.

The integration of the FD-FSI solver into forced response analysis allows to efficiently predict the forced response of turbomachinery blades accounting for both aerodynamic and structural nonlinearities. Also for this application, the FD-FSI solver showed excellent numerical performance. To robustly analyze the near-resonant response and to deal with turning points, the coupled solver was embedded in a numerical path continuation framework. Two variants were developed, the coupled continuation of the solution branch and the coupled re-iteration of selected solution points. In the former variant, the idea is to activate the coupling loop only when needed, and to use the local approximation of the aerodynamic force otherwise. The important advantage of the coupled re-iteration is that it can be carried out completely in parallel, reducing the wall clock time to the order of magnitude of the current state-of-the-art methods which are based on aerodynamic influence coefficients. The latter are generally less accurate, as they neglect the amplitude dependence of the aerodynamic forces and assume the linear superposition of wake- and vibration-induced flow, which was shown to have substantial effects on the predicted resonance amplitude in the numerical example. To close the gap between the re-iterated points, it is proposed to relaunch the continuation procedure, again, in parallel, so that a sufficiently finely spaced solution path is retrieved. In the future, more sophisticated indicators could be developed that activate the coupling loop only when a significant deviation from linearity is encountered.

The abilities of the FD-FSI solver are above of the initial expectations and thus the original goal of improving the prediction quality and efficiency is considered to be achieved. It can be considered to be superior to conventional TD-FSI solvers when LCOs are the focus of a numerical analysis.

9.3 Analysis of the Impact of Nonlinear Friction on Flutter Induced LCOs of Turbomachinery Cascades

For the first test case (Section 5.3), a limit cycle under relatively low flutter intensity was analyzed. The oscillation frequency and vibrational deflection shape were thus close to the linear case under sticking contact conditions. Hence, the conventional energy method yields a reasonable approximation and is therefore in good agreement with the newly developed methods. The second configuration of the first test case (Section 5.4) demonstrated, for the first time, the phenomenon of nonlinear blade flutter instability, i. e., a situation where the static equilibrium (sticking contact conditions) is stable, but the vibrations start to grow unboundedly once the initial vibration amplitude exceeds a certain threshold. Neither linear theory nor the conventional energy method are able to predict this behavior, while the newly developed methods are both able to determine the critical amplitude (stability limit).

In contrast to the first LPT test case, the second one (see Chapter 6) has a much higher flutter intensity. In this case, the amplitude-dependent stiffness provided by friction joints and the aerodynamic stiffness have the potential to significantly alter the frequency and deflection shape of the limit cycle. The aerodynamic damping shows a sensitive dependence on both frequency and mode shape, which leads to a complicated nonlinear interaction. Both approaches, the REM in air and the FD-FSI solver are well qualified to consistently account for the effect of both nonlinear contact boundary conditions and aerodynamic forces on the frequency and form of the limit cycle oscillations.

An interesting observation is the impact of the amplitude-dependent frequency and mode shape on the aerodynamic damping which was analyzed for both test cases (Section 5.4 and Chapter 6). For the first test case the frequency played a major role and the mode shape a minor one, cf. Section 5.4.2. Due to the frequency change, the aerodynamic damping changed from positive values for small amplitudes to negative values for large amplitudes. In Section 6.3, however, the change in mode shape played major role: the change from negative to positive aerodynamic damping is induced by the change in mode shape. Thus, it is concluded that in the general case both effects should be accounted for.

For most of the results, the good agreement between FD-FSI solver and REM/REM in air confirms that the aerodynamic forces can, in a wide range, be well approximated as amplitude-linear and by using a linear interpolation of the modal aerodynamic influence coefficients with respect to frequency. However, in special cases where strong aerodynamic nonlinearities such as oscillating shocks could potentially interact with nonlinear blade vibrations, the hypothesis of linear aerodynamic forces should be verified.

Finally, the simulation of the LTO confirmed two hypotheses from literature. The first one is the observation that the LCOs corresponding to the barely negative NDs tend to be not asymptotically stable [23]. This is confirmed in Chapter 7, where the initialization with the barely unstable ND 3 converges to a LTO and not to a LCO. The analysis of this LTO also confirmed the second hypothesis - the internal combination resonance postulated in [24]. It is again confirmed that the internal combination resonance is a necessary condition for the appearance of (quasi-periodic) limit torus oscillations. In this work however, both hypotheses are observed in a state-of-the-art and coupled FSI analysis and not, as in the past, with a drastically reduced aerodynamic model using influence coefficients.

9.4 Analysis of Nonlinear Structural and Aerodynamic Aspects on Forced Response Vibrations

In Chapter 8, a forced response analysis using the coupled FD-FSI solver reveals the potential impact of structural and aerodynamic nonlinear effects on the forced response amplitude.

First, it is shown that, as in case of flutter induced LCOs, through a change of mode shape the resulting vibration amplitude can substantially be altered due to the mode shape's impact on the aerodynamic damping.

Second, the prevailing practice to consider the aerodynamic force as a superposition of wake and blade vibration induced forces (see Section 2.8.7) is investigated for a transonic turbine blade row. While this practice is valid for a wide range of applications, the results of the nonlinear coupled methods show that it can turn out to be an invalid assumption. In the investigated case, the shock motion of the coupled analysis could not be accurately resembled by the superposition principle.

9.5 Limitations of the Proposed Methods

In Chapter 7 a comparison between the FD-FSI and a coupled time domain solver for the simulation of flutter induced LCOs is conducted, which, alongside the benefits, also reveals certain limitations of the developed methods.

Although the REM can predict the stability of the determined LCOs from a balance of energy perspective, this is not sufficient for a complete (asymptotic) stability analysis. In its current form both methods, the FD-FSI solver and the REM, are not able to provide reliable information on the asymptotic stability of the computed limit cycles, which is a general problem with harmonic balance. Furthermore, they cannot compute other types of limit states (limit tori, chaos) in their current form. These two aspects are not so severe for time domain methods. Additionally, a coupled time domain solver allows to study the transient from given initial values and the associated limit state. It is concluded that a clever combination of the FD-FSI solver and REM with time domain methods is an interesting perspective.

10 Conclusions

Preventing excessive vibration levels of turbomachinery blades is the main motivation of this work. Therefore, new numerical methods have been developed with the intent of increasing the prediction accuracy of nonlinear blade vibrations compared to existing methodologies. This should enable the design of improved turbines and compressors with reduced weight and high efficiency while being robust against blade vibrations at the same time. An important aspect of current and future designs are nonlinear friction elements, helping to mitigate vibration amplitudes. It is shown, that the newly developed refined energy method and the FD-FSI solver are capable of simulating LCOs of the blade vibrations under consideration of nonlinear structural friction for flutter and forced response. Furthermore, not only structural but also the nonlinear behavior of a moving shock in the fluid flow or the violation of the superposition principle of aerodynamic forces in a forced response setting was successfully uncovered by the FD-FSI solver. It is concluded that the novel methods are well suited for the above-mentioned design challenge.

The bidirectionally coupled solver outperforms a time domain FSI solver with respect to computational costs by orders of magnitude, which opens up the perspective of employing a coupled FSI analysis as a standard tool during the design process for the simulation of LCOs. With conventional time domain FSI solvers this is not affordable with the current computational resources. Thus, the FD-FSI solver and the refined energy methods have the potential to accelerate the development of new turbomachinery technology levels.

10.1 Open Research Questions

A remaining topic is the asymptotic stability of LCOs which cannot be determined by the proposed methods. One possibility to circumvent the difficult analysis of (in-) stability and LTOs is to remove their causes: A close frequency spacing of different modes is one reason for the instability of LCOs [70], while an internal combination resonance condition was discovered as a prerequisite for LTOs [24]. Consequently, an appropriate distribution of eigenfrequencies of all relevant modes could be considered as an additional design constraint, which is however difficult to achieve in practical applications.

While coupled time domain methods can resolve LTOs or detect asymptotic stability to a certain extent, there is still the difficulty of a structured approach for a flutter analysis in the sense, that time domain methods solve a single initial problem giving no further information on other possible limit cycles, like the refined energy method does. Building a test matrix for varying initial conditions is unfeasible due to the very high computational costs, at least for coupled FSI solvers. In order to get a more complete picture of relevant limit states and global stability of the mechanical system, the detection of bifurcations, the assessment of asymptotic stability and the simulation of LTOs is necessary. Analyses of dynamic systems with respect to stability, bifurcation points and the forming of LTOs and chaos have been carried out in e.g. [70, 23]. However, in these studies only fundamental mechanical systems or simplified models of a blade row have been considered so far. Thus, further research and ideas are needed in order to combine such numerical methods with the coupled approach developed in the current work. More specifically the extension of the coupled solver to multi-frequency harmonic balance methodologies would be necessary for the simulation for LTOs, where multiple fundamental frequencies exist and interact.

Another important topic is the uncertainty of the coupled methods. For the coupled methods presented in this work the knowledge of a result's uncertainty would be beneficial for the design of the mechanical components. This knowledge would further help in optimizing the safety margins and thus further research is necessary for this topic. Sources of uncertainty are for example the model parameters used for the contact model, the turbulence model or stochastic mistuning/manufacturing tolerances. While for each modeling discipline the analysis of uncertainty of the numerical results is already a demanding task, the evaluation of uncertainty for the coupled methods requires even more effort since the uncertainties from both domains will interact with each other.

In order to further validate the new methods, experimental tests must be carried out. First, an accurate modeling of the contact friction is a prerequisite in order to obtain a representative model of the structure, as demonstrated in [25], where a bladed disk was excited with an air jet. However, deviations between the numerical and experimental results may still arise due to the mistuning inherently present in real world components due to e.g. manufacturing tolerances. A source of uncertainty on the fluid side is e.g. the turbulence modeling and is by far not the only source of fluid modeling uncertainty. Hence, the experimental validation of the coupled methods presented in this work will be a challenging task and perfect agreement might be difficult, if not impossible, to reach. However, there is the potential of the developed methods to predict real world blade vibrations better than before.

List of frequently used symbols

Latin Letters

a	aerodynamic influence coefficient
$\boldsymbol{e}$	unit vector
$\boldsymbol{f}$	force
i	imaginary unit
p	static pressure
$\boldsymbol{q}$	vector of unknown (nodal) quantities
r	scalar residual function
t	time
u	modal amplitude
$\boldsymbol{u}$	vector of unknown quantities / generalized coordinates
D	damping ratio
E	kinetic energy
$\boldsymbol{G}$	aerodynamic influence coefficient (AIC) matrix
H	harmonic truncation order
$\boldsymbol{K}$	structural stiffness matrix
L	interpolation matrix
$\boldsymbol{M}$	structural mass matrix
$\boldsymbol{R}$	(real) residual vector function
T	period length
$\boldsymbol{T}$	matrix containing a (reduced) basis
W	work per cycle
$\boldsymbol{X}$	(real) vector of unknown quantities

Greek Letters

δ	logarithmic decrement
ϱ	density
$\boldsymbol{\chi}$	CFD mesh deformation
$\boldsymbol{\psi}$	structural normal mode
ω	angular frequency / vibration frequency

Sub- and Superscripts

$\hat{\square}$	Fourier coefficient
$\dot{\square}$	first derivative with respect to t
$\ddot{\square}$	second derivative with respect to t
a	aerodynamic/fluid quantity
c	contact related quantity
cb	Craig-Bampton
con	constraint
k	harmonic index
m	coupled solver iteration
n	path continuation step index
nl	refers to nonlinear modal analysis/refined energy method
s	structural quantity
FE	finite element
FV	finite volume

Abbreviations

AIC	aerodynamic influence coefficient
CFD	computational fluid dynamics
FD-FSI	frequency domain fluid-structure interaction (refers to the coupled solver)
LCO	limit cycle oscillation
LTO	limit torus oscillation
NMA	nonlinear modal analysis
REM	refined energy method
SL	stability limit

Publications

[A] C. Berthold. “Development of a Coupled Fluid-Structure Simulation Method in the Frequency Domain”. P&E report number: 2760. MA thesis. Faculty of Mechanical, Maritime and Materials Engineering (3mE), Delft University of Technology, 2016.

[B] C. Berthold, C. Frey, and H. Schönenborn. “Coupled Fluid Structure Simulation Method in the Frequency Domain for Turbomachinery Applications”. In: *ASME Turbo Expo 2018: Turbomachinery Technical Conference and Exposition*. American Society of Mechanical Engineers. 2018, V07CT36A014–V07CT36A014. **Contribution**: Development of coupled solver, implementation of coupling code, application to testcase and evaluation, writing of paper.

[C] C. Berthold et al. “Analysis of Friction-Saturated Flutter Vibrations With a Fully Coupled Frequency Domain Method”. In: *Journal of Engineering for Gas Turbines and Power* 142.11 (2020), p. 111007. **Contribution**: Implementation of coupling code, development of refined energy method in air, application to testcase and evaluation, writing of paper.

[D] C. Berthold et al. “Development of a fully-coupled harmonic balance method and a refined energy method for the computation of flutter-induced Limit Cycle Oscillations of bladed disks with nonlinear friction contacts”. In: *Journal of Fluids and Structures* 102 (2021), p. 103233. **Contribution**: Development of coupled solver and refined energy method, implementation of coupling code, application to testcase and evaluation, writing of paper.

[E] C. Berthold et al. “FULLY COUPLED AEROELASTIC SIMULATIONS OF LIMIT CYCLE OSCILLATIONS IN THE TIME DOMAIN”. In: *Proceedings of the 15th ISUAAAT*. 2018. URL: `https://elib.dlr.de/127137/`. **Contribution**: Implementation of coupled time domain solver, application to testcase and evaluation, writing of paper.

[F] C. Berthold et al. “Fully Coupled Analysis of Flutter Induced Limit Cycles: Frequency Versus Time Domain Methods”. In: *Journal of Engineering for Gas Turbines and Power* 145.7 (May 2023), p. 071009. ISSN: 0742-4795. DOI: `10.1115/1.4062408`. URL: `https://doi.org/10.1115/1.4062408`. **Contribution**: Development of coupled solver and refined energy method, implementation of time domain coupling code, application to testcase and evaluation, writing of paper.

[G] C. Berthold et al. “Fully Coupled Forced Response Analysis of Nonlinear Turbine Blade Vibrations in the Frequency Domain”. In: *Journal of Fluids and Structures* (2024). *Status: Revised Draft Submitted* **Contribution**: Development of coupled continuation and reiteration method, implementation of coupling code, application to testcase and evaluation, writing of paper.

Bibliography

[1] G. Ashcroft, C. Frey, and H.-P. Kersken. "On the Development of a Harmonic Balance Method for Aeroelastic Analysis". In: *6th European Conference on Computational Fluid Dynamics (ECFD VI)*. 2014.

[2] D. Blom et al. "A Review on Fast Quasi-Newton and Accelerated Fixed-Point Iterations for Partitioned Fluid-Structure Interaction Simulation". In: *Advances in Computational Fluid-Structure Interaction and Flow Simulation*. Springer International Publishing, 2016, pp. 257–269. DOI: `10.1007/978-3-319-40827-9_20`.

[3] A. de Boer, A. H. van Zuijlen, and H. Bijl. "Comparison of conservative and consistent approaches for the coupling of non-matching meshes". In: *Computer Methods in Applied Mechanics and Engineering* 197.49-50 (2008), pp. 4284–4297.

[4] A. de Boer, A. H. van Zuijlen, and H. Bijl. "Review of coupling methods for non-matching meshes". In: *Computer methods in applied mechanics and engineering* 196.8 (2007), pp. 1515–1525.

[5] J. C. Butcher. "Implicit Runge-Kutta Processess". In: *Math. Comp.* 18 (1964), pp. 50–64.

[6] A. Cadel et al., eds. *Computing fluid structure interaction coupling time spectral method (TSM) and harmonic balance method (HBM)*. Vol. 7B-2017. 2017. DOI: `10.1115/GT2017-64260`.

[7] V. Carstens, R. Kemme, and S. Schmitt. "Coupled simulation of flow-structure interaction in turbomachinery". In: *Aerospace Science and Technology* 7.4 (2003), pp. 298–306. DOI: `10.1016/S1270-9638(03)00016-6`.

[8] F. O. Carta. "Coupled blade-disk-shroud flutter instabilities in turbojet engine rotors". In: *Journal of Engineering for Power*. American Society of Mechanical Engineers 89 (1967). URL: `http://books.google.de/books?id=HqYrQwAACAAJ`.

[9] M. P. Castanier and C. Pierre. "Modeling and Analysis of Mistuned Bladed Disk Vibration: Current Status and Emerging Directions". In: *Journal of Propulsion and Power* 22.2 (2006), pp. 384–396.

[10] R. Corral and J. M. Gallardo. "Nonlinear dynamics of bladed disks with multiple unstable modes". In: *AIAA journal* 52.6 (2014), pp. 1124–1132.

[11] R. Corral, J. M. Gallardo, and C. Vasco. "Aeroelastic stability of welded-in-pair low pressure turbine rotor blades: A comparative study using linear methods". In: *Journal of Turbomachinery* 129.1 (2007), pp. 72–83.

[12] R. R. Craig and M. C. Bampton. "Coupling of substructures for dynamic analyses". In: *AIAA Journal* 6.7 (1968), pp. 1313–1319.

[13] J. Degroote et al. "Performance of partitioned procedures in fluid–structure interaction". In: *Computers & structures* 88.7-8 (2010), pp. 446–457.

[14] K. D'Souza, C. Jung, and Epureanu B. I. "Analyzing Mistuned Multi-Stage Turbomachinery Rotors With Aerodynamic Effects". In: *Journal of Fluids and Structures* 42.0 (2013), pp. 388–400. ISSN: 0889-9746. DOI: `10.1016/j.jfluidstructs.2013.07.007`.

[15] K. Ekici and H. Huang. "An assessment of frequency-domain and time-domain techniques for turbomachinery aeromechanics". In: *30th AIAA Applied Aerodynamics Conference 2012*. June 2012, pp. 1807–1823. ISBN: 9781624101854. URL: `http://www.scopus.com/inward/record.url?eid=2-s2.0-84880795955&partnerID=40&md5=8f1901a16de5617ef3a6e89851aaab4e`.

[16] A. Engels-Putzka, J. Backhaus, and C. Frey. "On the usage of finite differences for the development of discrete linearised and adjoint CFD solvers". In: *Proceedings of the 6th. European Conference on Computational Fluid Dynamics - ECFD VI*. Ed. by E. Oñate, X. Oliver, and A. Huerta. July 2014. URL: `http://www.wccm-eccm-ecfd2014.org/admin/files/filePaper/p1796.pdf`.

[17] J. I. Erdos, E. Alzner, and W. McNally. "Numerical Solution of Periodic Transonic Flow through a Fan Stage". In: *AIAA J.* 15.11 (Nov. 1977), pp. 1559–1568. ISSN: 0001-1452. DOI: `10.2514/3.60823`. URL: `http://dx.doi.org/10.2514/3.60823`.

[18] D. M. Feiner and J. H. Griffin. "A Fundamental Model of Mistuning for a Single Family of Modes". In: *Journal of Turbomachinery* 124.4 (2002), pp. 597–605. DOI: `10.1115/1.1508384`.

[19] A.-L. Fiquet, X. Ottavy, and C. Brandstetter. "UHBR OPEN-TEST CASE FAN ECL5/CATANA: Non-linear analysis of Non-Synchronous Blade Vibration at part-speed conditions". In: (2024). DOI: `10.1115/1.4064841`. URL: `https://www.semanticscholar.org/paper/72dbf4c838dd770e531026c6f410d162eec4b825`.

[20] C. M. Firrone and S. Zucca. *Modelling Friction Contacts in Structural Dynamics and its Application to Turbine Bladed Disks*. Intech, 2011.

[21] C. Frey et al. "A Harmonic Balance Technique for Multistage Turbomachinery Applications". In: *ASME Turbo Expo 2014: Turbine Technical Conference and Exposition*. 45615. 2014, V02BT39A005. DOI: `10.1115/gt2014-25230`. URL: `http://dx.doi.org/10.1115/GT2014-25230`.

[22] Y. Gong and W. Zhang. "Efficient aeroelastic solution based on time-spectral fluid–structure interaction method". In: *AIAA Journal* 57.7 (2019), pp. 3014–3025.

[23] J. González-Monge, S. RodrÃguez-Blanco, and C. Martel. "Friction-induced traveling wave coupling in tuned bladed-disks". In: 106 (2021), pp. 2963–2973. ISSN: 0924-090X. DOI: `10.1007/s11071-021-06930-1`.

[24] J. Gross and M. Krack. "Multi-Wave Vibration Caused by Flutter Instability and Nonlinear Tip-Shroud Friction". In: *Journal of Engineering for Gas Turbines and Power* 142.2 (2020).

[25] A. Hartung et al. "Rig and engine validation of the non-linear forced response analysis performed by the tool OrAgL". In: *J. Eng. Gas Turbines Power* 141.2 (2018), 9pp.

[26] S. Henninger et al. "Time-domain implementation of higher-order non-reflecting boundary conditions for turbomachinery applications". In: *Turbo Expo: Power for Land, Sea, and Air*. Vol. 56642. American Society of Mechanical Engineers. 2015, V02BT39A016.

[27] H. Huang et al. "An efficient aeroelastic eigenvalue method for analyzing coupled-mode flutter in turbomachinery". In: *Journal of Turbomachinery* 143.2 (2021).

[28] L. Junge et al. "A New Harmonic Balance Approach Using Multidimensional Time". In: *Journal of Engineering for Gas Turbines and Power* 143.8 (2021), p. 081007.

[29] H.-P. Kersken et al. "Flutter Analysis of an Embedded Blade Row with a Harmonic Balance Solver". In: *Proceedings of 12th European Conference on Turbomachinery Fluid dynamics & Thermodynamics*. 2017.

[30] H.-P. Kersken et al. "Nonreflecting Boundary Conditions for Aeroelastic analysis in Time and Frequency Domain 3D RANS Solvers". In: *Proceedings of ASME Turbo Expo 2014*. 2014.

[31] R. E. Kielb and K. R. Kaza. "Aeroelastic Characteristics of a Cascade of Mistuned Blades in Subsonic and Supersonic Flows". In: *Journal of Vibration, Acoustics, Stress, and Reliability in Design* 105 (1983), pp. 425–433.

[32] M. Krack. "Nonlinear modal analysis of nonconservative systems: Extension of the periodic motion concept". In: *Computers and Structures* 154 (2015), pp. 59–71. DOI: `10.1016/j.compstruc.2015.03.008`.

[33] M. Krack, L. Panning-von Scheidt, and J. Wallaschek. "On the interaction of multiple traveling wave modes in the flutter vibrations of friction-damped tuned bladed disks". In: *Journal of Engineering for Gas Turbines and Power* 139.4 (2016), pp. 042501–1 –042501–9.

[34] M. Krack, L. Salles, and F. Thouverez. "Vibration prediction of bladed disks coupled by friction joints". In: *Archives of Computational Methods in Engineering* 24.3 (2017), pp. 589–636.

[35] M. Krack and J. Gross. *Harmonic Balance for Nonlinear Vibration Problems*. Springer, 2019. ISBN: 978-3-030-14023-6. DOI: `10.1007/978-3-030-14023-6`.

[36] M. Krack, L. Salles, and F. Thouverez. "Vibration prediction of bladed disks coupled by friction joints". In: *Archives of Computational Methods in Engineering* 24.3 (2017), pp. 589–636.

[37] U. Küttler and W. A. Wall. "Fixed-point fluid–structure interaction solvers with dynamic relaxation". In: *Computational mechanics* 43.1 (2008), pp. 61–72.

[38] C. B. Laney. *Computational gasdynamics*. Cambridge University Press, 1998.

[39] M. Lassalle and C. M. Firrone. "A parametric study of Limit Cycle Oscillation of a bladed disk caused by flutter and friction at the blade root joints". In: *Journal of Fluids and Structures* 76.Supplement C (2018), pp. 349–366. ISSN: 0889-9746. DOI: `10.1016/j.jfluidstructs.2017.10.004`.

[40] S. Leichtfuss et al. "Aeroelastic Investigation of a Transonic Research Compressor". In: *Proceedings of ASME Turbo Expo 2013: Turbine Technical Conference and Exposition*. 55270. 2013, V07BT33A006–. DOI: `10.1115/GT2013-94730`. URL: `http://dx.doi.org/10.1115/GT2013-94730`.

[41] R. A. Leyes and W. A. Fleming. *The history of North American small gas turbine aircraft engines*. AIAA, 1999. ISBN: 1563473321.

[42] F. Lindner et al. "A comparison of various quasi-Newton schemes for partitioned fluid-structure interaction". In: *COUPLED VI: proceedings of the VI International Conference on Computational Methods for Coupled Problems in Science and Engineering*. CIMNE. 2015, pp. 477–488.

[43] C. Martel, R. Corral, and R. Ivaturi. "Flutter Amplitude Saturation by Nonlinear Friction Forces: Reduced Model Verification". In: *Journal of Turbomachinery* 137.4 (2014), p. 041004. DOI: `10.1115/1.4028443`.

[44] C. Martel, R. Corral, and J. M. Llorens. "Stability Increase of Aerodynamically Unstable Rotors Using Intentional Mistuning". In: *Journal of Turbomachinery* 130.1 (2007). DOI: `10.1115/1.2720503`.

[45] N. M. Newmark. "A method of computation for structural dynamics". In: *Journal of the engineering mechanics division* 85.3 (1959), pp. 67–94.

[46] M. Nowinski and J. Panovsky. "Flutter Mechanisms in Low Pressure Turbine Blades". In: *Journal of Engineering for Gas Turbines and Power* 122.1 (1999), pp. 82–88. ISSN: 0742-4795. DOI: `10.1115/1.483179`.

[47] N. Ombret et al. "Investigation of a methodology for describing fan blade flutter limitations induced by non-linear friction at blade roots". In: *COMPDYN Proceedings* 2021-June (2021). URL: `https://www.scopus.com/inward/record.uri?eid=2-s2.0-85120774322&partnerID=40&md5=a0d31dfb8a98ed0e087162b54fa69020`.

[48] S. A. Orszag. "Elimination of aliasing in finite-difference schemes by filtering high-wavenumber components". In: *J. Atmos. Sci.* 28 (1971), p. 1074.

[49] J. Panovsky and R. E. Kielb. "A Design Method to Prevent Low Pressure Turbine Blade Flutter". In: *Journal of Engineering for Gas Turbines and Power* 122.1 (2000), pp. 89–98. DOI: `10.1115/1.483180`.

[50] E. P. Petrov. "A High-Accuracy Model Reduction for Analysis of Nonlinear Vibrations in Structures With Contact Interfaces". In: *Journal of Engineering for Gas Turbines and Power* 133.10 (2010), pp. 102503/1–102503/10.

[51] E. P. Petrov. "Analysis of Flutter-Induced Limit Cycle Oscillations in Gas-Turbine Structures With Friction, Gap, and Other Nonlinear Contact Interfaces". In: *Journal of Turbomachinery* 134.6 (2012), pp. 061018/1–061018/13. DOI: `10.1115/1.4006292`.

[52] E. P. Petrov and D. J. Ewins. "Analytical Formulation of Friction Interface Elements for Analysis of Nonlinear Multi-Harmonic Vibrations of Bladed Disks". In: *Journal of Turbomachinery* 125.2 (2003), pp. 364–371. DOI: `10.1115/1.1539868`.

[53] A. Sayma et al. "Whole-assembly flutter analysis of a low-pressure turbine blade". In: *The Aeronautical Journal* 102.1018 (1998), pp. 459–463.

[54] D. Schluess, C. Frey, and G. Ashcroft. "Consistent Non-reflecting Boundary Conditions For Both Steady And Unsteady Flow Simulations In Turbomachinery Applications". In: *ECCOMAS Congress 2016 VII European Congress on Computational Methods in Applied Sciences and Engineering, Crete Island, Greece*. 2016.

[55] D. Schlüß and C. Frey. "Time Domain Flutter Simulations of a Steam Turbine Stage Using Sptectral 2D Non-Reflecting Boundary Conditions". In: *15th International Symposium on Unsteady Aerodynamics Aeroacoustics and Aeroelasticity Turbomachines*. June 2018.

[56] R. Schnell and D. Nürnberger. "Investigation of the tonal acoustic field of a transonic Fanstage by time-domain CFD-Calculation with Arbitrary Blade Counts". In: *Proceedings of the ASME Turbo Expo 2004*. Vol. 5. GT2004-54216. Vienna, Austria, 2004, pp. 1763–1773. DOI: `10.1115/GT2004-54216`.

[57] M. Schuff and V. A. Chenaux. "Coupled Mode Flutter Analysis of Turbomachinery Blades Using an Adaptation of the p–k Method". In: *Journal of Engineering for Gas Turbines and Power* 143.2 (2021), p. 021017.

[58] R. Seydel. "Practical Bifurcation and Stability Analysis". In: *Interdisciplinary Applied Mathematics*. Vol. 5. Springer New-York, 2010. ISBN: 978-1-4419-1740-9. DOI: `https://doi.org/10.1007/978-1-4419-1740-9`.

[59] A. Sinha and J. H. Griffin. "Friction Damping of Flutter in Gas Turbine Engine Airfoils". In: *AIAA Journal of Aircraft* 20.4 (1983), pp. 372–376.

[60] F. Sotiropoulos and X. Yang. "Immersed boundary methods for simulating fluid–structure interaction". In: *Progress in Aerospace Sciences* 65 (2014), pp. 1–21.

[61] M. Souli, A Ouahsine, and L Lewin. “ALE formulation for fluid–structure interaction problems”. In: *Computer methods in applied mechanics and engineering* 190.5-7 (2000), pp. 659–675.

[62] A. Srinivasan. “Flutter and Resonant Vibration Characteristics of Engine Blades”. In: *Journal of Engineering for Gas Turbines and Power* 119 (Oct. 1997), pp. –.

[63] D. Su, W. Zhang, and Z. Ye. “A reduced order model for uncoupled and coupled cascade flutter analysis”. In: *Journal of Fluids and Structures* 61 (2016), pp. 410–430.

[64] C. M. Tec, J. Gross, and M. Krack. “A massless boundary component mode synthesis method for elastodynamic contact problems”. In: *Computers & Structures* 260 (2022), p. 106698.

[65] C. Voigt, C. Frey, and H.-P. Kersken. “Development of a Generic Surface Mapping Algorithm for Fluid-Structure-Interaction Simulations in Turbomachinery”. In: *V European Conference on Computational Fluid Dynamics ECCOMAS CFD 2010*. Ed. by J. C. F. Pereira, A. Sequeira, and J. M. C. Pereira. June 2010. URL: `http://elib.dlr.de/64893/`.

[66] J. J. Waite and R. E. Kielb. “Physical Understanding and Sensitivities of Low Pressure Turbine Flutter”. In: *Journal of Engineering for Gas Turbines and Power* 137.1 (Aug. 2014), pp. 012502–012502. ISSN: 0742-4795. DOI: `10.1115/1.4028207`. URL: `http://dx.doi.org/10.1115/1.4028207`.

[67] S. T. Wei and C. Pierre. “Localization Phenomena in Mistuned Assemblies with Cyclic Symmetry. Part I: Free Vibrations”. In: *Journal of Vibration, Acoustics, Stress, and Reliability in Design* 110.4 (1988), pp. 429–438. DOI: `10.1115/1.3269547`.

[68] S. T. Wei and C. Pierre. “Localization Phenomena in Mistuned Assemblies with Cyclic Symmetry. Part II: Forced Vibrations”. In: *Journal of Vibration, Acoustics, Stress, and Reliability in Design* 110.4 (1988), pp. 439–449. DOI: `10.1115/1.3269548`.

[69] D. C. Wilcox. “Reassessment of the Scale-Determining Equation for Advanced Turbulence Models”. In: *AIAA J.* 26.11 (1988), pp. 1299–1310.

[70] L. Woiwode, A. F. Vakakis, and M. Krack. “Analysis of the non-periodic oscillations of a self-excited friction-damped system with closely spaced modes”. In: *Nonlinear Dynamics* 106.3 (2021), pp. 1659–1673.

[71] X. Wu et al. *Analysis of low-pressure turbine flutter for different shroud interfaces*. Proceedings of the ASME Turbo Expo, May 14-17, Montreal, Canada. 2007.

[72] A. H. van Zuijlen. “Fluid-structure interaction simulations: efficient higher order time integration of partitioned systems”. PhD thesis. TU Delft, Nov. 22, 2006. ISBN: 90-8559-254-2. URL: `http://resolver.tudelft.nl/uuid:fd466357-7890-45bd-b199-3df64df2e6d7`.